

**EXPLORING CHEMICAL REACTION COMPLEXITY:
APPLICATION TO HYDROGEN COMBUSTION**

A Dissertation

presented to

the Faculty of the Graduate School

at the University of Missouri-Columbia

In Partial Fulfillment

of the Requirements for the Degree

Doctor of Philosophy in Chemistry

by

HOMAYOON RAFATIJO

Dissertation Supervisor: Prof. Donald L. Thompson

JULY 2017

© Copyright by Homayoon Rafatijo 2017

All Rights Reserved

The undersigned, appointed by the dean of the Graduate School, have examined the dissertation entitled

EXPLORING CHEMICAL REACTION COMPLEXITY:

APPLICATION TO HYDROGEN COMBUSTION

presented by Homayoon Rafatijo,

a candidate for the degree of doctor of philosophy in chemistry, and hereby certify that, in their opinion, it is worthy of acceptance.

Professor Donald L. Thompson

Professor Thomas D. Sewell

Professor Paul F. Miceli

Professor Giovanni Vignale

Professor Mark W. Lee Jr.

In loving memory of my brother, Hooman...

ACKNOWLEDGMENTS

*“They have drawn so many a bow of reproach upon me,
That I have conquered the matter by the beloved’s eyebrow”*

Hafez

I would like to humbly and sincerely thank Professor Donald. L. Thompson for his expert supervision and kindness throughout this difficult project. I would also like to express my gratitude to Professors Sewell, Miceli, Vignale, and Lee for all advice and many incisive comments. I should thank Professor Malaek, my role model, who taught me the scientific ethics and etiquette. I am also very grateful of my undergraduate adviser Professor Parsafar who extended my view of theoretical physical chemistry.

Finally, and most importantly, I would like to thank my wife, Tahereh, for her moral support, patience and encouragement. Her understanding and tolerance of my abnormal office hours is a testament in itself of her love and devotion. I thank my parents, Fereydoon and Mahnaz, for their insistence on continuing my academic journey. I would like to thank my godparents, Behrouz and Mona, for embracing me as their son. I want to acknowledge my true friend, Mirjavad Miremarati, for all his brotherhood long distance supports throughout these years.

This work was supported by the U. S. Army Research Laboratory and the U. S. Army Research Office under grant number W911NF-14-1-0359.

TABLE OF CONTENTS

| | |
|--|-----|
| ACKNOWLEDGMENTS | ii |
| LIST OF ILLUSTRATIONS | vi |
| LIST OF TABLES | xiv |
| ABSTRACT | xv |
| CHAPTERS | |
| 1. INTRODUCTION..... | 1 |
| 1.1 DESCRIPTION OF THE PROBLEM | 1 |
| 1.2 MECHANISM REDUCTION | 3 |
| 1.3 CHARACTERIZATION OF THE TOPOLOGIES OF THE POTENTIAL ENERGY SURFACES | 9 |
| 1.4 MOLECULAR DYNAMICS SIMULATIONS..... | 10 |
| 1.5 OVERVIEW OF HYDROGEN COMBUSTION MECHANISMS | 13 |
| 1.6 ReaxFF REACTIVE FORCE FIELD | 19 |
| 1.7 GOALS OF THIS STUDY | 21 |
| 2. EARLY CHEMISTRY OF HYDROGEN COMBUSTION | 23 |
| 2.1 REAXFF VALIDATION FOR INTERACTION ENERGIES AND EQUATIONS OF STATE..... | 25 |
| 2.2 COMPUTATIONAL METHODS | 32 |
| 2.2.1 SIMULATION DETAILS | 32 |

| | |
|---|-----|
| 2.2.2 REACTION IDENTIFICATION ALGORITHM..... | 36 |
| 2.3 INITIAL REACTIONS..... | 38 |
| 2.4 EFFECTS OF DENSITY | 45 |
| 2.4.1 COLLISION FREQUENCY..... | 47 |
| 3. POTENTIAL ENERGY PROFILE AND ENERGY REQUIREMENT | 60 |
| 3.1 COMPUTATIONAL METHODS | 60 |
| 3.1.1 NUDGED ELASTIC BAND METHOD | 60 |
| 3.1.2 ELECTRONIC STRUCTURE CALCULATIONS | 62 |
| 3.2 OXYGEN DIMER | 63 |
| 3.3 RESULTS AND DISCUSSION | 66 |
| 3.3.1 NEB RESULTS FOR ReaxFF FORCE FIELD | 66 |
| 3.3.2 AB INITIO RESULTS..... | 68 |
| 3.4 EFFECTS OF TEMPRATURE ON THE EARLY CHEMISTRY OF HYDROGEN COMBUSTION..... | 83 |
| 3.5 STERIC EFFECTS | 87 |
| 4. GENERAL APPLICATION OF TOLMAN’S CONCEPT OF ACTIVATION ENERGY | 90 |
| 4.1 GENERALIZED TOLMAN ACTIVATION ENERGY | 95 |
| 4.2 CANONICAL ENSEMBLE | 98 |
| 4.2.1 COMPUTATIONAL METHODS | 98 |
| 4.2.2 RESULTS AND DISCUSSION | 102 |
| 4.3 MICROCANONICAL ENSEMBLE | 111 |

| | |
|--|-----|
| 4.3.1 COMPUTATIONAL METHODS | 111 |
| 4.3.2 ATOMIC REACTION SEQUENCE AND REACTION STREAM | 112 |
| 4.3.3 NEB CALCULATIONS | 118 |
| 4.3.4 APPLICATION OF GENERALIZED TOLMAN ACTIVATION ENERGY TO NON-THERMAL REACTIONS..... | 121 |
| 4.3.5 THEORETICAL METHODS AND RESULTS | 124 |
| 5. CONCLUSION | 130 |
| 6. APPENDIX I..... | 132 |
| BIBLIOGRAPHY | 134 |
| VITA | 153 |

LIST OF ILLUSTRATIONS

- Figure 1.1:** A schematic illustration of P - T diagram of explosion limits for $H_2:O_2$ mixtures..... **19**
- Figure 2.1:** Top frame: Comparison of the intermolecular (dimer) potential energy for the linear configuration of two ground state oxygen molecules, that is, $O_2(^3\Sigma_g^-)-O_2(^3\Sigma_g^-)$ dimer predicted by ReaxFF (black curve) and the three lowest multiplet spin states for the $O_2(^3\Sigma_g^-)-O_2(^3\Sigma_g^-)$ dimer calculated using MRCI with SPACE-1 and B1 basis set reported by Bartolomei *et al.* Bottom frame: Comparison of $H_2\cdots H_2$ interaction energy predicted by ReaxFF (solid curves) and the results of CCSD(T)/cc-pVTZ (dashed curves) for linear (blue) and perpendicular (red) configurations. **26**
- Figure 2.2:** Top frame: Comparison of the results for the EOS of H_2 predicted by ReaxFF (solid curves) and the empirical equation reported by Lemmon *et al.* (dashed curves) at different temperatures: 300 K (red), 500 K (green) and 1,000 K (blue). Bottom frame: relative error in ReaxFF prediction of pressure for H_2 at different temperatures of the top frame. **29**
- Figure 2.3:** Top frame: Comparison of the results for the EOS of O_2 predicted by ReaxFF (solid curves) and the empirical equation reported by Kuznetsov *et al.* (dashed curves) at different temperatures. Light blue: 300 K, violet: 500 K, pink: 1,000 K, dark blue: 2,000 K, green: 3,000 K and red: 4,000 K. Bottom frame: Relative error in ReaxFF prediction of pressure for O_2 at different temperatures of previous frame. **31**
- Figure 2.4:** The average translational (top frame), rotational (middle frames), and vibrational (bottom frames) kinetic temperatures of hydrogen molecules during the first

100 ps of a typical simulation at thermodynamic temperature of 3,000 K, 276.3 kg·m⁻³, and composition ratio of [H₂]/[O₂] = 1. For the rotational and vibrational parts, kinetic temperature was also plotted during the first 10 ps to show the completion of the equilibration (right frames). The target thermodynamic temperature is shown by a horizontal black line.....**34**

Figure 2.5: The average translational (top frame), rotational (middle frames), and vibrational (bottom frames) kinetic temperatures of oxygen molecules during the first 100 ps of a typical simulation at thermodynamic temperature of 3,000 K, 276.3 kg·m⁻³, and composition ratio of [H₂]/[O₂] = 1. For the rotational and vibrational parts, kinetic temperature was also plotted during the first 15 and 20 ps, respectively, to show the completion of the equilibration (right frames). The target thermodynamic temperature is shown by a horizontal black line.**35**

Figure 2.6: The reaction identification algorithm flowchart.....**38**

Figure 2.7: The evolution of interatomic distances for a typical trajectory of the bimolecular reaction $O_2 + H_2 \rightarrow H + HO_2$**39**

Figure 2.8: Top frame: The evolution of interatomic distances for a typical trajectory of the synchronous termolecular reaction $2O_2 + H_2 \rightarrow 2HO_2$. Bottom frame: The evolution of interatomic distances for a typical trajectory of the asynchronous termolecular reaction $2O_2 + H_2 \rightarrow 2HO_2$**40**

Figure 2.9: Top frame: The evolution of interatomic distances for a typical trajectory of indirect termolecular reaction $2O_2 + H_2 \rightarrow HO_2 \cdots HO_2 \rightarrow H_2O_2 + O_2$. Bottom frame: The evolution of interatomic distances for a typical trajectory of indirect termolecular reaction $2O_2 + H_2 \rightarrow HO_2 \cdots HO_2 \rightarrow 2H_2O$**41**

Figure 2.10: The evolution of interatomic distances for a typical trajectory of the termolecular reaction $2\text{O}_2 + \text{H}_2 \rightarrow \text{H} + \text{HO}_2 + \text{O}_2$ in which one O_2 molecule acts as a third body..... **42**

Figure 2.11: Probabilities of the $\text{O}_2 + \text{H}_2 + (\text{M}) \rightarrow \text{H} + \text{HO}_2 + (\text{M})$ (dashed trend-lines) and $2\text{O}_2 + \text{H}_2 \rightarrow 2\text{HO}_2$ (dotted trend-lines) reactions occurring as initial reactions as functions of density for composition ratios (top frame) $[\text{H}_2]/[\text{O}_2] = 0.25$, (middle frame) $[\text{H}_2]/[\text{O}_2] = 0.5$, (bottom left) $[\text{H}_2]/[\text{O}_2] = 1$ and (bottom right) $[\text{H}_2]/[\text{O}_2] = 2$ at 3,000 K (blue), 4,000 K (green), and 5,000 K (red). The density changes were effected by varying the volume of the simulation box. The margins of error were calculated using $\text{error} = Z\sqrt{([P(1 - P)]/N)}$, where Z is 1.645 to give 90% level of confidence, P is the reaction probability, and N is the number of trajectories run for a given set of initial conditions. In most cases ensembles of 50 trajectories were run, but in some cases an additional 20 trajectories were run to lower the margin of error. The average of the error over all data points is ± 0.09 **46**

Figure 2.12: Average collision frequencies of the bimolecular $\text{O}_2 \cdots \text{H}_2$ (yellow curves and circle points, left y-axis) and termolecular $\text{O}_2 \cdots \text{H}_2 \cdots \text{O}_2$ (purple curves and square points, right y-axis) collisions as functions of density at 3,000 K (dashed curves and blue points) and 4,000 K (solid curves and green points). The density was varied by varying the volume of the simulation box for the composition ratio $[\text{H}_2]/[\text{O}_2] = 0.25$ **48**

Figure 2.13: A schematic illustration of effective pair potential. Pairs with $E < 0$ form permanently bound molecules. Pairs with $0 < E < E^*$ and $r < r^*$ are referred to as metastably bound molecules trapped inside the centrifugal barrier. Pairs with $E \simeq E^*$ and $r \simeq r^*$ can dance around each other for a long time since the attractive part of the

potential and the centrifugal repulsion part are balanced. These pairs are called transient pairs and are very effective in producing termolecular collisions.53

Figure 2.14: Average durations of the $O_2 \cdots O_2$ (yellow curves and circle points, left y-axis) and $O_2 \cdots H_2$ (purple curves and square points, right y-axis) collisions as functions of density at 3,000 K (dashed curves and blue points) and 4,000 K (solid curves and green points). The density was varied by varying the volume of the simulation box with $[H_2]/[O_2] = 0.25$57

Figure 2.15: The ratios of the termolecular collision frequency to the bimolecular collision frequency computed using Eq. (16) at 3,000 K (blue) and 4,000 K (green). 57

Figure 2.16: The characteristic ratio of the termolecular collision frequency to the bimolecular collision frequency computed using Eq. (17) at 3,000 K (blue) and 4,000 K (green). The characteristic ratio is independent of temperature.59

Figure 3.1: Schematic representations of the molecular orbitals for the O_2 - O_2 dimer according to CCSD(T) calculations performed by Gadzhiev *et al.*: (a) quintet state; (b) triplet state; (c) singlet state. They postulated that for exploring the triplet and singlet PESs raised from two ground-state oxygen molecules, $2O_2(^3\Sigma_g^-)$, CCSD(T) methods may not be useful.65

Figure 3.2: ReaxFF potential energy profile obtained *via* NEB method with the energy (kcal/mol), with respect to the reactants of the termolecular $2O_2 + H_2 \rightarrow 2HO_2$ (green lines) and bimolecular $H_2 + O_2 \rightarrow H + HO_2$ (blue lines) reactions. Optimized geometry of the stationary points including the reactant complexes (RC) and the saddle points (SP) predicted by ReaxFF are included, as well. (Distances in angstroms)67

Figure 3.3: Optimized geometries (distances in angstroms) at the CCSD=FC/cc-pVTZ *ab initio* level of the saddle points and intermediate complexes on the triplet PES of the (a) termolecular and (b) bimolecular reactions, $2\text{O}_2 + \text{H}_2 \rightarrow 2\text{HO}_2$, $2\text{O}_2 + \text{H}_2 \rightarrow \text{H} + \text{HO}_2 + \text{O}_2$ and $\text{H}_2 + \text{O}_2 \rightarrow \text{H} + \text{HO}_2$ (SP2 and SP3 at the MP2/6-31G level). The eigenvectors associated to the imaginary frequencies of the saddle points of the termolecular reactions are also given. **69**

Figure 3.4: Molecular orbitals at SP1, the symmetric saddle point on the $2\text{O}_2 + \text{H}_2 \rightarrow 2\text{HO}_2$ triplet PES, formed by the (a) Π_x and (b) Π_x^* orbitals of the $\text{O}_2(^3\Sigma_g^-)$ molecules. The Π_x and Π_x^* orbitals are orthogonal to the double bond. **77**

Figure 3.5: Molecular orbitals at SP2, the asymmetric saddle point on the $2\text{O}_2 + \text{H}_2 \rightarrow 2\text{HO}_2$ triplet PES, formed by the Π_x , (a) and (b), and Π_x^* , (c) and (d), orbitals of the $\text{O}_2(^3\Sigma_g^-)$ molecules. The Π_x and Π_x^* orbitals are orthogonal to the double bond. **77**

Figure 3.6: Classical potential energy profile with the energy (kcal/mol), with respect to the reactants, and optimized geometry, of the stationary points found on the triplet potential energy surfaces of the termolecular $2\text{O}_2 + \text{H}_2 \rightarrow 2\text{HO}_2$ (the top panel) and bimolecular $\text{H}_2 + \text{O}_2 \rightarrow \text{H} + \text{HO}_2$ (the bottom panel) reactions at the CCSD(T)=FULL/aug-cc-pVTZ//CCSD=FC/cc-pVTZ *ab initio* level. **82**

Figure 3.7: The probability distribution of the bond angle(s) α O–O–H for the bimolecular (green) and termolecular (red and blue) reaction clusters. The probability distributions are fitted to the beta distribution function and were obtained for the bond angles of 50 individual reaction clusters calculated during the interval between formation of each reaction cluster and rupturing of the H-H bond. **87**

Figure 4.1: Average relative translational energy for all $\text{H}_2 + 2\text{O}_2$ groups as a function of time for a typical simulation. The time average of the quantity is 17.92 kcal/mol that is about $3RT$ **103**

Figure 4.2: The local energy (LE) of the reactants (dashed blue curves) and products (dashed red curves), both calculated using Eq. (22) for (a) a typical $\text{H}_2 + \text{O}_2 \rightarrow \text{H} + \text{HO}_2$ reaction and (c) a typical $\text{H}_2 + 2\text{O}_2 \rightarrow 2\text{HO}_2$ reaction. The LE is the minimum of these local energy curves and plotted in green for (b) the bimolecular reaction and (d) the termolecular reaction. The transition configuration for each reaction is shown by an arrow. For each individual reaction, the thermal energy curves are shown by blue and red dotted curves for the reactant and product arrangement of the reaction cluster, respectively. The thermal energy (TE) curves are shown in purple. The Tolman activation energy for these individual reactions is 39.8 kcal/mol and 26.3 kcal/mol for the bi- and ter-molecular reaction, respectively. **106**

Figure 4.3: The local energy curves for the reactant arrangement of two typical bimolecular reaction cluster $\text{H}_2 + \text{O}_2 \rightarrow \text{H} + \text{HO}_2$. The time origin sets at 215 fs prior to detection of the reaction that is rupturing of the H_2 molecule. For the reaction cluster shown in red, the local energy is constant in the interval prior to the time at which reaction was detected. However, the local energy shown by the blue curve abruptly increases about 75 fs prior to breaking of the H-H bond. This abrupt change is due to a H_2 molecule colliding with a collision complex previously formed by a H_2 and an O_2 molecule. This collision occurs about 55 fs before the formation of the reaction cluster. **107**

Figure 4.4: The local energy (LE) path (green curves) and the thermal energy (TE) path (purple curves) were obtained by averaging over 30 individual reaction LEs and TEs, respectively, and shown for the bimolecular (top panel) and termolecular (bottom panel) reactions. The average local energy curves are plotted for reactants (blue) and products (red). While near the time of the reaction, the average RCLE is conserved, the bimolecular and termolecular reaction clusters lose 42.1 kcal/mol and 4.0 kcal/mol thermal energy on average, respectively. The Tolman activation energy was computed as the average of 30 individual activation energies..... **108**

Figure 4.5: The reaction identification algorithm monitors the evolution of internuclear distances within the reaction cluster; the dashed green curve shows the local energy (LE) which maximum is associated to the energy of the presumptive TC. (a) A typical bimolecular reaction with the transition configuration (TC) geometry of $r_{\text{H-H}} = 1.22 \text{ \AA}$, $r_{\text{O-H}} = 1.26 \text{ \AA}$ and $r_{\text{O-O}} = 1.26 \text{ \AA}$, and (b) a typical termolecular reaction with the TC geometry of $r_{\text{H-H}} = 1.15 \text{ \AA}$, $r_{\text{O-H}} = 1.34 \text{ \AA}$, $r_{\text{O-H}} = 1.34 \text{ \AA}$, $r_{\text{O-O}} = 1.29 \text{ \AA}$ and $r_{\text{O-O}} = 1.23 \text{ \AA}$ **110**

Figure 4.6: (a) All atomic species sequences (ASSs) found for (a) H atoms and (b) O atoms from analysis of 50 NVE simulations of 10 H_2O_2 molecules equilibrated at 2,100 K and $275.6 \text{ kg}\cdot\text{m}^{-3}$ **114**

Figure 4.7: The dominant atomic species sequences (ASSs) obtained by removing less frequent ASSs with occurrence probability $< 1\%$ from Figure 4.6 for (a) H atoms and (b) O atoms. **115**

Figure 4.8: The dominant subset of atomic reaction stream (ARS) for H atoms obtained from analysis of 50 NVE simulations of 10 H_2O_2 molecules equilibrated at 2,100 K and

275.6 kg·m⁻³. Dominant reaction sequences which connect (a) a H₂O₂ molecule to a H₂O molecule, (b) a H₂O molecule to a H₂O₂ molecule, (c) a H₂O₂ molecule to a H₂O₂ molecule, and (d) a H₂O molecule to a H₂O molecule. **116**

Figure 4.9: ReaxFF prediction for the potential energy profile of the dominant reactions in atomic reaction stream (ARS) of thermal dissociation of H₂O₂. Reactant complex (RC), saddle point (SP), and product complex (PC) are energetically characterized for each reaction. Attempts to characterize the potential energy profile for reactions (R4) and (R7) failed **120**

Figure 4.10: The Tolman activation energy for 40 individual secondary reactions of H₂O₂ + OH → HO₂ + H₂O in the simulation of the thermal dissociation of H₂O₂. **129**

LIST OF TABLES

| | |
|---|------------|
| Table 3.1: The ReaxFF predictions for the geometrical parameters of the stationary points of the potential energy surface for the ter- and bi-molecular reactions obtained by the NEB method..... | 68 |
| Table 3.2: <i>Ab initio</i> calculated geometries, vibrational frequencies, saddle point and complex energies relative to reactants, ΔV , enthalpy changes, ΔH (0 K), and absolute energies. | 71 |
| Table 3.3: The probabilities of fulfillment of energy requirement of Eq. (4) for the ter- and bi-molecular reactions, respectively, at 3,000 K, 4,000 K, and 5,000 K. | 86 |
| Table 4.1: Predicted transition configuration (TC) geometries determined by using Tolman's approach and saddle point (SP) structures obtained using NEB method for bi- and ter-molecular reactions. The reported values are the average over an ensemble of 30 individual TC. | 109 |
| Table 4.2: The dominant subset of atomic reaction stream (ARS) for H atoms..... | 117 |

ABSTRACT

The aim of this research is to gain insight into hydrogen combustion as a prototype of complex chemistry *via* classical molecular dynamics (CMD) simulations given the presently available reactive force field, ReaxFF. We focus on developing computational and theoretical methods to analyze CMD simulations of hydrogen combustion and glean the details of chemistry to identify major sequential elementary reactions connecting reactants to products.

In Chapter 1 we explain the problem exists in understanding complex chemistry followed by a brief overview of currently popular methods used to study complex chemical processes with an emphasis on hydrogen combustion. Then, we propose our approach that is based on CMD simulations to tackle the problem and elaborate on the goals of the study.

In Chapter 2 we introduce an algorithm that identifies every elementary molecular event such as reactions and formation/dissociation of hydrogen-bond complexes in CMD simulations of hydrogen combustion. After validating the ReaxFF force field for the equation of state and interaction energy, we then present ReaxFF-based results of CMD simulations for the early chemistry of hydrogen combustion. The CMD simulations predict two major pathways for production of initial radicals; a termolecular elementary reaction $2\text{O}_2 + \text{H}_2 \rightarrow 2\text{HO}_2$ and the widely-accepted bimolecular reaction $\text{O}_2 + \text{H}_2 \rightarrow \text{H} + \text{HO}_2$. Later in Chapter 2, we present and discuss the effects of density on the early chemistry of hydrogen combustion; which show that at elevated density and low temperature the termolecular reaction dominates the chemistry. We describe a method

based on collision gas theory that can be used with CMD simulations to explain the observed trends.

In Chapter 3, we provide results for Nudged Elastic Band method (NEB) to characterize potential energy profiles for the bi- and ter-molecular reactions predicted by ReaxFF. Then, we use state-of-the-art electronic structure calculations to examine accuracy of the ReaxFF predictions for the energies and stationary points of the reactions. Later in Chapter 3 we discuss the effect of temperature on the occurrence probability of the ter- and bi-molecular reactions based on the electronic structure predictions of the energy barriers. Lastly, we identify the steric requirements predicted by ReaxFF for each reaction based on the CMD simulations.

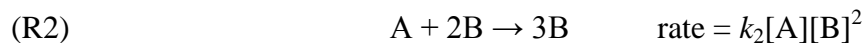
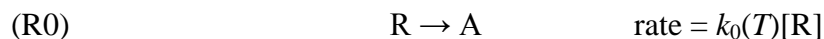
In Chapter 4, we present a method based on Tolman's interpretation of activation energy that can be applied to thermal and non-thermal chemical reactions in molecular dynamics simulations of bulk gases. We use Boyd's assumption of local equilibrium thermodynamics to generalize Tolman's concept for application to individual reaction clusters, which include all chemical species that participate in an isolated reaction, for which we define the reaction cluster local energy (RCLE). The RLCE is shown to be conserved during the course of a reaction. We identify the transition configuration (TC), which is the point where the local energy of the reactants crosses that of the products. The TC is a unique point that separates reactants and products and can be used as an estimation of the transition state in accordance with Marcus theory for proton transfer reactions. We demonstrate application of the method by computing activation energies of the several reactions in molecular dynamics simulations.

1. INTRODUCTION

1.1 DESCRIPTION OF THE PROBLEM

Accurately characterizing the complexity of combustion chemistry is a challenging problem. The chemical complexity mainly originates from the fundamental nature of the electronic structure that results in an enormous number of elementary molecular reactions involving many transient intermediates, many with very short lifetimes. The chemistry usually evolves through a set of branching sequential reactions. The reactions are modeled *via* a set of coupled nonlinear differential equations whose solutions (obtained by using numerical integration techniques) may not be true to the real chemistry. These equations include temperature- and pressure-dependent parameters that are not always determinable over the thermodynamic conditions of the real chemistry. The variation of these temperature- and pressure-dependent parameters with thermodynamic conditions amplifies the complexity.

To illustrate complexity of these mathematical models, we employ the non-isothermal cubic autocatalator chemical scheme introduced by Scott and co-workers¹⁻³ as an example. The model can describe oscillatory behavior of chemically isolated systems. In this scheme, a reactant species R is converted to a product P through a set of irreversible elementary reactions involving intermediate species of A and B; that is,



In this chemical scheme, it is assumed that only the termination step (R3) involves heat change, and it is exothermic. Usually the rate determining reaction is the most temperature-sensitive process. In the non-isothermal cubic autocatalator model the initiation reaction (R0) is rate determining, has an Arrhenius temperature dependence; that is,

$$k_0 = A \exp\left(\frac{-E_a}{RT}\right). \quad (1)$$

We may now construct a set of coupled nonlinear ordinary differential equations that can describe the behavior of this chemical scheme. This set may consist of rate equations for the species of our choice or/and balance equations for thermodynamic variables. For simplicity, let us consider the case where reactant concentration [R] remains unchanged—referred to as the “pool chemical approximation”.³ Thus, the governing differential equations are the reaction rate equations for intermediates A and B,

$$\frac{d[A]}{dt} = A \exp\left(\frac{-E_a}{RT}\right)[R] - k_1[A] - k_2[B]^2[A], \quad (2)$$

$$\frac{d[B]}{dt} = k_1[A] + k_2[B]^2[A] - k_3[B], \quad (3)$$

and the heat-balance equation is

$$\frac{dT}{dt} = \chi k_3 [\text{B}], \quad (4)$$

where χ is the exothermicity of reaction (R3) at constant volume.

Therefore, even a simple chemical model as the one introduced here can mathematically be very complex to describe. This complexity would significantly increase if we were to consider rate equation for the reactant species R, the temperature- and pressure-dependences for all rate coefficients, or rate equations for the reversible processes. Thus, even for relatively simple processes like combustion of hydrogen with many chemical species and reactions involved, one should mathematically deal with a huge number of coupled differential equations that is far from simple to handle even numerically.

There are several approaches to simplify the problem all of which lead to insufficiently accurate models. Mechanism reduction, characterization of the topologies of the potential energy surfaces, and molecular dynamics (MD) simulations methods are among the most studied approaches.

1.2 MECHANISM REDUCTION

The earliest systematic approach to describe chemical reaction complexity was to identify a set of elementary reactions, commonly referred to as overall reaction mechanism, responsible for transformation of reactants into products. These elementary reactions were mostly, but not exclusively, bimolecular. The foundations of this approach were constructed in late 18th and early 19th centuries by pioneers like Lavoisier, Wenzel, Berthollet, and Faraday.

Among the common practical approaches to simplify the complexity of chemical mechanisms were quasi-steady-state assumption (QSSA) and partial equilibrium (PE) method. In the QSSA that was formally proposed in 1913 by Bodenstein,⁴ it is assumed that intermediate species react in a relatively short time scale and consumed immediately after they are formed. The QSSA yields to set rate equations of the intermediate species equal to zero, so that their equilibrium concentrations can be expressed in terms of concentrations of reactants and products. In the PE method, a mechanism is divided into fast and slow reactions, and it is assumed that fast reactions are always at equilibrium and slow reactions govern the rate. In particular, if a fast reaction is followed by a slow reaction, concentrations of the fast reaction products are not required to determine the overall rate.

The QSSA and PE methods are useful tools for mathematical simplifications of smaller chemical models and have been widely used. However, for a complex process such as combustion where we must deal with many parameters, identifying QSSA species and PE reactions are not straightforward especially because the thermodynamic conditions in combustion constantly changes. Therefore, a sophisticated mathematical method to identify important elementary reactions to be included in an overall mechanism seems vital.

In 1985 Vajda *et al.*⁵ presented a method to set up a basis for reduction of a detailed kinetic model including all potential elementary reactions that could occur in a system. The idea is to convert the correlated variables, such as species concentrations, into a set of linearly uncorrelated variables (the principal components), and elementary reactions with no significant contribution to the evolution of the principal components are

disregarded. This approach has been widely used for mechanism reduction of combustion processes.⁶⁻⁸

The procedure involves a set of variables $\mathbf{C} = \{C_1, C_2, C_3, \dots, C_n\}$ representing temperature and species concentrations. Since it is impossible to follow the values of set \mathbf{C} as continuous functions of time, let us assume set \mathbf{C} is determined *via* independent measurements at a series of times $t = t_1, t_2, t_3, \dots, t_q$. Also, let p denote the total number of elementary reactions in a mechanism that governs evolution of the set \mathbf{C} . The rate of each elementary reaction is described by an Arrhenius expression. Thus, the vector \mathbf{k} is the rate expression for the overall mechanism; that is,

$$\mathbf{k} = \mathbf{A}T^{\boldsymbol{\beta}} \exp\left(\frac{-\mathbf{E}_a}{RT}\right), \quad (5)$$

where \mathbf{A} , $\boldsymbol{\beta}$, and \mathbf{E}_a are vectors of pre-exponential constants, temperature exponents, and activation energies for the p reactions. Let \mathbf{k}^0 be the unperturbed vector of rate expressions calculated for arbitrary thermodynamic conditions. Therefore, $C_{i,j}(\mathbf{k})$ stands for concentration of the i^{th} species at time t_j when the overall rate expression for the overall mechanism is \mathbf{k} . According to Lutz *et al.*⁹ a set of differential equations that describes the evolution of this system has the general form

$$\frac{d\mathbf{C}}{dt} = \mathbf{F}(\mathbf{C}, t; \mathbf{k}). \quad (6)$$

Differentiating Eq. (6) with respect to rate constant of the l^{th} reaction k_l gives

$$\frac{dw_{i,l}}{dt} = \frac{\partial F}{\partial C} \times w_{i,l} + \frac{\partial F_i}{\partial k_l} \quad \text{for } i = 1, 2, 3, \dots, n; \quad (7)$$

where $w_{i,l}$ are elements of the first-order sensitivity coefficient matrix, defined as

$$w_{i,l} = \frac{\partial C_i}{\partial k_l}. \quad (8)$$

In principal component analysis, we seek to quantify the variation of concentrations (in general, dependent variables) result from the variation (perturbation) of \mathbf{k} from its unperturbed nominal value \mathbf{k}^0 by defining a response function as

$$Q(\mathbf{k}) = \sum_{j=1}^q \sum_{i=1}^n \left[\frac{C_{i,j}(\mathbf{k}) - C_{i,j}(\mathbf{k}^0)}{C_{i,j}(\mathbf{k}^0)} \right]^2. \quad (9)$$

With $\boldsymbol{\alpha} = \ln(\mathbf{k})$ the classical Gauss approximation for the Taylor's expansion of $Q(\mathbf{k})$ about \mathbf{k}^0 gives

$$Q(\mathbf{k}) = \Delta \boldsymbol{\alpha}^T \mathbf{S}^T \mathbf{S} \Delta \boldsymbol{\alpha}, \quad (10)$$

where \mathbf{S} is the matrix of sensitivity coefficients with $n \times q$ rows and p columns in form of

$$\mathbf{S} = [\mathbf{S}_1 \quad \mathbf{S}_2 \quad \dots \quad \mathbf{S}_q]^T, \quad (11)$$

where \mathbf{S}_j is an array of normalized sensitivities at time t_j ; that is,

$$\mathbf{S}_j = \begin{bmatrix} \hat{W}_{1,1,j} & \hat{W}_{1,2,j} & \cdots & \hat{W}_{1,p,j} \\ \hat{W}_{2,1,j} & \hat{W}_{i,l,j} & \cdots & \hat{W}_{2,p,j} \\ \cdot & \cdot & \cdot & \cdot \\ \hat{W}_{n,1,j} & \hat{W}_{n,2,j} & \cdots & \hat{W}_{n,p,j} \end{bmatrix}. \quad (12)$$

In Eq. (12) $\hat{W}_{i,l,j}$ is the normalized first-order sensitivity coefficient matrix elements at time t_j ; that is, according to Eq. (8)

$$\hat{W}_{i,l,j} = \frac{k_{l,j}}{C_{i,j}} \frac{\partial C_{i,j}}{\partial k_{l,j}} = \frac{\partial \ln C_{i,j}}{\partial \ln k_{l,j}}. \quad (13)$$

Eigenvalue-eigenvector decomposition of the matrix $\mathbf{S}^T \mathbf{S}$ yields

$$\mathbf{S}^T \mathbf{S} = \mathbf{U} \boldsymbol{\lambda} \mathbf{U}^T, \quad (14)$$

where \mathbf{U} is an orthogonal set of p eigenvectors associated with p reactions which represent the directions of principal variables, and $\boldsymbol{\lambda}$ is diagonal matrix of eigenvalues.

Principal components are defined as

$$\boldsymbol{\Psi} = \mathbf{U}^T \mathbf{k}, \quad (15)$$

which leads to the canonical form of the response function as

$$Q(\mathbf{k}) = \sum_{l=1}^p \lambda_l \boldsymbol{\psi}_l^T \boldsymbol{\psi}_l . \quad (16)$$

Equation (16) shows that the effect on the response function by a change of one unit of a principal component $\boldsymbol{\psi}_l$ is equal to the corresponding eigenvalue λ_l . Vajda *et al.*⁵ showed that elimination of components (reactions) with magnitudes less than 0.2 from the eigenvector of the largest eigenvalue results in no more than a 4% error. After elimination of reactions specified above, species which were not involved in any of the remaining reactions could be disregarded. It should be noted that exclusion of an elementary reaction from a mechanism does not imply that the reaction does not occur, but merely indicates that the reaction is not significant or likely over the thermodynamic conditions studied.

One of the disadvantages of principal component analysis is its sensitivity to parameters of kinetic models, activation energies and rate coefficients of elementary reactions. Different calculation/measurement methods lead to different magnitudes for the parameters. Another disadvantage of principal component analysis, and in general, any reduction techniques, is that they usually fail when applied to systems with a large number of degrees of freedom. Fast transient dynamics of the chemical species, the main characteristic of combustion, adds to the inaccuracies of these methods. Finally, as the principal component method mathematically represents a basic linearization procedure, some vital chemical information to describe the chemical complexity may be lost. This is mainly due to the fact that chemistry, in essence, evolves nonlinearly.

1.3 CHARACTERIZATION OF THE TOPOLOGIES OF THE POTENTIAL ENERGY SURFACES

Characterization of the critical points on the potential energy surfaces (PESs) of reactions is fundamental to describing chemistry. *Ab initio* electronic structure theory can be used to accurately identify critical points and energy requirements for reactions with few degrees of freedom. However, for processes with a large number of degrees of freedom like combustion, employing *ab initio* electronic structure theory is very expensive in cpu time and thus is not practical. Therefore, for such complex systems it is not of interest (and even feasible) to characterize every critical point of the entire topology of the PESs. Instead, we are primarily interested in characterizing the critical points for the regions of the topology that are critically important from the point of view of dynamics and kinetics. Then one could use topological reconstruction techniques^{10,11} to map out those regions to accurately describe the complexity of combustion. This is essentially an interpolation problem in which the goal is to find a function $V(\mathbf{x})$ that smoothly connects a discrete set of *ab initio* energy values V_i calculated for a set of geometries $\{\mathbf{x}_1, \mathbf{x}_2, \mathbf{x}_3, \dots, \mathbf{x}_n\}$. The solution function $V(\mathbf{x})$ must also predict the gradients at each geometry. In this perspective, we seek to develop methods based on theory of chemical dynamics to identify important regions of topology of the PESs, thus, we can characterize the critical points associated to those regions. This systematic approach to efficiently use *ab initio* electronic structure theory saves significant amount of time.

1.4 MOLECULAR DYNAMICS SIMULATIONS

Molecular dynamics (MD) simulations is another approach to gain insight into the chemical complexity of combustion processes. In MD simulations one numerically solves the Newton's equations of motion; that is,

$$m_i \frac{d \mathbf{v}_i}{dt} = \mathbf{F}_i, \quad (17)$$

$$\mathbf{F}_i = - \frac{\partial V(\mathbf{x}_1, \mathbf{x}_2, \dots, \mathbf{x}_N)}{\partial \mathbf{x}_i}; \quad (18)$$

where \mathbf{F}_i is the net force imposed upon the i^{th} particle by other particles. This force is derived from a potential energy surface which is a function of Cartesian coordinates of N particles. Determination of a suitable potential energy function, that is, a force field, for a chemical system of interest is essentially the first step in MD simulations method.

Coulombic and van der Waals interactions are the main non-bonded contributions in a force field. These interactions are usually expressed as sum of 1-body, 2-body, 3-body, ... terms; that is,

$$V_{\text{NB}}(\mathbf{x}_1, \mathbf{x}_2, \mathbf{x}_3, \dots, \mathbf{x}_N) = \sum_i u_1(\mathbf{x}_i) + \sum_i \sum_j u_2(\mathbf{x}_i, \mathbf{x}_j) + \sum_i \sum_j \sum_k u_3(\mathbf{x}_i, \mathbf{x}_j, \mathbf{x}_k) + \dots; \quad (19)$$

however, traditionally the 3-body (and higher order) terms are neglected, which is called the pairwise additive assumption; that is, $u_2(\mathbf{x}_i, \mathbf{x}_j) = u_2(x_{ij})$.

The integration time step used in MD algorithms must be chosen such that the trajectories accurately predict the correct physics and conserve the main characteristics of Newton's equations such as time reversibility and conservations of total energy, net angular momentum, and net linear momentum. While trajectories with short time steps are computationally expensive and cover only a small region of the phase space, too large time steps result in violation of energy conservation, and thus unstable simulations. In the former situation, conditions required by ergodic theorem may not be met since time averages are carried out over a short time. As a rule of thumb, it is recommended to pick a time step which is smaller than the fastest time scale in the system—that is associated to bond vibrations in classical MD—by an order of magnitude. However, every choice for a time step should be verified to ensure that the conservation laws are satisfied prior to use it for propagating trajectories.

The velocity-Verlet^{12,13} algorithm is a common integration algorithm. It avoids energy drift, thus long-term energy conservation; however, it gives enormous energy fluctuations from step to step. Given an integration time step of $2\delta t$, the velocity-Verlet algorithm has 4 steps: (1) calculate atomic velocities at time $t + \delta t$ based on the corresponding acting force at time t ; (2) calculate atomic positions at time $t + 2\delta t$ based on the corresponding atomic velocity at time $t + \delta t$; (3) evaluate the acting force on each atom at time $t + 2\delta t$ based on the atomic positions at time $t + 2\delta t$; and (4) calculate atomic velocities at time $t + 2\delta t$ based on the corresponding acting force at time $t + 2\delta t$.

$$\mathbf{v}_i(t + \delta t) = \mathbf{v}_i(t) + \delta t \frac{\mathbf{F}_i(t)}{m_i}, \quad (20)$$

$$\mathbf{r}_i(t + 2\delta t) = \mathbf{r}_i(t) + 2\delta t \mathbf{v}_i(t + \delta t), \quad (21)$$

$$\mathbf{F}_i(t + 2\delta t) = \mathbf{F}_i(\mathbf{r}_1(t + 2\delta t), \mathbf{r}_2(t + 2\delta t), \dots, \mathbf{r}_N(t + 2\delta t)), \quad (22)$$

$$\mathbf{v}_i(t + 2\delta t) = \mathbf{v}_i(t + \delta t) + \delta t \frac{\mathbf{F}_i(t + 2\delta t)}{m_i}. \quad (23)$$

In addition to inaccuracies raised by fitting procedure to construct a reliable force field, the main disadvantage of MD simulations method is the classical approximation,¹⁴ especially neglect of zero-point energy constraints, which can be acceptably accurate for many physical processes but may not accurately describe chemical reactions. Another disadvantage is the fact that the times required for overall reactions to complete far exceed those feasible in MD simulations. Therefore, practically size of a simulated system must be significantly reduced in MD simulations so that the chemistry of interest be within the feasible range simulation times. However, one needs to assess the statistical error to assign significance to results and to determine how well it corresponds to the macroscopic behavior.

Performing classical molecular chemical dynamics¹⁵⁻¹⁷ (CMD) simulations given a relatively accurate reactive force field can provide useful information on how the overall chemistry evolves from reactants to products over a wide range of thermodynamic conditions, assuming the classical approximation is acceptable. This information includes but is not limited to: detection of reactions, intermediates and chemical species; average lifetimes intermediates; reaction mechanisms; transition structures; and the dominant sequences of elementary reactions governing the evolution of the chemistry. However, due to the size and complexity of the data sets produced in the MD simulations the extant analysis methods are inadequate to glean all relevant details of the chemistry. The main challenge and the ultimate aim of this project is how to analyze the MD data sets so that

important details are captured to gain better insight into the complexity of the chemistry. We use the combustion of hydrogen ($\text{H}_2:\text{O}_2$) as the system for perusing our goal, that is, development of new methods to glean details from MD data sets. We seek to describe the behavior of hydrogen combustion, a prototypical complex chemical reaction, in various ranges of initial conditions via CMD simulations performed using a quantum-derived reactive force field. The benefit of employing such a force field in CMD simulations is that it produces complex chemistry, some of which may not be accurate but the overall model is realistic enough for the development of the methods of interest.

1.5 OVERVIEW OF HYDROGEN COMBUSTION MECHANISMS

Perhaps, understanding the non-monotonic explosion limits of $\text{H}_2:\text{O}_2$ mixtures—as schematically illustrated in Figure 1—was the main motivation for development of earlier kinetic mechanisms for hydrogen combustion. It is widely accepted that the lower (first) limit is due to a competition between surface recombination reactions—which remove highly reactive radicals from the system—and formation of radicals which initiate chain reactions.¹⁸⁻²⁰ The H, OH, and O destructions are the most important termination steps observed in the first explosion limit.²¹ Therefore, in the non-explosive region of lower limit, these radicals are destructed immediately after they are formed. As a consequence, chain branching reactions which are responsible for rapidly developing a radical pool do not propagate, and thus explosion will not occur. However, as pressure increases and molecular collisions overtake wall collisions, mixture becomes highly explosive even at relatively low temperatures. It is experimentally proved that the location of first explosion limit in P - T diagram depends on container size and inner surface coating

material.²¹⁻²⁴ Reactions (R4) to (R7) are the main chain branching reactions that have been widely used in many mechanisms.²⁵⁻⁴¹



The second explosion limit is usually explained in term of a competition between chain branching reactions such as (R4) and a non-branching reaction which outruns the chain branching reactions under the thermodynamic conditions of the second limit. Reaction (R8) is a potential candidate for the competing non-branching reaction that has been widely employed in several mechanisms.^{21,25,27}

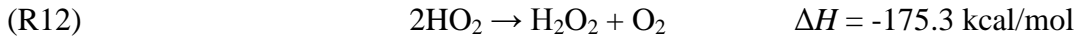
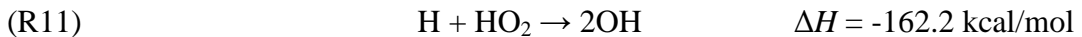


Positive slope of the second explosion limit indicates that at constant temperature, pressure should favor the non-branching reaction, that is, the non-branching reaction is more pressure-sensitive than chain branching reactions. This is the reason that reaction (R8) is usually written as a termolecular reaction by adding a third body M. Existence of a third body also stabilizes produced HO₂ radicals, and thus makes the mixture less reactive (explosive).

The upper (third) explosion limit is due to conversion of relatively inert HO₂ radicals produced by reaction (R8) to relatively unstable species such as H and OH which can be used up in the chain branching reactions ((R4) to (R7)). Reactions (R9) and (R10) are usually considered responsible for such conversions. These reactions are more effective at higher temperatures and lower pressures that agrees with negative slope of the third explosion limit. This explanation was first introduced by Willbourn and Hinshelwood.⁴²

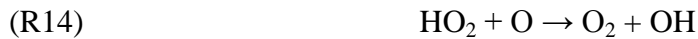


Although the pure chain branching explanation, that is, (R9) and (R10) can perfectly justify existence of the third limit, it has been suggested that thermal explosion is also effective in existence of the third explosion limit.^{26,28} In other words, highly exothermic reactions which consume HO₂ radicals such as reactions (R11) and (R12) heat up the mixture and push it into the explosion regime.



Among the explosion limits, the second limit is critically important since it divides the *P-T* plane into detonation and non-detonation domains. This was first introduced by Belles.⁴³ Later, Dove and Tribbeck⁴⁴ showed that for characterizing the extended second limit (dashed line in Figure 1) reactions involving HO₂ and H₂O₂ must be taken into

account. This was also suggested by Mueller *et al.*³³ Extension of the second explosion limit was experimentally verified by glass vessel experiments.⁴⁵ Reactions (R13) to (R18) are examples of these reactions through which HO₂ and H₂O₂ are consumed by relatively unstable species.



As characterized by several three-step kinetics models of hydrogen combustion^{46,47} (which include initiation, branching, and termination), at extended second explosion limit overall rate of the chain branching reactions ((R4) to (R7)) and non-branching reactions ((R8) and (R13) to (R18)) are equal. Therefore, below the extended second limit, the chain-branching reactions dominate and the mixture is detonating. It should be noted that the exact locations of the explosion limits in *P-T* plane depend on several factors. Wang and Law,²⁴ for instance, recently showed that the upper and lower limits get closer to each other for rich H₂:O₂ mixtures.

There have been too many kinetics schemes developed to model hydrogen combustion. The most well-known and comprehensive models for combustion in open systems with in- and out-flows involve up to 62 reactions with eight or more

species.^{27,29,30,33} However, the most recently developed chemical mechanisms involve networks of twenty or so reactions and cover broader ranges of thermodynamic conditions. Some examples are the models developed by Li *et al.*,³⁴ Óconaire *et al.*,³⁵ and Burke *et al.*³⁷ The models involve large numbers of parameters, some of which cannot be directly determined, but to the extent possible are based on measurements of isolated gas phase reactions. These models have been constructed and parameterized to match measurements of properties such as flame speed, species and concentration profiles in flames, ignition delay times, and other macroscopic processes; all of which are highly averaged bulk processes. Varga *et al.*,⁴⁸ for example, used the results of ignition measurements in shock tubes, rapid compression experiments, and flame velocity measurements to optimize the model developed by Kéromnès *et al.*⁴⁹ However, these models have not been validated for extremely elevated pressures due to experimental limitations. Also, it should be noted that each of these models describes the kinetics of a specific range of thermodynamic conditions and may fail in reproducing experimental results outside that range. For example, models developed by Li *et al.*³⁴ and Óconaire *et al.*³⁵ are the best present models validated over a temperature range of 300-3,000 K and pressure range up to 33 atm according to Strohle and Myhrvold.⁵⁰ On the other hand, the model proposed by Baldwin *et al.*²⁵ is in an agreement with experimental data obtained for rich H₂:O₂ mixtures and thermodynamic conditions near to second limit. Therefore, despite the existence of multiple chemical mechanisms in the literature for hydrogen combustion, no comprehensive model exists to describe its complexity across all ranges of initial conditions.

It must be noted that in none of the above models and mechanisms effects of excited species (either vibrationally or electronically) have been studied. Neglect of this important aspect may significantly reduce the reliability of these models; especially at extremely high temperatures and pressures where vibrational or/and electronic excitations are likely. In the presence of vibrationally excited hydrogen molecules $H_2(v)$, for instance, the main initial radical production source is (R19),⁵¹ while in absence of vibrationally excited species reaction (R20) has been widely suggested for the initiation reaction and reaction (R19) is excluded from the mechanism.^{52,53} The combustion of hydrogen in presence of $O_2(^1\Delta_g)$ has been recently the subject of several experimental studies.⁵⁴⁻⁵⁷ These studies determined that adding just a small percentage of $O_2(^1\Delta_g)$ molecules (even 1%) to the $H_2:O_2$ mixture results in noticeable enhancement of mixture burning, especially when lean fuels are used. In a recent study, Konnov⁵³ proposed a comprehensive mechanism for hydrogen combustion including reactions of excited species $O_2(^1\Delta_g)$ and $OH(^2\Sigma_g^-)$.



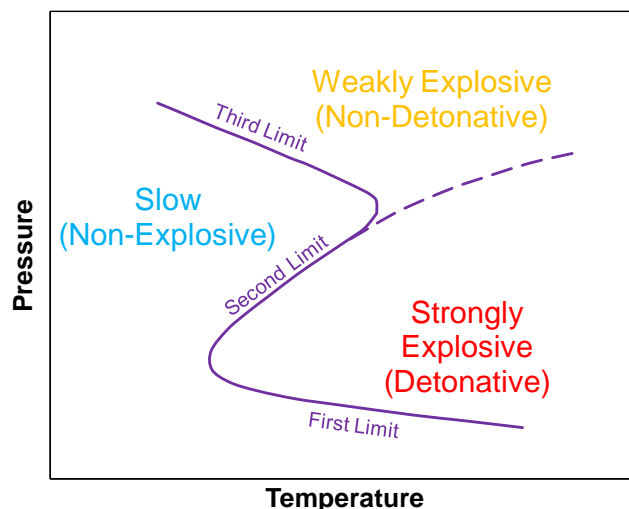


Figure 1.1: A schematic illustration of P - T diagram of explosion limits for $H_2:O_2$ mixtures. The extended second explosion limit is shown in dashed curve is dividing the diagram into strongly explosive and weakly explosive regimes. The exact locations of these limits depend on many factors such as chamber size and composition ratio of the mixture.

1.6 ReaxFF REACTIVE FORCE FIELD

As an attempt to reproduce the complexity of hydrocarbon combustion in MD simulations (C/H/O systems), a quantum-derived reactive force field (ReaxFF) has been developed by van Duin and coworkers.⁵⁸⁻⁶³ ReaxFF can be applied to simulate dynamics of a reactive system of atoms by solving Newton's equations of motion, that is, the classical treatment of reactive chemistry (popularly referred to as Classical Molecular Dynamics as discussed earlier). ReaxFF method uses a bond-order formalism to describe reactive interactions so that it can predict the formation/dissociation of a bond without requiring predefined reaction pathways and expensive quantum mechanics (QM) calculations. Bond order in ReaxFF method determines the connectivity between a pair of

atoms and is empirically calculated based on the interatomic distance of the pair and updated at every integration time step. While bonded interaction energies are calculated using the bond-order formalism, non-bonded interactions such as van der Waals and Columbic interactions are calculated between all pair of atoms, regardless of connectivity. Full functional form of ReaxFF potential can be accessed through the supporting information of Chenoweth *et al.*⁵⁸

In 2011, Agrawalla and van Duin⁶⁴ parametrized the ReaxFF functions for hydrogen combustion (H/O systems). Specifically, they slightly modified the original ReaxFF lone pair potential function reported by Chenoweth *et al.*⁵⁸ in order to account for the non-bonded pair stabilization energy on a single oxygen atom. The force field parameters for H/O systems were optimized against QM data set consisting of transition states and reaction energies relevant to the key reactions of hydrogen combustions listed by Li *et al.*³⁴ The ground-state energy of each bond was considered in the QM training data set. The QM calculations to obtain the training data set were performed using the B3LYP hybrid DFT (density functional theory) functional^{65,66} and the Pople 6-311G** basis set.⁶⁷

Although ReaxFF can, to some extent, reproduce the complexity of chemistry for bulk reactive systems (e.g., H/O systems), it is not, yet, a useful tool to accurately describe the chemistry. Inaccuracies of ReaxFF—and in general, any DFT-adapted force fields—mainly result from the uncertainties in defining comprehensive functional forms for energy which can accurately reproduce energy of a system for all configurations.

The major downside in development of ReaxFF for the H/O systems is that the QM training data set was obtained for reactions of the reduced mechanism of hydrogen combustion reported by Li *et al.*³⁴ As explained in Section 1.2, reduction techniques, in

essence, are not usually reliable tools to completely describe complexity of the chemistry for combustion and bulk systems. Therefore, some chemically important information might not be caught using ReaxFF. However, ReaxFF is, to the best of our knowledge, the only reactive force field that can be used to simulate the chemistry of combustion for bulk systems in a great detail. Therefore, we have used ReaxFF all over this study to perform CMD simulations for an ensemble of sufficient size and time in order explore complexity of hydrogen combustion as a prototype of the hydrocarbon combustions, methane specifically.

1.7 GOALS OF THIS STUDY

Despite existence of so many models for combustion of hydrogen, still we do not have solid theoretical methods to accurately characterize its complexity. Particularly, it is not very clear how a given set of reactants ($\text{H}_2 + \text{O}_2$) at defined initial conditions react *via* a sequence of reactions to produce specific products (H_2O) at predictable final conditions—often called emergent behavior. The dynamics of this evolution from reactants to products is still ambiguous from the microscopic point of view though macroscopically its rate is determined.

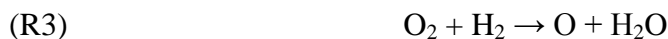
While the currently existing methods require *a priori* developed mechanism as an input, we seek for a method based on atomic level simulations which does not rely on any mechanism. In fact, atomic level simulations output can be directly used to write down a set of master equations for hydrogen combustion to describe its complexity which ultimately leads to construct a more fundamental and comprehensive mechanism.

Due to prohibitive computational costs of quantum dynamics simulations, we will use CMD simulations to explore the complexity of combustion. We will develop tools and methods to analyze the “Big Data” created by MD simulations to glean the details of chemistry from them and gain a better understanding of the emergent behavior in hydrogen combustion. However, while accuracy is not a key for our purpose, we will be cautious about any results and/or predictions reported under classical approximation.

We seek for efficiently taking benefits from electronic structure theory by using the quantum-derived force field, ReaxFF, to perform our CMD simulations. Once the most important molecular events such as reactions are identified from analyzing CMD simulations, we will use electronic structure theory to accurately characterize their potential energy profiles.

2. EARLY CHEMISTRY OF HYDROGEN COMBUSTION¹

Combustion is the result of reactions of radicals, so that characterizing mechanisms of formation of the first radicals is critically important for understanding the overall chemistry. It is important to mention that, while determination of the actual initiation step is critically important to understand the dynamics governing evolution of a chemical system from reactants to products, it is ineffective in determining neither the explosion limits nor the final state of the products.²¹ In 2000 Michael *et al.*⁵² gave a good overview of the initial reactions in H₂:O₂ in their paper on shock tube experiments, *ab initio* calculations, and transition-state theory. They pointed out that at low pressures there are five reactions that can lead to radicals that initiate the chain branching chemistry:



Reactions (R4) and (R5) can be readily dismissed as sources of early radicals because of the energies required relative to the other reactions. Reaction (R3) involves relatively complex bond changes, and although it is the most exothermic of these reactions it has a very high barrier.⁵² Reaction (R2) is generally Woodward-Hoffman⁶⁸ forbidden and

¹ Parts of this Chapter were published as M. Monge-Palacios and H. Rafatijo, On the Role of the Termolecular Reactions $2O_2 + H_2 \rightarrow 2HO_2$ and $2O_2 + H_2 \rightarrow H + HO_2 + O_2$ in Formation of the First Radicals in Hydrogen Combustion: *ab initio* Predictions of Energy Barriers, *Phys. Chem. Chem. Phys.* **19**, 2175 (2017).

cannot be a main source for formation of radicals. However, it should be noted that Woodward-Hoffman rules become less relevant if excited species exist in the mixture.^{69,70} Popov,⁵¹ for instance, postulated that in the presence of vibrationally excited hydrogen molecules, reaction (R2) becomes very important.

For the ground state species, the most likely sources of the initial radicals for the chain initiation are reactions (R1) and (R2). Michael *et al.*⁵² concluded that “only reaction (R1) initiates chain branching in the H₂:O₂ system.” Others, for example, Westbrook⁷¹ in 1982, also suggested this, but Michael *et al.* provided a theoretical basis for it.

Karkach and Oshero⁷² proposed a mechanism involving the termolecular reaction



to explain the discrepancies between their theoretical and the experimental rates for Reaction (R2).⁷³ They postulated that very high pressures and reduced temperatures are needed for the reaction



to be important in the initiation mechanism of hydrogen combustion.

Based on CMD simulations using the ReaxFF force field,⁵⁸⁻⁶⁴ Agrawalla and van Duin⁶⁴ reported mechanisms for hydrogen combustion for various temperatures and pressures, finding that between 3,000 K and 4,000 K and pressures higher than 400 atm

the initial reaction is predominantly Reaction (R1); however, a third body plays an important role:



Our aim in this Chapter is to identify possible initial elementary reactions in a mixture of H₂ and O₂ at the elevated pressures ~4,000 atm and ~5,000 atm using ReaxFF. Although the accuracy of the force field and the classical approximation¹⁴ may not be sufficient to allow definite conclusions about the relative importance of the reactions that produce the early radicals, they can provide qualitative insights into the variety of reactions that might occur in the early stages of the combustion. Thus, we have used the MD simulations to identify all critically important reactions occurring in hydrogen combustion; specifically, the initial reactions.

2.1 REAXFF VALIDATION FOR INTERACTION ENERGIES AND EQUATIONS OF STATE

Since we intend to use ReaxFF for this study, we must be aware of sources of errors which are imposed upon us by ReaxFF and can potentially affect accuracy of the results. In addition, we need to know whether ReaxFF is a reliable tool to be used for our target thermodynamic conditions, that is, pressures ~4,000 atm and ~5,000 atm and temperatures 3,000 K to 5,000 K . Interaction energies are of the important criterion that can be used to validate ReaxFF accuracy. ReaxFF predictions for dimer interaction energy of H₂⋯H₂ and O₂⋯O₂ are compared against the results of high level

wavefunction-based *ab initio* method and the results are shown in panels of Figure 2.1, respectively.

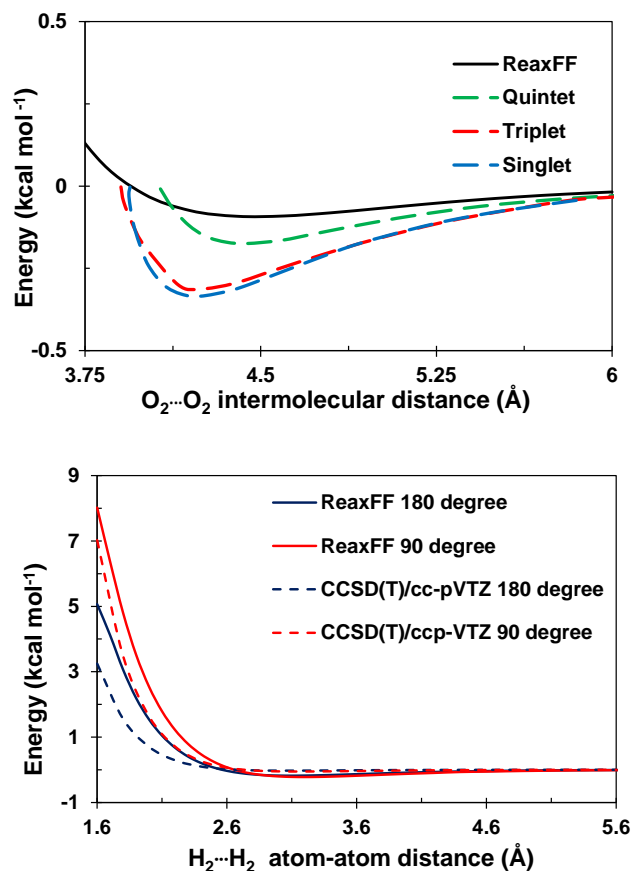


Figure 2.1: Top frame: Comparison of the intermolecular (dimer) potential energy for the linear configuration of two ground state oxygen molecules, that is, $\text{O}_2(^3\Sigma_g^-)\text{-O}_2(^3\Sigma_g^-)$ dimer predicted by ReaxFF (black curve) and the three lowest multiplet spin states for the $\text{O}_2(^3\Sigma_g^-)\text{-O}_2(^3\Sigma_g^-)$ dimer calculated using MRCI with SPACE-1 and B1 basis set reported by Bartolomei *et al.*⁷⁴ Bottom frame: Comparison of $\text{H}_2\cdots\text{H}_2$ interaction energy predicted by ReaxFF (solid curves) and the results of CCSD(T)/cc-pVTZ (dashed curves) for linear (blue) and perpendicular (red) configurations.

Figure 2.1 (the top panel) shows that not only does ReaxFF fail in prediction of PES splitting phenomena for two interacting ground state oxygen molecules, that has been the subject of many experimental and theoretical studies,⁷⁴⁻⁷⁹ but it also does not provide an accurate description of interaction energy for dimer systems as simple as H₂⋯H₂ (bottom panel). The discrepancies between ReaxFF predictions for the intermolecular interaction energies and results of electronic structure *ab initio* calculations subsequently cause errors in predictions of collision frequencies.

We performed calculations in LAMMPS 2014^{80,81} to determine how well ReaxFF predicts the equations of state (EOS) for H₂ and O₂ as indirect evidence of the accuracy of the collision frequency predictions. We computed the pressure-density isotherms (P - ρ ; T) for H₂ and O₂ by simulating the NVT ensemble with 2,500 molecules in cubic simulation boxes with volumes 55×55×55 Å³, 75×75×75 Å³, 85×85×85 Å³, 95×95×95 Å³ and 105×105×105 Å³, and temperatures 300 K, 500 K and 1,000 K. For O₂ simulations, three more temperatures of 2,000 K, 3,000 K, and 4,000 K were also considered.

The temperature is controlled in the simulations by the Nosé-Hoover thermostat.^{82,83} The temperature was always close to the target value; for example, at 1,000 K temperature fluctuates in the 950 K – 1050 K interval. These fluctuations are not large for the goals of this work. Pressure is computed in LAMMPS from the virial expansion⁸⁴

$$P = \frac{NkT}{V} + \frac{\sum_i^N \mathbf{f}_i \cdot \mathbf{r}_i}{dV}, \quad (1)$$

where N is the number of atoms, κ is the Boltzmann constant, T is temperature, d is the dimensionality of the system (3 for a cubic simulation box), V is the volume, and \mathbf{f}_i is the force exerted on the i^{th} particle located at position \mathbf{r}_i . Then, the fluctuations of pressure are due not only to temperature, but also to changes in the configuration of the system through the atomic positions, \mathbf{r}_i , and forces, \mathbf{f}_i as appeared in Eq. (1). As a result, pressure fluctuation amplitudes are larger than that of the temperature. This is the reason we performed NVT simulations and expressed results in terms of density which is fixed during the simulations while pressure widely fluctuates around an average value.

We examined ReaxFF prediction for EOS of hydrogen over the predictions of the truncated virial-type equation reported by Lemmon *et al.*,⁸⁵ which are in a good agreement with the results in the NIST Standard Database.⁸⁶ The EOS expression developed by Lemmon *et al.* is for the temperature interval 150 K to 1,000 K and pressure up to 200 MPa with an uncertainty of 0.15% at lower temperatures.⁸⁵ The P - ρ isotherms computed using ReaxFF (solid curves) are compared with those computed using Lemmon *et al.*'s expression (dotted curves) in Figure 2.2 (top). The relative errors of ReaxFF predictions for EOS of hydrogen that is illustrated in Figure 2.2 (bottom) shows that ReaxFF generally underestimates the P - ρ isotherms for hydrogen over the density range of 8-50 kg·m⁻³ and temperature range of 300-1,000 K. However, ReaxFF reproduces very well the thermodynamic data⁸⁵ at lower densities, with the best agreement at lower densities and higher temperatures. For example, at 1,000 K the relative errors are in the range 0.7 % - 8.5 %.

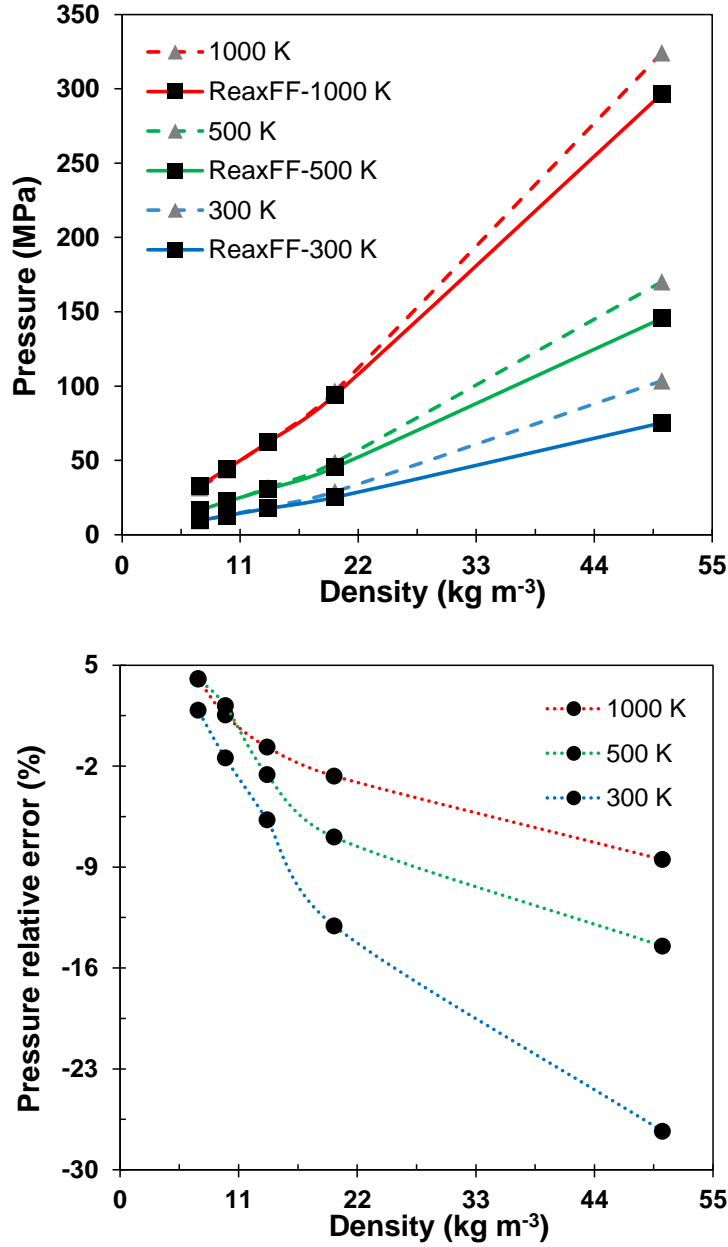


Figure 2.2: Top frame: Comparison of the results for the EOS of H₂ predicted by ReaxFF (solid curves) and the empirical equation reported by Lemmon *et al.* (dashed curves) at different temperatures: 300 K (red), 500 K (green) and 1,000 K (blue). Bottom frame: relative error in ReaxFF prediction of pressure for H₂ at different temperatures of the top frame.

The ReaxFF-computed P - ρ isotherms (solid curves) for O_2 are compared with results reported by Kuznetsov *et al.*⁸⁷ (dotted curves) in Figure 2.3 (top frame). The Kuznetsov *et al.* empirical equation was derived from the thermodynamic data reported by Sychev *et al.*⁸⁸ In contrast to the case for hydrogen, ReaxFF generally overestimates the P - ρ isotherms for oxygen over the density range of 130-330 $kg \cdot m^{-3}$ and temperature range of 300-4,000 K as shown in Figure 2.3 (bottom frame) for the relative errors. However as is the case for H_2 , the agreement is better at the lower densities and the higher temperatures. Based on these results we expect that at densities below 350 $kg \cdot m^{-3}$ and temperatures 3,000 K and higher ReaxFF will predict acceptably accurate $O_2 + O_2$, $H_2 + H_2$, and $O_2 + H_2$ collision frequencies.

It is important to note that extreme thermodynamic conditions such as high densities intensify the inaccuracies of ReaxFF predictions for EOS (see Figs. 2.2 and 2.3). This is mainly due to the failure of ReaxFF assumption of pairwise additive for calculation of energy at high densities and pressures when many-body interaction energies become important.

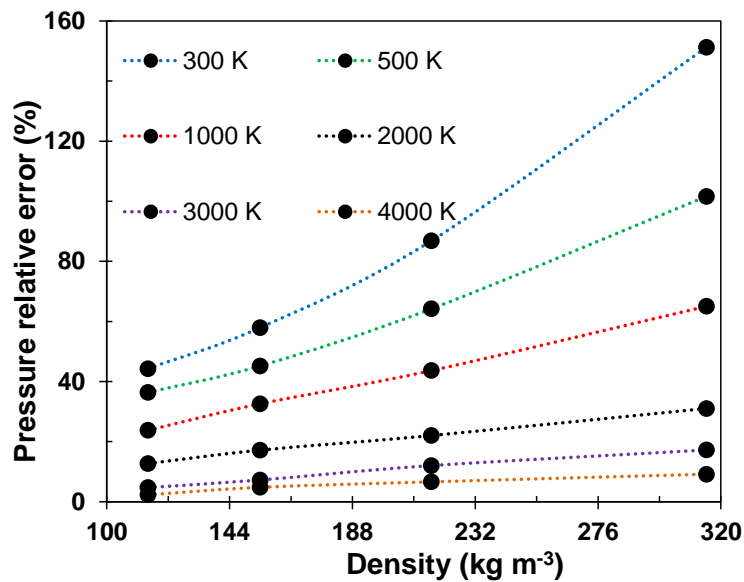
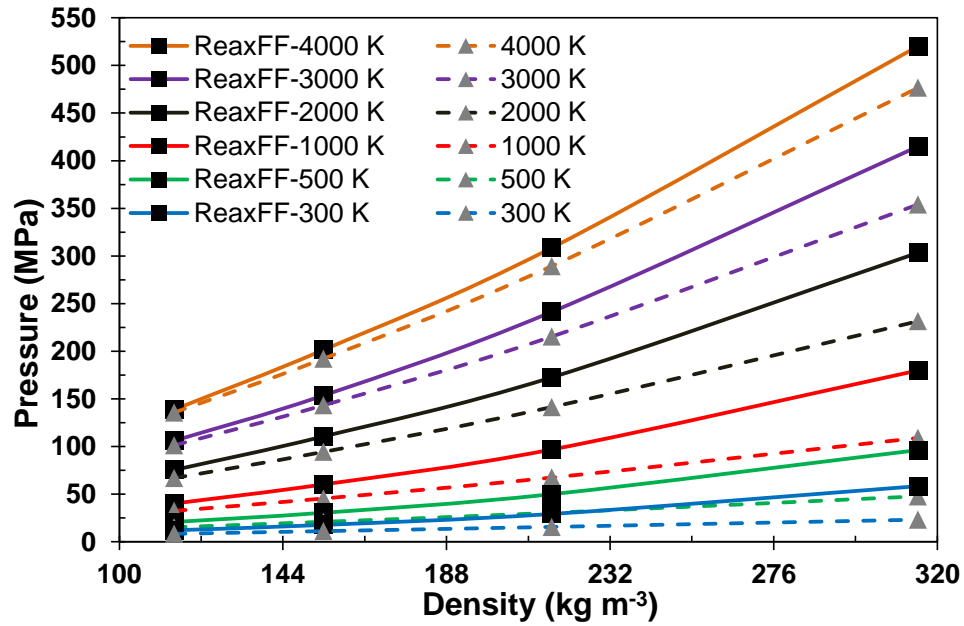


Figure 2.3: Top frame: Comparison of the results for the EOS of O_2 predicted by ReaxFF (solid curves) and the empirical equation reported by Kuznetsov *et al.* (dashed curves) at different temperatures. Light blue: 300 K, violet: 500 K, pink: 1,000 K, dark blue: 2,000 K, green: 3,000 K and red: 4,000 K. Bottom frame: Relative error in ReaxFF prediction of pressure for O_2 at different temperatures of previous frame.

2.2 COMPUTATIONAL METHODS

2.2.1 SIMULATION DETAILS

Molecular dynamics simulations were performed using the 2014 version of the LAMMPS code with ReaxFF as the reactive force field parametrized for hydrogen combustion systems. The simulations were performed with canonical ensembles, that is, fixed number of atoms (N), fixed volume (V), and fixed temperature (T)—referred to as NVT. We simulated a total number of 100 molecules of H_2 and O_2 for composition ratios $[H_2]/[O_2] = 0.25-2$, the density range of $120.2-332.7 \text{ kg}\cdot\text{m}^{-3}$, and temperature inputs of 3,000 K, 4,000 K, and 5,000 K in a cubic cell with periodic boundary conditions (for composition ratios $[H_2]/[O_2] = 1$ and 2 only the density interval of $177.7-332.7$ was studied). For each composition ratio, the size of the simulation box was varied to cover the density interval of $120.2 \text{ kg}\cdot\text{m}^{-3}$ to $332.7 \text{ kg}\cdot\text{m}^{-3}$. Therefore, 60 sets of initial conditions in the (composition, temperature, density) space were studied. For each set of initial conditions an ensemble of 50 trajectories was run to cover a large region of the phase space. In some cases an additional 20 trajectories were run to lower the margin of error.

We first began with running an equilibration simulation. Initial configuration of reactants for each simulation was generated using PACKMOL⁸⁹ code that distributes all molecules homogeneously in a box with periodic boundaries such that all non-bonding interatomic distances were at least 2.2 \AA . These initial configurations were adjusted by using the Polak-Ribiere⁹⁰ version of the conjugate gradient algorithm for energy minimization, until either the energy, $1\times 10^{-4} \text{ kcal/mol}$, or the force criterion, $1\times 10^{-6} \text{ kcal/mol \AA}^{-1}$, was satisfied. This resulted in all H_2 and O_2 reactants covalent bond

distances being at their equilibrium lengths: 0.759 Å and 1.188 Å, respectively. Atomic velocities were selected from Gaussian distributions corresponding to the input temperatures of 3,000 K, 4,000 K, and 5,000 K. The temperature was controlled by a Nosé-Hoover thermostat^{82,83} with damping constant 500 fs. The trajectories were propagated using the velocity Verlet algorithm^{12,13} with time step 0.1 fs. The equilibration in the system was checked by calculation of the average kinetic temperatures of the molecules; that is, rotational, vibrational, and translational. While the rotational and translational kinetic temperatures rapidly merged to input thermodynamics temperature, it took up to 20 ps (10 ps) for the vibrational kinetic temperature to equilibrate at 3,000 K (5,000 K). If a reaction was occurred during equilibration, the simulation was abandoned. It must be noted that the time required for complete equilibration depends on both density and temperature, that is, at higher densities or/and temperatures equilibration was completed very fast; see the time scales given above for 3,000 K and 5,000 K. Figures 2.4 and 2.5 show the time required for a complete equilibration in a typical simulation at 3,000 K for H₂ and O₂, respectively.

The configurations of the system at the end of the equilibration simulations were used as the initial states to produce simulations (without minimization) which were run for 6 ns to ensure observation of an initial reaction; however, at 4,000 K and 5,000 K, the initial reaction usually occurred within the 250 ps of the beginning of the simulation. Since those trajectories were initiated with different initial atomic velocities and configurations, a wide spectrum of the phase space was covered. The analysis of simulations was stopped after we observed the first reaction to prevent the NVT ensemble being affected by the thermochemistry.

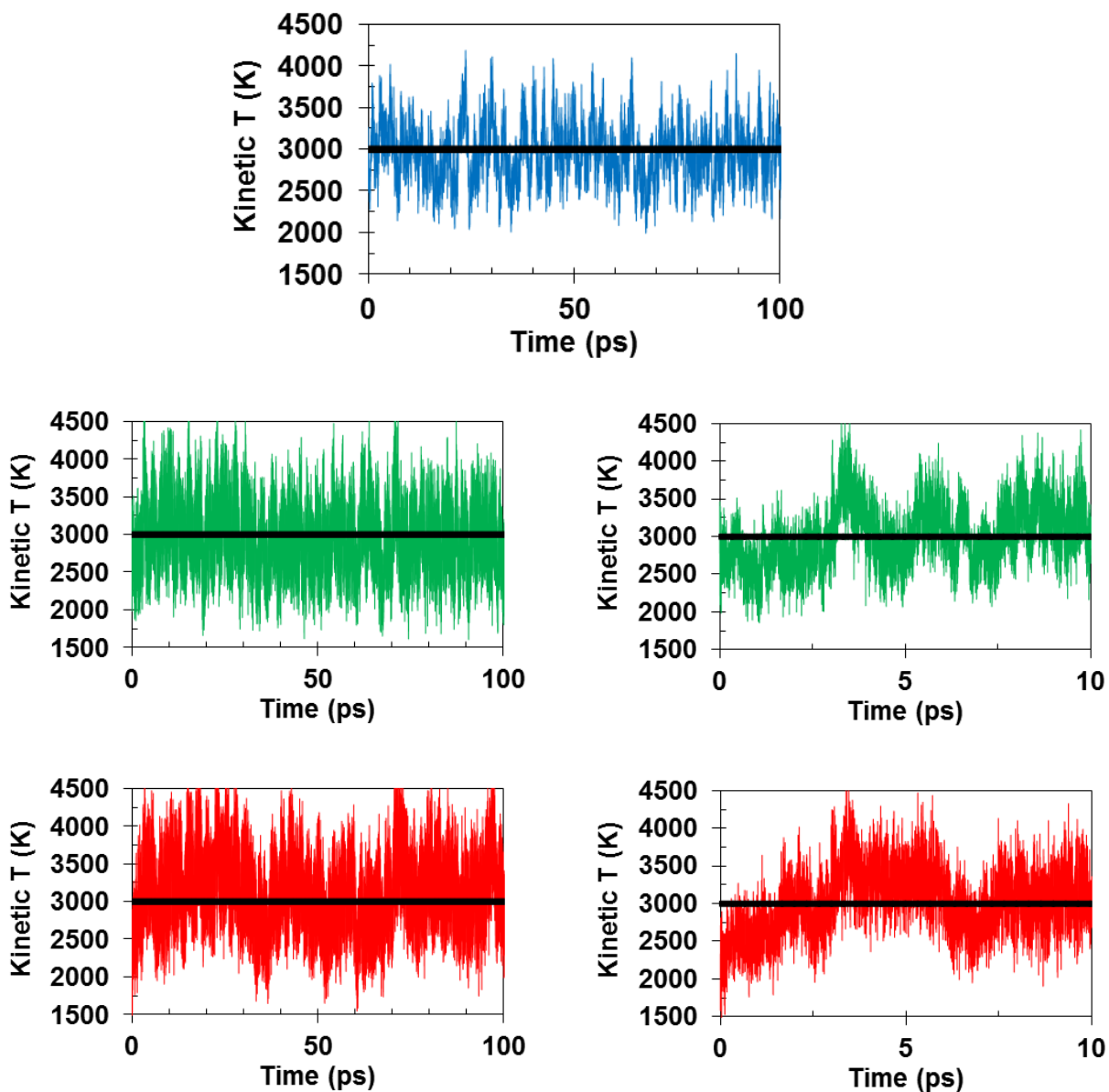


Figure 2.4: The average translational (top frame), rotational (middle frames), and vibrational (bottom frames) kinetic temperatures of hydrogen molecules during the first 100 ps of a typical simulation at thermodynamic temperature of 3,000 K, 276.3 kg·m⁻³, and composition ratio of $[H_2]/[O_2] = 1$. For the rotational and vibrational parts, kinetic temperature was also plotted during the first 10 ps to show the completion of the equilibration (right frames). The target thermodynamic temperature is shown by a horizontal black line.

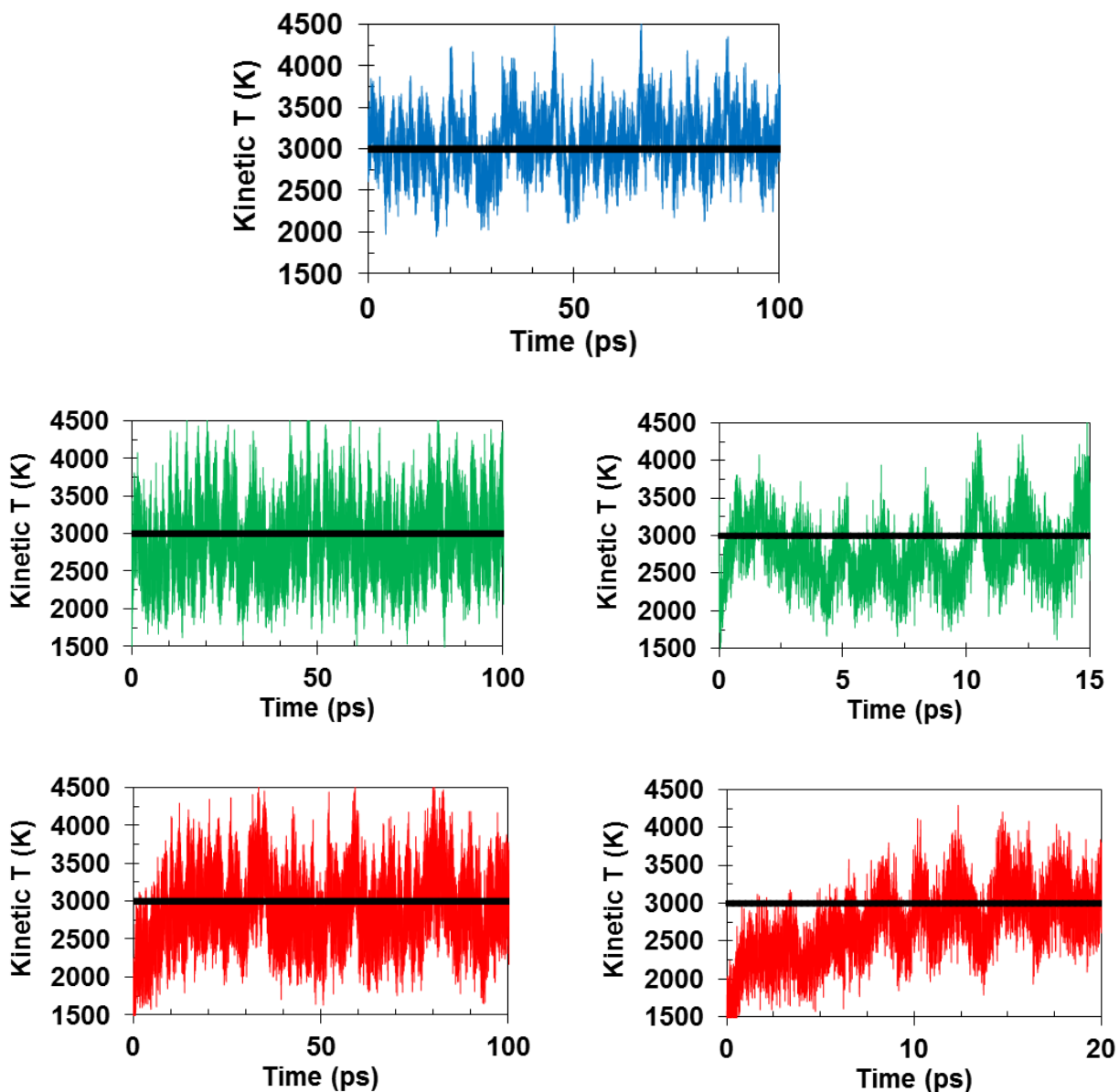


Figure 2.5: The average translational (top frame), rotational (middle frames), and vibrational (bottom frames) kinetic temperatures of oxygen molecules during the first 100 ps of a typical simulation at thermodynamic temperature of 3,000 K, 276.3 kg·m⁻³, and composition ratio of $[H_2]/[O_2] = 1$. For the rotational and vibrational parts, kinetic temperature was also plotted during the first 15 and 20 ps, respectively, to show the completion of the equilibration (right frames). The target thermodynamic temperature is shown by a horizontal black line.

2.2.2 REACTION IDENTIFICATION ALGORITHM

We developed an algorithm to identify reactions by monitoring the atom-atom distances. The first step to accurately identify a reaction and all involved chemical species is to determine the molecularity the reaction. A termolecular or higher molecularity collision is in essence a sequence of two or more bimolecular collisions that occur sufficiently close in time that the chemical changes can be considered to be a single event. A practical definition of molecularity can be based on arbitrary criteria of reactants being within covalent ranges. Thus, we monitored inter-atomic distances to identify groups of atoms, which we call clusters, that are involved in a reaction. In this definition an n -molecular collision results from a corresponding n -molecular doubly connected cluster^{91,92} in which connections between pairs are determined by an inter-atomic cutoff distance. In the cluster representation each molecule is represented by a point, and lines illustrate interactions (connections) between them. In a doubly connected cluster diagram there are at least two independent non-crossing paths between each pair of molecules; thus, a bimolecular collision cluster is a cluster in which two chemical species are within defined atom-atom cutoff distances and a termolecular collision cluster is one where three species are within the defined atom-atom cutoff distances. The initial conditions chosen for this study were such that the probability of collisions of molecularity greater than two is expected to be large enough for chemistry to begin on the timescale of the simulations.

Knowing composition of a system, we categorized covalent bonds into various groups based on: (1) bond elements (H-H, O-O, and O-H for our system); and (2) chemical species. O-H bond, for example, exists in various species such as H₂O, HO₂, OH, etc., each of which was considered as a different group. For each bond group, we defined a

cutoff interatomic distance beyond a bond was considered ruptured. These cutoff interatomic distances were set to be within 1 kcal/mol of the asymptotic limit of the bond dissociation energy curves (as predicted by ReaxFF), where the gradient of dissociation potential energy curves become zero. For example, the cutoff interatomic distance for a covalent O-O bond in O₂ is 2.3 Å, and for an H-H bond in H₂ is 1.5 Å; both obtained from the corresponding potential energy dissociation curves (see Figure 2 in Agrawalla and van Duin⁶⁴). The initiation of a reaction was identified by the rupturing of a bond. Molecular bond lengths were checked every 0.5 fs, and when a bond length exceeded the corresponding cutoff interatomic distance, it was assumed that a reaction was underway. Then, all the molecules surrounding the two fragments of the rupturing bond were identified using critical cutoff values 3.0 Å, 1.8 Å, and 3.5 Å for the non-bonding atom-atom distances for H···H, H···O, and O···O, respectively. This identified the collision complex, and then the evolution of internuclear distances were analyzed for the collision complex beginning 210 fs before the time at which the bond rupture was detected. The cutoff values used to identify the collision clusters were selected as distances at which non-bonded atoms interact with energy greater than 1 kcal/mol, according to the H···H, H···O, and O···O non-bonded interatomic potential energy curves. A new bond is considered as formed if atom-atom distance between its elements oscillates for at least two inner turning points of the motion near the equilibrium bond-length after the bond breaking was detected. Once a reaction completed and products became identifiable, the composition of the system was updated, and so was the bond group information.

There is an exception to the approach described above and that is when a reaction involves only bond forming events. This situation, usually, occurs when radicals are

reacting. To account for these reactions, non-bonding interatomic distances of each atom in a radical with all other atoms in the system were calculated every 0.5 fs and the evolutions were monitored. A bond was considered as formed between a radical atom and another atom if a non-bonding interatomic distance oscillated around the equilibrium bond-length of the presumptive bond group for duration of 15 fs. The schematic flowchart of the algorithm is presented in Figure 2.6.

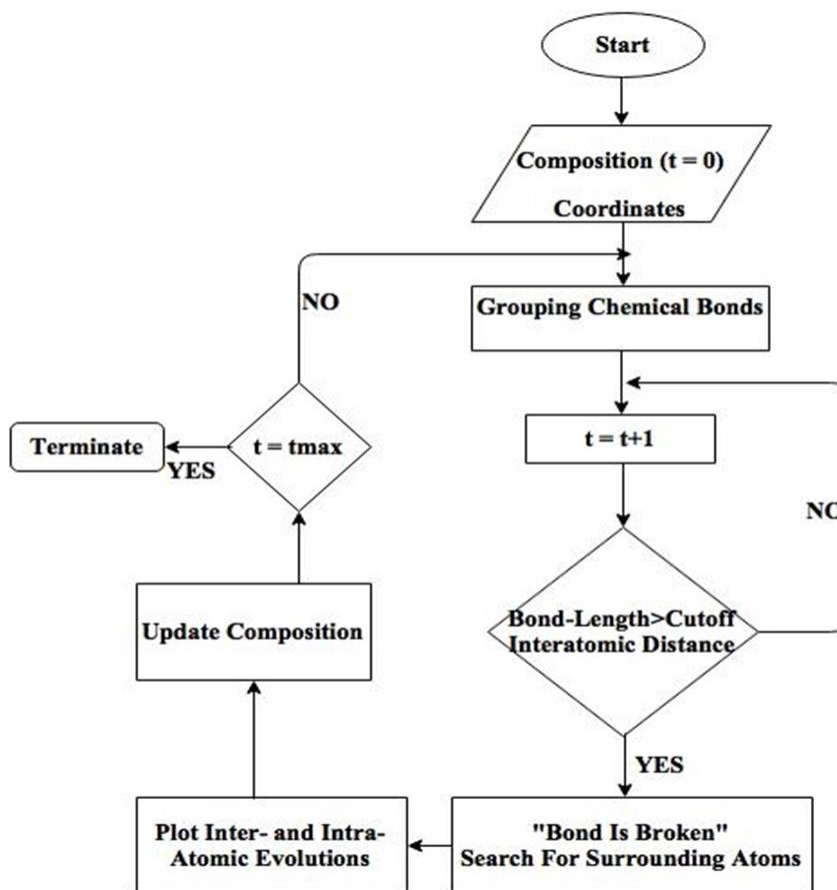


Figure 2.6: The reaction identification algorithm flowchart.

2.3 INITIAL REACTIONS

Here, we made use of the reaction identification algorithm to identify the main reactions that produces initial radicals. The simulations showed that initial reactions

mainly began with breaking of an H-H bond. If two H-atoms of the broken H_2 molecule were simultaneously within 1.8 \AA to one of the oxygen atoms of two different O_2 molecules, and the resulting products are 2HO_2 , the reaction was identified as $2\text{O}_2 + \text{H}_2 \rightarrow 2\text{HO}_2$. If only one hydrogen atom was within that cutoff distance, and the resulting products are $\text{H} + \text{HO}_2$, the reaction was identified as $\text{O}_2 + \text{H}_2 \rightarrow \text{H} + \text{HO}_2$.

The simulations predicted three reactions that produce radicals. In addition to the bimolecular reaction $\text{O}_2 + \text{H}_2 \rightarrow \text{H} + \text{HO}_2$ two termolecular reactions were identified: $\text{O}_2 + \text{H}_2 + \text{M} \rightarrow \text{H} + \text{HO}_2 + \text{M}$ (with M being either O_2 or H_2) and $2\text{O}_2 + \text{H}_2 \rightarrow 2\text{HO}_2$. It must be noted that at 3,000 K, these reactions contribute 95% of initial reaction, and as temperature increases to 5,000 K, this contribution reduces to 80%. We identified four different pathways for $2\text{O}_2 + \text{H}_2 \rightarrow 2\text{HO}_2$: (a) A synchronous pathway $2\text{O}_2 + \text{H}_2 \rightarrow 2\text{HO}_2$; (b) an asynchronous pathway $2\text{O}_2 + \text{H}_2 \rightarrow 2\text{HO}_2$; (c) an indirect pathway $2\text{O}_2 + \text{H}_2 \rightarrow \text{HO}_2 \cdots \text{HO}_2 \rightarrow \text{H}_2\text{O}_2 + \text{O}_2$; and (d) an indirect pathway $2\text{O}_2 + \text{H}_2 \rightarrow \text{HO}_2 \cdots \text{HO}_2 \rightarrow 2\text{HO}_2$. The interatomic distances as functions of time for typical trajectories resulting in these pathways are shown, respectively, in Figures 2.7, 2.8, 2.9, and 2.10.

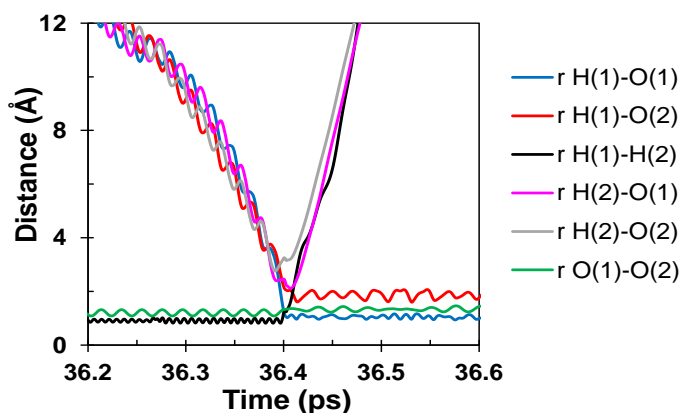


Figure 2.7: The evolution of interatomic distances for a typical trajectory of the bimolecular reaction $\text{O}_2 + \text{H}_2 \rightarrow \text{H} + \text{HO}_2$.

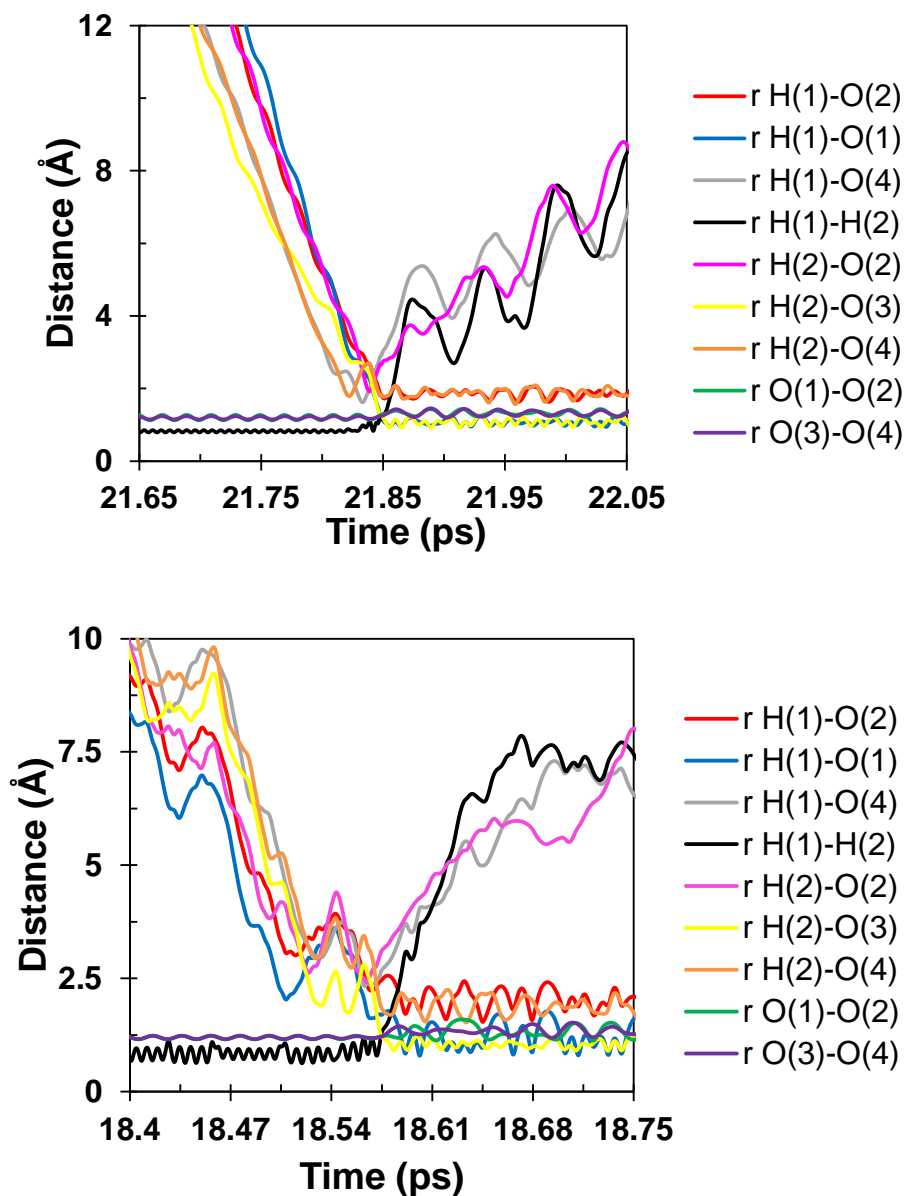


Figure 2.8: Top frame: The evolution of interatomic distances for a typical trajectory of the synchronous termolecular reaction $2\text{O}_2 + \text{H}_2 \rightarrow 2\text{HO}_2$. Bottom frame: The evolution of interatomic distances for a typical trajectory of the asynchronous termolecular reaction $2\text{O}_2 + \text{H}_2 \rightarrow 2\text{HO}_2$.

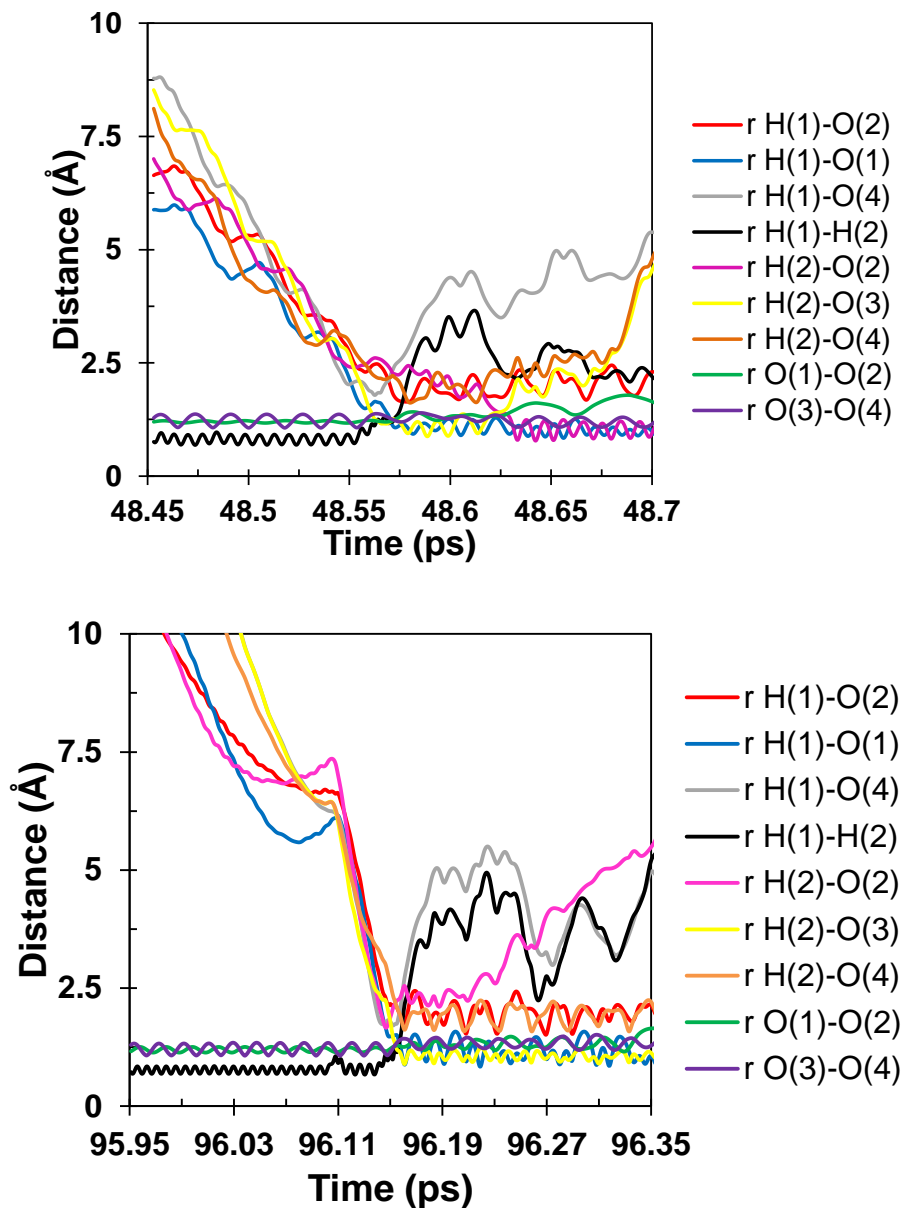


Figure 2.9: Top frame: The evolution of interatomic distances for a typical trajectory of indirect termolecular reaction $2\text{O}_2 + \text{H}_2 \rightarrow \text{HO}_2 \cdots \text{HO}_2 \rightarrow \text{H}_2\text{O}_2 + \text{O}_2$. Bottom frame: The evolution of interatomic distances for a typical trajectory of indirect termolecular reaction $2\text{O}_2 + \text{H}_2 \rightarrow \text{HO}_2 \cdots \text{HO}_2 \rightarrow 2\text{H}_2\text{O}$.

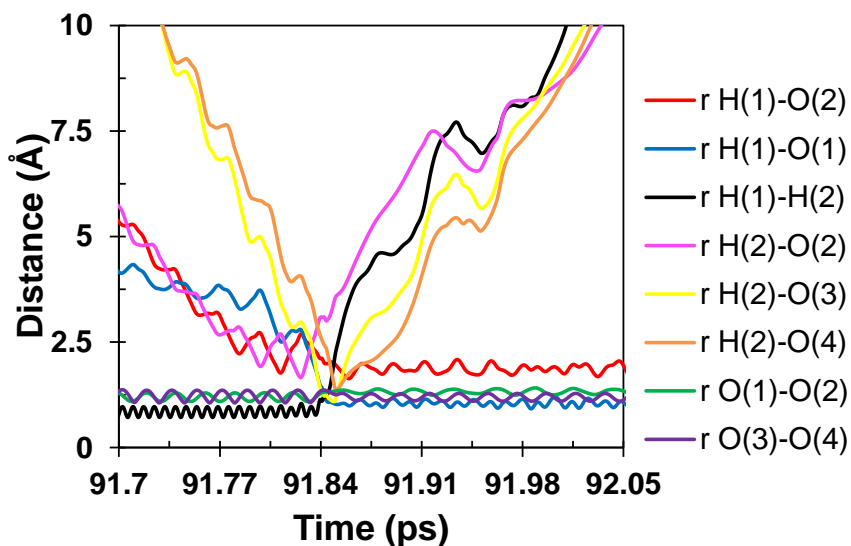


Figure 2.10: The evolution of interatomic distances for a typical trajectory of the termolecular reaction $2\text{O}_2 + \text{H}_2 \rightarrow \text{H} + \text{HO}_2 + \text{O}_2$ in which one O_2 molecule acts as a third body.

Comparisons of the plots in top and bottom frames of Figure 2.8 clearly illustrate two distinct pathways that produce 2HO_2 . In the asynchronous pathway, bottom frame of Figure 2.8, there is a significant gap between the times of the formation of the two HO_2 radicals; one HO_2 radical is formed with one H-atom and one of the O_2 molecules, and the other H-atom subsequently reacts with the second oxygen molecule, forming the second HO_2 radical. To distinguish between the two $2\text{O}_2 + \text{H}_2 \rightarrow 2\text{HO}_2$ pathways we examined in the O–H and H–H bond distances as functions of time in the collision cluster. It can be seen in the top frame of Figure 2.8 for the synchronous pathway that at $t \approx 21.85$ ps two O–H bonds are formed (yellow and blue curves) as the H–H bond (black curve) is broken. In the asynchronous pathway, the bottom frame of Figure 2.8 the collision cluster is formed at $t \approx 18.57$ ps, where the O–H bonds distances (yellow and

blue curves) are about 1.1 Å and 1.6 Å while the H–H bond length (green curve) is about 1.3 Å. There is sequential formation of the two HO₂ radicals, with the second being formed about 15 fs after the first.

The asynchronous pathway is essentially a one-step process. The H–H bond is not completely broken before the second HO₂ is formed, and the bond length of the O₂ (purple curve in the bottom frame of Figure 2.8) that will be part of the second HO₂ radical is significantly increased right after the formation of the first HO₂ radical (blue curve). That is, it is a concerted termolecular process rather than a two-step mechanism as proposed by Cheng *et al.*,⁹³ who concluded that the $\text{H} + \text{O}_2 \rightarrow \text{HO}_2$ reaction occurs quickly following $\text{H}_2 + \text{O}_2 \rightarrow \text{H} + \text{HO}_2$. We also observed that sequence of reactions; however, this is not the case of the asynchronous pathway that we characterize as a single termolecular reaction rather than two bimolecular reactions.

We have used distance criteria to distinguish between the asynchronous termolecular pathway and the two-step process described by Cheng *et al.*⁹³ Based on what was previously discussed, we characterized a collision cluster as termolecular when the two H···O intermolecular distances are simultaneously less than or equal to the cutoff distance of 1.8 Å, the ReaxFF distance criterion (see Figure 5 in Agrawalla and van Duin⁶⁴); otherwise, it was identified as bimolecular.

We observed an indirect reaction that takes place through the intermediate complex HO₂···HO₂ formed in the post-transition state region. The top frame of Figure 2.9 shows the evolution of the interatomic distances as functions of time for a typical trajectory of this pathway. The distances between the terminal oxygen atom of one of the HO₂ radicals and the hydrogen atom of the other HO₂ radical are shown by the pink and gray curves,

respectively. At about $t \approx 48.57$ ps, two HO₂ radicals are formed, but they remain together because of the formation of an O–H hydrogen bond (pink curve). The complex is formed at about $t \approx 48.60$ ps by the bonding of the terminal O-atom of one of the HO₂ radicals with the H-atom of the other HO₂ radical (pink curve). The interatomic separation immediately (within about 5.14 ps) shortens as the O–H bond (yellow curve) is broken at $t \approx 48.65$ ps. The overall result is $2\text{O}_2 + \text{H}_2 \rightarrow \text{HO}_2 \cdots \text{HO}_2 \rightarrow \text{H}_2\text{O}_2 + \text{O}_2$. The self-reaction of HO₂ to produce H₂O₂ + O₂ has been reported by Kéromnès *et al.*⁴⁹ as an inhibitor of reactivity under low-temperature and high-pressure conditions. Stockwell⁹⁴ has pointed out that it is an important source of H₂O₂ in atmospheric chemistry. Both termolecular reaction and the indirect pathway $2\text{O}_2 + \text{H}_2 \rightarrow \text{HO}_2 \cdots \text{HO}_2 \rightarrow \text{H}_2\text{O}_2 + \text{O}_2$, are likely important at high pressures.

Zhou *et al.*⁹⁵ reported CASPT2/CBS/aug-cc-pVTZ results that characterized the saddle point region of the triplet PES for $\text{HO}_2 + \text{HO}_2 \rightarrow \text{H}_2\text{O}_2 + \text{O}_2$ reaction; which indicates an indirect mechanism through an intermediate complex with a doubly hydrogen-bonded ring structure similar to that predicted by ReaxFF as illustrated in the top panel of Figure 2.9. They found that there is no potential barrier to the formation of the complex, which they predict to be bound by 9.79 kcal/mol. This complex, which forms in the entry channel, is responsible for the shift of the activation energy from negative at low temperatures to positive at high temperatures that results in an Arrhenius curve for the $\text{HO}_2 + \text{HO}_2 \rightarrow \text{H}_2\text{O}_2 + \text{O}_2$ reaction with a minimum at around 800 K. Zhou *et al.*⁹⁵ pointed out an enhancement of the computed rate coefficient for $\text{HO}_2 + \text{HO}_2 \rightarrow \text{H}_2\text{O}_2 + \text{O}_2$ with increasing pressure, which is more significant at low temperatures. Kircher *et al.*⁹⁶ observed enhancement of the rate constant with pressure in flash

photolysis/UV absorption experiments. This is presumably due to the collisional stabilization of the $\text{HO}_2\cdots\text{HO}_2$ complex. If the complex is stabilized the indirect pathway $2\text{O}_2 + \text{H}_2 \rightarrow \text{HO}_2\cdots\text{HO}_2 \rightarrow \text{H}_2\text{O}_2 + \text{O}_2$ will be favored over dissociation to 2HO_2 . We observed the dissociation of the $\text{HO}_2\cdots\text{HO}_2$ complex in the simulations. A typical trajectory is illustrated in the bottom frame of Figure 2.9, where the pink and gray curves represent the two inter-radical $\text{O}\cdots\text{H}$ bonds as functions of time. The complex begins to dissociate at around 96.27 ps as one of the $\text{O}\cdots\text{H}$ bonds (purple curves) breaks. The overall reaction is $2\text{O}_2 + \text{H}_2 \rightarrow \text{HO}_2\cdots\text{HO}_2 \rightarrow 2\text{HO}_2$.

2.4 EFFECTS OF DENSITY

Plots of the probability of finding the reactions $\text{O}_2 + \text{H}_2 \rightarrow \text{H} + \text{HO}_2$ (dashed lines) and $2\text{O}_2 + \text{H}_2 \rightarrow 2\text{HO}_2$ (solid lines) occurring as initial reactions as functions of density for composition ratios (a) $[\text{H}_2]/[\text{O}_2] = 0.25$, (b) $[\text{H}_2]/[\text{O}_2] = 0.5$, (c) $[\text{H}_2]/[\text{O}_2] = 1$ and (d) $[\text{H}_2]/[\text{O}_2] = 2$ at 3,000 K (blue), 4,000 K (green), and 5,000 K (red) are shown in Figure 2.11. The density changes were effected by varying the volume of the simulation box. The reaction $\text{O}_2 + \text{H}_2 \rightarrow \text{H} + \text{HO}_2$ is the most prevalent initial reaction over a broad range of densities. However, at 3,000 K and $\rho > 250.0 \text{ kg}\cdot\text{m}^{-3}$ the reaction $2\text{O}_2 + \text{H}_2 \rightarrow 2\text{HO}_2$ becomes dominant. At 4,000 K and 5,000 K the probability of $2\text{O}_2 + \text{H}_2 \rightarrow 2\text{HO}_2$ increases with increasing density, although not to the extent that it does at 3,000 K. In fact, at 4,000 K and 5,000 K the termolecular reaction does not become the initiation reaction mechanism at any of the density values studied. We justified this competitive behavior between ter- and bi-molecular reactions, as shown in the panels of Figure 2.11, in context of collision theory of the gases.

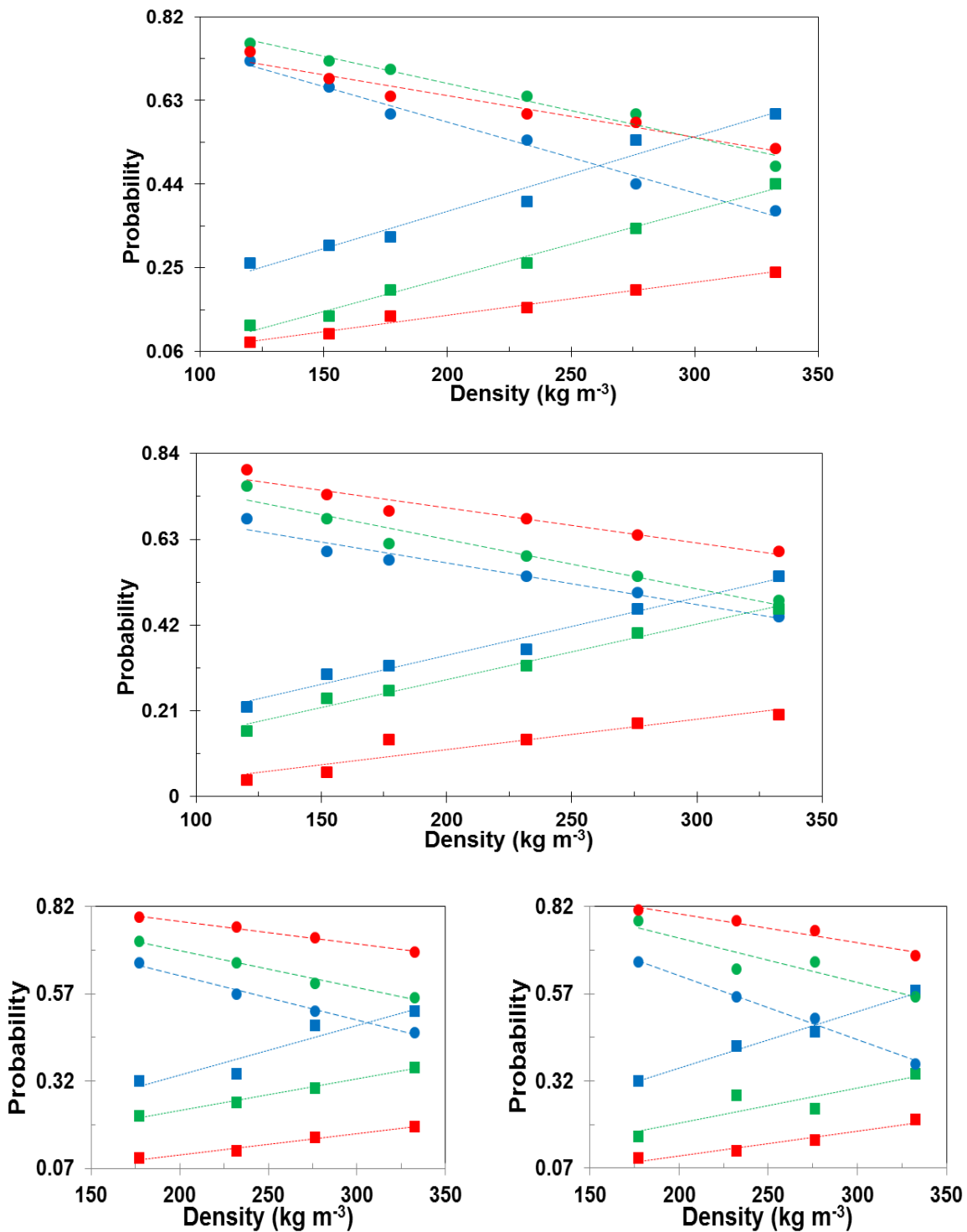


Figure 2.11: Probabilities of the $O_2 + H_2 + (M) \rightarrow H + HO_2 + (M)$ (dashed trend-lines) and $2O_2 + H_2 \rightarrow 2HO_2$ (dotted trend-lines) reactions occurring as initial reactions as functions of density for composition ratios (top frame) $[H_2]/[O_2] = 0.25$, (middle frame)

$[\text{H}_2]/[\text{O}_2] = 0.5$, (bottom left) $[\text{H}_2]/[\text{O}_2] = 1$ and (bottom right) $[\text{H}_2]/[\text{O}_2] = 2$ at 3,000 K (blue), 4,000 K (green), and 5,000 K (red). The density changes were effected by varying the volume of the simulation box. The margins of error were calculated using $error = Z\sqrt{([P(1 - P)]/N)}$, where Z is 1.645 to give 90% level of confidence, P is the reaction probability, and N is the number of trajectories run for a given set of initial conditions. In most cases ensembles of 50 trajectories were run, but in some cases an additional 20 trajectories were run to lower the margin of error. The average of the error over all data points is ± 0.09 .

2.4.1 COLLISION FREQUENCY

We computed average collision frequency and average collision duration for the $\text{H}_2\cdots\text{O}_2$ and $\text{O}_2\cdots\text{H}_2\cdots\text{O}_2$ collisions for the composition ratio of $[\text{H}_2]/[\text{O}_2] = 0.25$ and density range of $120.2 \text{ kg}\cdot\text{m}^{-3}$ to $332.7 \text{ kg}\cdot\text{m}^{-3}$ at 3,000 K and 4,000 K. For each set of initial conditions 70 target H_2 molecules were randomly selected from seven different simulations run for that set of initial conditions. Therefore, a large region of the phase space was covered. We monitored atom-atom distances of each target H_2 molecule and all O_2 molecules over the first 50 ps of the simulations. For a target H_2 molecule, a bimolecular collision $\text{O}_2\cdots\text{H}_2$ was reported when the $\text{O}\cdots\text{H}$ atom-atom distance between the target H_2 and only one O_2 molecule became less than the cutoff value of $r_{\text{O}_i\text{H}_j} \leq 1.8 \text{ \AA}$. If $\text{O}\cdots\text{H}$ atom-atom distances between hydrogen atoms of a target molecule and two oxygen molecules met this criterion, we considered a termolecular $\text{O}_2\cdots\text{H}_2\cdots\text{O}_2$ collision. For each collision, collision duration was computed as the time interval during which the criterion $r_{\text{O}_i\text{H}_j} \leq 1.8$ held true.

Figure 2.12 shows the average collision frequency for $\text{H}_2\cdots\text{O}_2$ (yellow curves and circle points) and $\text{O}_2\cdots\text{H}_2\cdots\text{O}_2$ (purple curves and square points) collisions at 3,000 K (dashed curves and blue points) and 4,000 K (solid curves and green points) as functions of density. The density change was effected by changing the volume of the simulation box at composition ratio of $[\text{H}_2]/[\text{O}_2] = 0.25$. The results in Figure 2.12 show that at both temperatures the termolecular collision $\text{O}_2\cdots\text{H}_2\cdots\text{O}_2$ is much less probable than the bimolecular one; however, the former, with nonlinear growth is more dependent on density than the latter which shows linear growth.

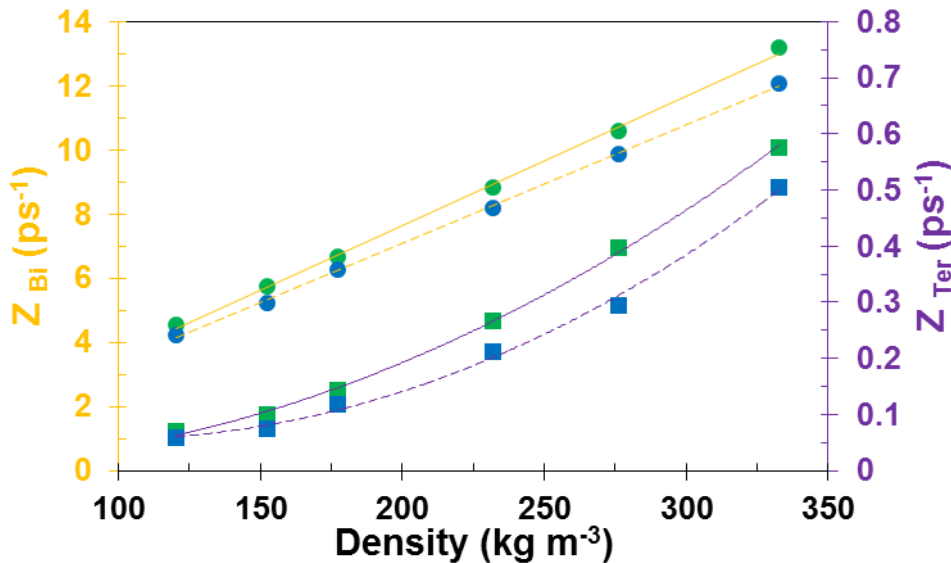


Figure 2.12: Average collision frequencies of the bimolecular $\text{O}_2\cdots\text{H}_2$ (yellow curves and circle points, left y-axis) and termolecular $\text{O}_2\cdots\text{H}_2\cdots\text{O}_2$ (purple curves and square points, right y-axis) collisions as functions of density at 3,000 K (dashed curves and blue points) and 4,000 K (solid curves and green points). The density was varied by varying the volume of the simulation box for the composition ratio $[\text{H}_2]/[\text{O}_2] = 0.25$.

To obtain an explicit expression for the density dependence of termolecular collision frequency, we made use of Bodenstein's⁹⁷ interpretation of a termolecular collision. According to Bodenstein, all termolecular collisions are indirect, that is, a transient pair [the word "transient" was not mentioned in Bodenstein's original paper] is formed before arrival of a third body species. This picture is indeed incomplete since purely triple collisions (in which all three bodies enter the collision at the same time) are not considered. In fact, termolecular collisions must be defined for the range between the indirect termolecular collisions, as defined by Bodenstein, and purely triple collisions. Here, we only consider the indirect termolecular collisions due to their relatively high importance.

Generally, binary and ternary collision frequencies are expressed as:

$$Z_{AB} = f_{AB}(T)[A][B]; \quad (2)$$

$$Z_{ABC} = f_{ABC}(T)[A][B][C], \quad (3)$$

where f 's account for temperature dependences. The frequency of triple collisions between species A, B, and C can be interpreted as the frequency of binary collisions between species A and pairs BC multiplied by concentrations of A species and BC pairs [Bodenstein, however, expressed the rate of ternary collisions slightly differently as the product of the rate of binary collisions between A and B, and the ratio of the concentration of BC pairs and free B species], that is,

$$Z_{ABC} = Z_{A,BC}[A][BC], \quad (4)$$

where concentration of BC pairs can be expressed in terms of concentrations of B and C given an equilibrium constant K_{BC} as

$$[BC] = K_{BC}[B][C]. \quad (5)$$

Substituting appropriate form of Eq. (2) for $Z_{A,BC}$ together with Eq. (5) for [BC] into Eq. (4) yields

$$Z_{ABC} = f_{A,BC}(T)K_{BC}[A][B][C]. \quad (6)$$

Comparing right-hand sides of Eqs. (3) and (6), we have

$$f_{ABC}(T) = f_{A,BC}(T)K_{BC}. \quad (7)$$

Determination of the equilibrium constant K_{BC} relies on accurately describing the forces between species B and C which is not always straightforward (at least in Bodenstein's time). Therefore, Bodenstein picked up an alternative approach that can be usefully applied today. He reasonably estimated that the ratio between the concentrations of BC pairs and free B species as the ratio of average collision duration τ_{BC} and mean free time t for B's between their collisions with C, that is,

$$\frac{[BC]}{[B]} = \frac{\tau_{BC}}{t}. \quad (8)$$

According to collision theory of gases, mean free time t is related to kinetic radius of BC pairs r_{BC} , average relative velocity \bar{v} , and the concentration of C by

$$t = \frac{1}{\pi r_{BC}^2 \bar{v} [C]}. \quad (9)$$

Substituting Eq. (9) for t in Eq. (8) and multiplying both side by $[B]$, we have

$$[BC] = \pi r_{BC}^2 \bar{v} \tau_{BC} [C][B], \quad (10)$$

so we find, comparing with Eq. (5),

$$K_{BC} = \pi r_{BC}^2 \bar{v} \tau_{BC} = f_{BC}(T) \tau_{BC}, \quad (11)$$

where the equilibrium constant K_{BC} depends on temperature *via* the dependence of the average relative velocity on temperature.

Despite the integrity of the approach proposed by Bodenstein,⁹⁷ he could not correctly estimate the average duration time appeared in Eqs. (8)–(11). He assumed that τ_{BC} is equal to the time needed for species B and C to physically impact when their initial relative distance and relative velocity are r_{BC} and \bar{v} , respectively. There are two main downsides to this assumption: (1) it takes no effect for repulsive forces which prevent two species entirely passing through the region $r < r_{BC}$; and (2) the relative velocity is not constant within this region but affected by repulsive forces.

Later, Tolman⁹⁸ suggested that it is impossible for species B and C to penetrate into the region of $r < r_{BC}$. He introduced a new length δr which is essentially smaller than r_{BC} and defined the average collision duration as the time two species spend in the region of $r_{BC} < r < r_{BC} + \delta r$ assuming the relative velocity is constant. However, introducing an unknown length δr adds further ambiguity to the problem rather than solving it.

Effects of molecular forces on determination of the equilibrium constant K_{BC} (and the collision duration τ_{BC}) for BC pairs were first studied by Kassel.⁹⁹ He reasonably assumed that repulsive forces cannot bring about ternary collisions, so that must not be considered for frequency calculations. This is mainly due to the fact that repulsive forces tend to shorten the collision duration. Therefore, it is less likely to find collisions where all three species interact concurrently when repulsive forces are dominant. As a consequence, under the influence of repulsive forces sequences of bimolecular collisions are predominant. Therefore, Kassel only accounted for attractive collisions to calculate the termolecular collision frequency between species A, B, and C.

The term “pair” is usually referred to two species whose separation distance is less than a cutoff value. This definition of a pair is in a complete agreement with the definition of a bimolecular cluster introduced earlier in this Chapter. Unlike repulsive forces, attractive forces tend to increase the time colliding pairs remain together. Depending on the total energy, there are three types of pairs that can be formed under the influence of attractive forces; permanently bound molecules, metastably bound molecules, and transient pairs. Figure 2.13 shows the conditions required for each type of the pairs to be formed. Kassel named the two former pairs as permanently stable pairs believing that these pairs are effective in producing ternary collisions.

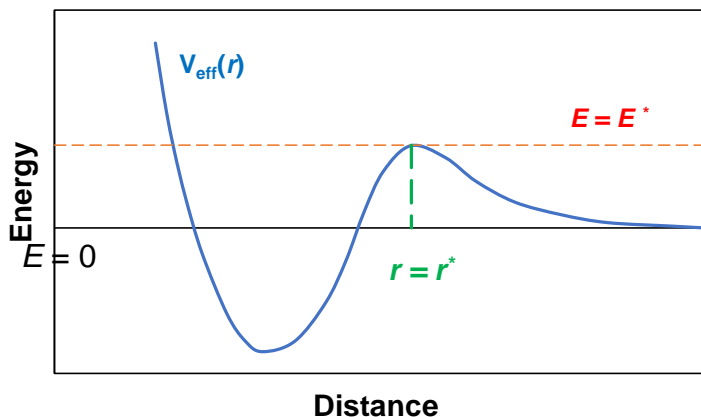


Figure 2.13: A schematic illustration of effective pair potential. Pairs with $E < 0$ form permanently bound molecules. Pairs with $0 < E < E^*$ and $r < r^*$ are referred to as metastably bound molecules trapped inside the centrifugal barrier. Pairs with $E \simeq E^*$ and $r \simeq r^*$ can dance around each other for a long time since the attractive part of the potential and the centrifugal repulsion part are balanced. These pairs are called transient pairs and are very effective in producing termolecular collisions.

Calculating the number of permanently stable pairs for a mixture of constant concentration, Kassel⁹⁹ showed that the ternary collision frequency decreases with increasing temperature due to the reduction in number of permanently stable pairs. Kassel also proved that if concentration of one species becomes relatively high (that is either lean or rich mixtures) comparing to other species, the number of permanently stable pairs falls down significantly, and thus smaller number of termolecular collisions occurs.

Kassel suggested that transient pairs might become important to compute the frequency of triple collisions only at high temperatures; however, he could not express this in a systematic way. Apparently Kassel overlooked the fact that attribute of collision duration to permanently stable pairs is meaningless. Since these pairs are referred to as

stable complexes, the term “lifetime” is more appropriate. Therefore, while there are some mechanisms of termolecular reactions initiated by the permanently stable pairs, it is the transient pairs that should be used in Bodenstein formalism to calculate the ternary collision frequency. In other words, the termolecular collision frequency is expected to increase with temperature due to the increase with temperature of the number of transient pairs. This is in contradiction with what Kassel proposed, but can justify the results shown in Figure 2.12. Seemingly, the importance of transient pairs was obvious to Smith,¹⁰⁰ who disregarded the permanently stable pairs from his discussion of termolecular collisions.

Since given three species A, B, and C, there are three possible transient pairs AB, AC, and BC, there are three contributions to the termolecular collision frequency. Therefore, a more general expression than Eq. (6) for the termolecular collision frequency is

$$Z_{ABC} = (f_{A,BC}(T)f_{BC}(T)\tau_{BC} + f_{B,AC}(T)f_{AC}(T)\tau_{AC} + f_{C,AB}(T)f_{AB}(T)\tau_{AB})[A][B][C] \quad (12)$$

where we substituted appropriate forms of Eq. (11) for the equilibrium constants K_{BC} , K_{AC} , and K_{AB} . Equating the right-hand sides of Eqs. (3) and (12), we have

$$f_{ABC} = f_{A,BC}(T)f_{BC}(T)\tau_{BC} + f_{B,AC}(T)f_{AC}(T)\tau_{AC} + f_{C,AB}(T)f_{AB}(T)\tau_{AB} \quad (13)$$

If we assume the hard sphere model for temperature dependences of binary collisions, that is,

$$f_{AB}(T) = \sqrt{\left(\frac{8\pi\kappa T}{\mu_2}\right)} (r_A + r_B)^2 \quad (14)$$

then Eq. (13) can be rewritten as

$$f_{ABC}(T) = \left(\frac{8\pi\kappa T}{\mu_3}\right) \left[(r_B + r_C)^2 (r_{BC} + r_A)^2 \tau_{BC} + (r_A + r_C)^2 (r_{AC} + r_B)^2 \tau_{AC} + (r_A + r_B)^2 (r_{AB} + r_C)^2 \tau_{AB} \right] \quad (15)$$

where τ 's are the collision durations corresponding to A \cdots B, A \cdots C, and C \cdots B collisions, and r 's are the kinetic radii, and μ_2 and μ_3 are the bi- and ter-molecular reduced masses, respectively. Substituting Eqs. (14) and (15) into Eqs. (2) and (3), respectively, for the ratio of termolecular to bimolecular collision frequencies, we have

$$\frac{Z_{ABC}}{Z_{AB}} = \frac{\sqrt{8\pi\kappa T \mu_2}}{\mu_3} \frac{(r_B + r_C)^2 (r_{BC} + r_A)^2 \tau_{BC} + (r_A + r_C)^2 (r_{AC} + r_B)^2 \tau_{AC} + (r_A + r_B)^2 (r_{AB} + r_C)^2 \tau_{AB}}{(r_A + r_B)^2} [C] \quad (16)$$

In our study, species A and C are oxygen molecules and B is the hydrogen molecule. Equation (16) shows that the ratio of termolecular collision frequency to the bimolecular collision frequency is linear with respect to density (or [C]) if and only if the collision durations of τ are independent of density. We determined the collision durations τ for O₂ \cdots O₂ and O₂ \cdots H₂ transient pairs to be used in Eq. (16). To get the collision duration for O₂ \cdots O₂ transient pairs, τ_{AC} , at each density input in the interval of 120-350 kg·m⁻³, 70 oxygen molecules equally distributed in seven different simulations were tracked for 50 ps. Whenever a target oxygen molecule was within the interatomic cutoff distance of 3.5 Å of only one oxygen molecule, we considered a transient pair of O₂ \cdots O₂. We excluded

the cases where a hydrogen molecule or more than one oxygen molecule were interacting with the target oxygen molecules. Similarly, to get the collision duration for $O_2 \cdots H_2$ transient pairs, $\tau_{AB} = \tau_{BC}$, at each density input in the interval of $120\text{-}350 \text{ kg}\cdot\text{m}^{-3}$, 70 hydrogen molecules equally distributed in seven different simulations were tracked for 50 ps. Whenever a target hydrogen molecule was within the interatomic cutoff distance of 1.8 \AA of only one oxygen molecule, we considered a transient pair of $O_2 \cdots H_2$. We excluded the cases where another hydrogen molecule or more than one oxygen molecule were present. This procedure determines the transient pairs of $O_2 \cdots O_2$ and $O_2 \cdots H_2$, respectively. The duration of a collision for a transient pair was measured as the length of the time they were interacting within the cutoff distance and were not interrupted by a third molecule. Figure 2.14 shows that at $T = 3,000 \text{ K}$ (dashed curves and blue points) and $4,000 \text{ K}$ (solid curves and green points) the average collision duration for $O_2 \cdots O_2$ transient pairs (yellow curves and circle points) linearly decreases with density. The similar trend was observed for $O_2 \cdots H_2$ pairs (purple curves and square points). Finally, the linear dependence of collision durations to density shown in Figure 2.14 can be substituted into Eq. (16) to get the ratio of termolecular to bimolecular collision frequencies. It is straightforward to show that the collision frequency ratio of Eq. (16) is non-linearly dependent on density resulting from multiplying linear term for collision durations and a linear term for the explicit dependency on density ($[C]$). This ratio is plotted for the simulations in Figure 2.15.

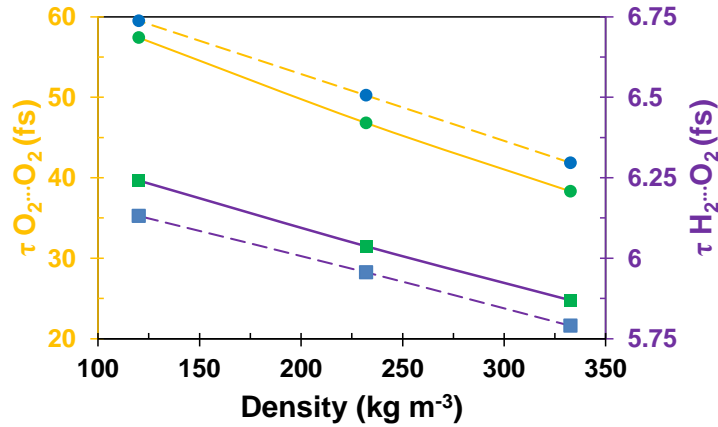


Figure 2.14: Average durations of the $O_2 \cdots O_2$ (yellow curves and circle points, left y-axis) and $O_2 \cdots H_2$ (purple curves and square points, right y-axis) collisions as functions of density at 3,000 K (dashed curves and blue points) and 4,000 K (solid curves and green points). The density was varied by varying the volume of the simulation box with $[H_2]/[O_2] = 0.25$.

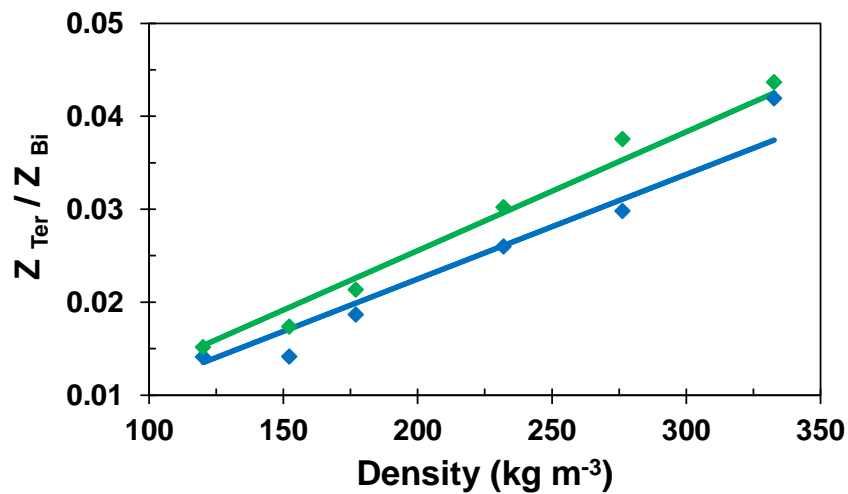


Figure 2.15: The ratios of the termolecular collision frequency to the bimolecular collision frequency computed using Eq. (16) at 3,000 K (blue) and 4,000 K (green).

As Figure 2.14 predicts, while the average collision duration of O₂··O₂ transient pairs decreases with temperature, the average collision duration of O₂··H₂ transient pairs increases with temperature. However, the opposite effects of temperature on the average collision duration of O₂··O₂ transient pairs and O₂··H₂ transient pairs, seemingly, cancel each other out. To verify this, we defined the characteristic ratio of termolecular to bimolecular collision frequencies, $\left(\frac{Z_{ABC}}{Z_{AB}}\right)^*$, by dividing both sides of Eq. (16) by \sqrt{T} ; that is,

$$\left(\frac{Z_{ABC}}{Z_{AB}}\right)^* = \frac{\sqrt{8\pi\kappa\mu_2} (r_B + r_C)^2 (r_{BC} + r_A)^2 \tau_{BC} + (r_A + r_C)^2 (r_{AC} + r_B)^2 \tau_{AC} + (r_A + r_B)^2 (r_{AB} + r_C)^2 \tau_{AB}}{\mu_3 (r_A + r_B)^2} [C] \quad (17)$$

The characteristic ratio of termolecular to bimolecular collision frequencies, as expressed in Eq. (17), is plotted in Figure 2.16 for T = 3,000 K (blue) and 4,000 K (green), for the density interval 120.2 kg·m⁻³ to 332.7 kg·m⁻³ and composition ratio of [H₂]/[O₂] = 0.25. Figure 2.16 proves that for the termolecular and bimolecular collisions of this study, the characteristic ratio of $\left(\frac{Z_{ABC}}{Z_{AB}}\right)^*$ depends only on density (and not on temperature). This confirms the fact that the favorable effects of temperature on the average collision duration of O₂--H₂ transient pairs, are canceled by its negative effect on the average collision duration of O₂--O₂ transient pairs. Therefore, the ratio $\left(\frac{Z_{ABC}}{Z_{AB}}\right)$ increases by temperature only through a factor of \sqrt{T} .

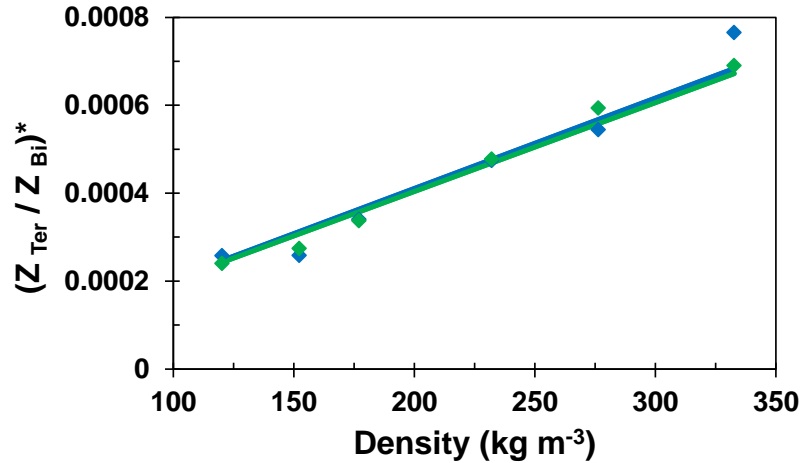


Figure 2.16: The characteristic ratio of the termolecular collision frequency to the bimolecular collision frequency computed using Eq. (17) at 3,000 K (blue) and 4,000 K (green). The characteristic ratio is independent of temperature.

At both temperatures, while the collision frequency of bimolecular collisions $O_2 \cdots H_2$ is multiplied by 2.10 when density increases from $120.2 \text{ kg}\cdot\text{m}^{-3}$ to $332.7 \text{ kg}\cdot\text{m}^{-3}$, that for termolecular collisions $O_2 \cdots H_2 \cdots O_2$ is multiplied by 8.5 (See Figure 2.12). The significant increase in the collision frequency of termolecular collisions in the density range of $120.2 \text{ kg}\cdot\text{m}^{-3}$ to $332.7 \text{ kg}\cdot\text{m}^{-3}$ (in form of a third degree polynomial function) suggests that the reaction $2O_2 + H_2 \rightarrow 2HO_2$ becomes relatively more important than the reaction $O_2 + H_2 \rightarrow H + HO_2$ with increasing density (and pressure). It must be noted that since the termolecular collision frequency is smaller than the bimolecular collision frequency by almost 30 factors (see Figure 2.12), bimolecular reaction $O_2 + H_2 \rightarrow H + HO_2$ plays a more important role on the initiation mechanism than the termolecular reaction $2O_2 + H_2 \rightarrow 2HO_2$ at almost any of the density regimes considered (except at densities greater than $250 \text{ kg}\cdot\text{m}^{-3}$ at 3,000 K) which justifies the trend observed in panels of Figure 2.11.

3. POTENTIAL ENERGY PROFILE AND ENERGY REQUIREMENT²

The ReaxFF simulations predict that the termolecular initial reactions $2\text{O}_2 + \text{H}_2 \rightarrow 2\text{HO}_2$ and $2\text{O}_2 + \text{H}_2 \rightarrow \text{H} + \text{HO}_2 + \text{O}_2$ may play roles in the initial radical formation at sufficiently high pressures; however, the energy requirements of these reactions are important in determining their roles. In this Chapter we intend to characterize the energetics of the termolecular reaction $2\text{O}_2 + \text{H}_2 \rightarrow 2\text{HO}_2$ and bimolecular reaction $\text{O}_2 + \text{H}_2 \rightarrow \text{H} + \text{HO}_2$. Using accurate *ab initio* forces, we found the barrier heights for both reactions and could characterize the stationary points on the potential energy surface of each reaction. We also calculated the barrier height predicted by ReaxFF for each reaction and compared it to the one computed by the electronic structure theory. Characterization and comparison of both reactions from the energy point of view is essential to better understand the competition between the two reactions.

3.1 COMPUTATIONAL METHODS

3.1.1 NUDGED ELASTIC BAND METHOD

Nudged Elastic Band (NEB)¹⁰¹⁻¹⁰³ method is a common approach to find the minimum energy path (MEP) connecting two stable configurations of cluster of atoms, that is, two local minima such as configuration of reactants and configuration of products. The NEB method is in essence a form of chain-of-states method¹⁰⁴⁻¹⁰⁷ in which a path is

² Parts of this Chapter were published as M. Monge-Palacios and H. Rafatijo, On the Role of the Termolecular Reactions $2\text{O}_2 + \text{H}_2 \rightarrow 2\text{HO}_2$ and $2\text{O}_2 + \text{H}_2 \rightarrow \text{H} + \text{HO}_2 + \text{O}_2$ in Formation of the First Radicals in Hydrogen Combustion: *ab initio* Predictions of Energy Barriers, *Phys. Chem. Chem. Phys.* **19**, 2175 (2017).

assumed as a chain of several images (or ‘replicas’) of the system that are connected through zero-length springs. The images are selected along the reaction coordinate beginning with configuration of reactants and ending with configuration of products. In chain-of-states methods, the goal is to find the MEP *via* optimization of an energy objective function which represents the energy pathway. A typical form of the objective function can be expressed as

$$S(\mathbf{R}_0, \mathbf{R}_1, \dots, \mathbf{R}_n) = \sum_{i=0}^n V(\mathbf{R}_i) + \sum_{i=0}^n \frac{1}{2} k (\mathbf{R}_i - \mathbf{R}_{i-1})^2, \quad (1)$$

where \mathbf{R}_i stands for state of the i^{th} replica and $V(\mathbf{R}_i)$ is the potential energy of the i^{th} replica. There are total of $(n + 1)$ replicas and k is the spring constant. The force on the i^{th} replica then is

$$\mathbf{F}_i = \frac{-\partial V(\mathbf{R}_i)}{\partial \mathbf{R}_i} - k (2\mathbf{R}_i - \mathbf{R}_{i-1} - \mathbf{R}_{i+1}), \quad (2)$$

where the term with k is the net spring force and the other term is the configurational force defined as the gradient of the potential energy of the i^{th} replica.

In the NEB method, optimization of the objective function of Eq. (1) is carried out where the component of configurational force parallel to the energy pathway and the component of net spring force perpendicular to the energy pathway are projected out from Eq. (2). The reason to neglect the former force term is that it causes non-uniformity in distribution of replicas along the reaction pathway, and the removal of the latter term

avoids a drift of the energy pathway which causes to miss the saddle point region in characterizing MEP.

In this study, a version of the NEB method¹⁰⁸ as implemented in LAMMPS 2014 was used to identify the MEPs and optimize the saddle points predicted by ReaxFF for the termolecular reaction $2\text{O}_2 + \text{H}_2 \rightarrow 2\text{HO}_2$ and bimolecular reaction $\text{O}_2 + \text{H}_2 \rightarrow \text{H} + \text{HO}_2$. A minimum total number of 36 replicas initially distributed equidistantly along the reaction pathway were selected from actual simulations to perform the NEB study. The value of the force constants was iteratively changed within the $1.0 \times 10^{-5} E_h \cdot a_0^{-2}$ to $1.0 \times 10^{-1} E_h \cdot a_0^{-2}$ interval until the force criteria of $1.0 \times 10^{-5} E_h \cdot a_0$ was met for the saddle points.

3.1.2 ELECTRONIC STRUCTURE CALCULATIONS

Electronic structure calculations were performed using the Gaussian09 package¹⁰⁹ to optimize and characterize critical points on the potential energy surfaces of the initial reactions that were observed in CMD simulations of hydrogen combustion. The CCSD(T)=FULL/aug-cc-pVTZ//CCSD=FC/cc-pVTZ single-point *ab initio* level was used, based on the CCSD=FC and CCSD(T)=FULL coupled cluster methods^{110,111} and the cc-pVTZ and aug-cc-pVTZ basis sets.^{112,113} The lower CCSD(T)=FC/cc-pVTZ//MP2/6-31G single-point level was also used, based on the second order Moller-Plesset perturbational method MP2¹¹⁴ and the 6-31G basis set.¹¹⁵ In addition, the energies obtained at these two levels of theory were corrected by considering the basis set superposition error, calculated with the Boys and Bernardi counterpoise correction.¹¹⁶

The spin contamination in the wave-functions was checked by analyzing the $\langle S^2 \rangle$ expectation value, verifying that it is negligible³ in the found stationary points. Another important aspect is the multi-reference character of the stationary points. This feature was addressed with the *TI* diagnostic by Lee and Taylor¹¹⁷ and was checked to ensure that the coupled cluster methods are suitable for studying the found stationary points. We also performed CASSCF calculations including dynamic correlation, CASSCF MP2, as implemented in Gaussian09 to further validate the single-reference methods used in our calculations.

3.2 OXYGEN DIMER

In the previous Chapter, we showed that one possible pathway for the termolecular reaction $2\text{O}_2 + \text{H}_2 \rightarrow 2\text{HO}_2$ is a reactive collision between a hydrogen molecule and an $\text{O}_2\text{-O}_2$ dimer. Therefore, understanding the $\text{O}_2\text{-O}_2$ dimer potential energy surface is essential to perform any electronic structure calculations.

Accurately characterizing interaction of two ground state oxygen molecules, $\text{O}_2(^3\Sigma_g^-)$ is a difficult problem that has been target of many theoretical works.⁷⁴⁻⁷⁹ This difficulty is raised from the spin exchange interaction between two $\text{O}_2(^3\Sigma_g^-)$ molecules which leads to three different PESs: singlet, triplet and quintet. Such spin exchange interaction can be represented in form of a Heisenberg-Dirac Hamiltonian as

$$\hat{H}_{\text{EX}} = -2J \hat{\mathbf{S}}_{\text{A}} \cdot \hat{\mathbf{S}}_{\text{B}}, \quad (3)$$

³ Further studies are underway which indicate that the saddle points reported for the termolecular reactions are highly spin contaminated.

where J is the spin coupling constant between molecules A and B. The spin coupling constant, J , generally depends on both intermolecular distance of two oxygen molecules and their relative orientation.⁷⁹ It has been proved that the most accurate *ab initio* methods such as CCSD(T) can be applied only for the quintet electronic state of $O_2(^3\Sigma_g^-)$ - $O_2(^3\Sigma_g^-)$ dimer. The reason for this limitation is the fact that single-reference CCSD(T) methods do not account for systems with strong static correlations such as spin exchange interaction.^{118,119} In contrast to the quintet state, characterization and description of the lower triplet and singlet states inevitably require multi-reference configuration interaction methods, MRCI.¹²⁰ Gadzhiev *et al.*¹²⁰ showed that CCSD(T) methods reproduce an excited triplet(singlet) electronic state for the $mS = 1(0)$ of the dimer in which there is(are) one(two) singlet oxygen molecule(s), $O_2(^1\Delta_g)$. According to Gadzhiev *et al.* the schematic representations of the molecular orbitals for the quintet, triplet, and singlet electronic states of the O_2 - O_2 dimer as predicted by CCSD(T) are illustrated in Figure 3.1.

In a recent study, Bartolomei *et al.*⁷⁷ reported global *ab initio* PESs of three multiplet spin states for two interacting rigid $O_2(^3\Sigma_g^-)$ molecules. Hernández-Lamonedá *et al.*⁷⁶ showed that the energy splitting between these three spin states dies out for interatomic distances larger than 4.0 Å. As two interacting open-shell $O_2(^3\Sigma_g^-)$ molecules split into three different PESs, three possible scenarios may arise for the termolecular cluster of $2O_2(^3\Sigma_g^-) + H_2$: singlet, triplet, and quintet states. With regard to the reactions $2O_2(^3\Sigma_g^-) + H_2 \rightarrow 2HO_2$ and $2O_2(^3\Sigma_g^-) + H_2 \rightarrow H + HO_2 + O_2$, the quintet state cannot be involved because the interacting products cannot generate a quintet state. In the synchronous pathway, for instance, the quintet state cannot correlate with two doublet HO_2 radicals.

Since the methods used to study these reactions were single-reference CCSD(T), we, unfortunately, could not confidently claim that the lowest triplet and the lowest singlet electronic states for these reactions were studied. Although suitability of the single-reference CCSD(T) methods used in this study was checked by analyzing the *TI* diagnostic as well as performing CASSCF MP2 calculations, we present our results with caution since it is possible that single-reference CCSD(T) methods may not be useful to study the lowest triplet and the lowest singlet electronic states for these reactions as cautioned by Gadzhiev *et al.*¹²⁰

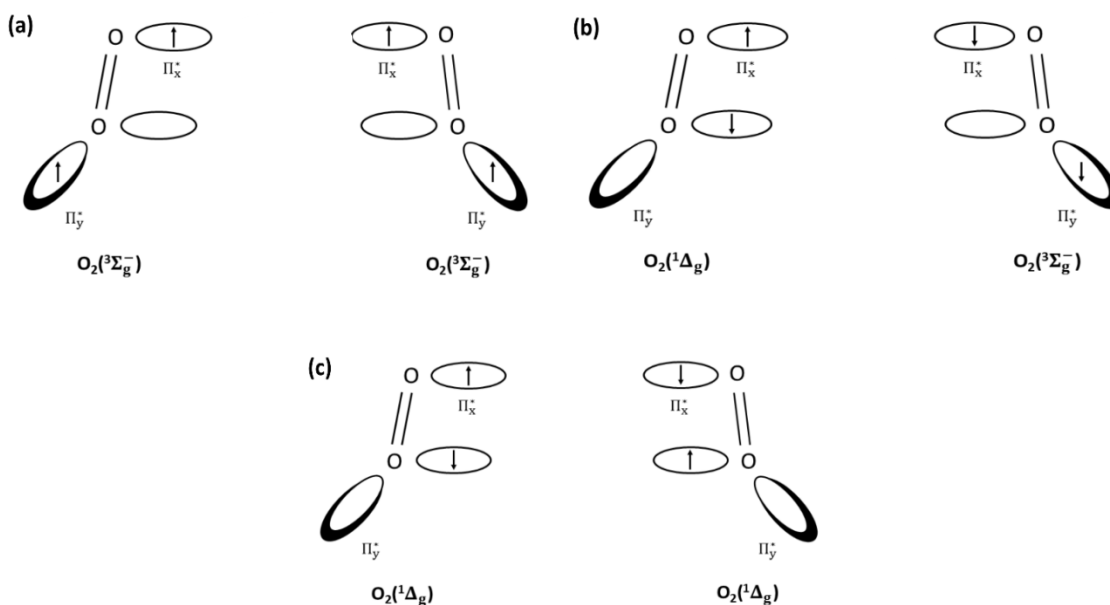


Figure 3.1: Schematic representations of the molecular orbitals for the O₂-O₂ dimer according to CCSD(T) calculations performed by Gadzhiev *et al.*: (a) quintet state; (b) triplet state; (c) singlet state. They postulated that for exploring the triplet and singlet PESs raised from two ground-state oxygen molecules, 2O₂(³Σ_g⁻), CCSD(T) methods may not be useful.

3.3 RESULTS AND DISCUSSION

3.3.1 NEB RESULTS FOR ReaxFF FORCE FIELD

The potential energy profile and geometry of the stationary points predicted by ReaxFF for the bimolecular reaction $\text{O}_2 + \text{H}_2 \rightarrow \text{H} + \text{HO}_2$ and the termolecular reaction $2\text{O}_2 + \text{H}_2 \rightarrow 2\text{HO}_2$ are shown in Figure 3.2, respectively, and the corresponding geometrical parameters are provided in Table 3.1. As inferred from Figure 3.2, the termolecular reaction $2\text{O}_2 + \text{H}_2 \rightarrow 2\text{HO}_2$ through the synchronous pathway is energetically more favorable than the bimolecular reaction $\text{O}_2 + \text{H}_2 \rightarrow \text{H} + \text{HO}_2$. It is important to note that the ReaxFF prediction for the barrier height of the bimolecular reaction is only 0.17 kcal/mol lower than the value reported by Michael *et al.*⁵² using the accurate CCSD(T)=FC/cc-pVQZ level of theory. This proves that ReaxFF performance is really good regarding to the bimolecular reaction which is not far from our expectation since the bimolecular reaction $\text{O}_2 + \text{H}_2 \rightarrow \text{H} + \text{HO}_2$ is one of the reactions listed in Li *et al.*³⁴ mechanism, and thus used to obtain the QM training data set for development of ReaxFF force field for hydrogen combustion.⁶⁴

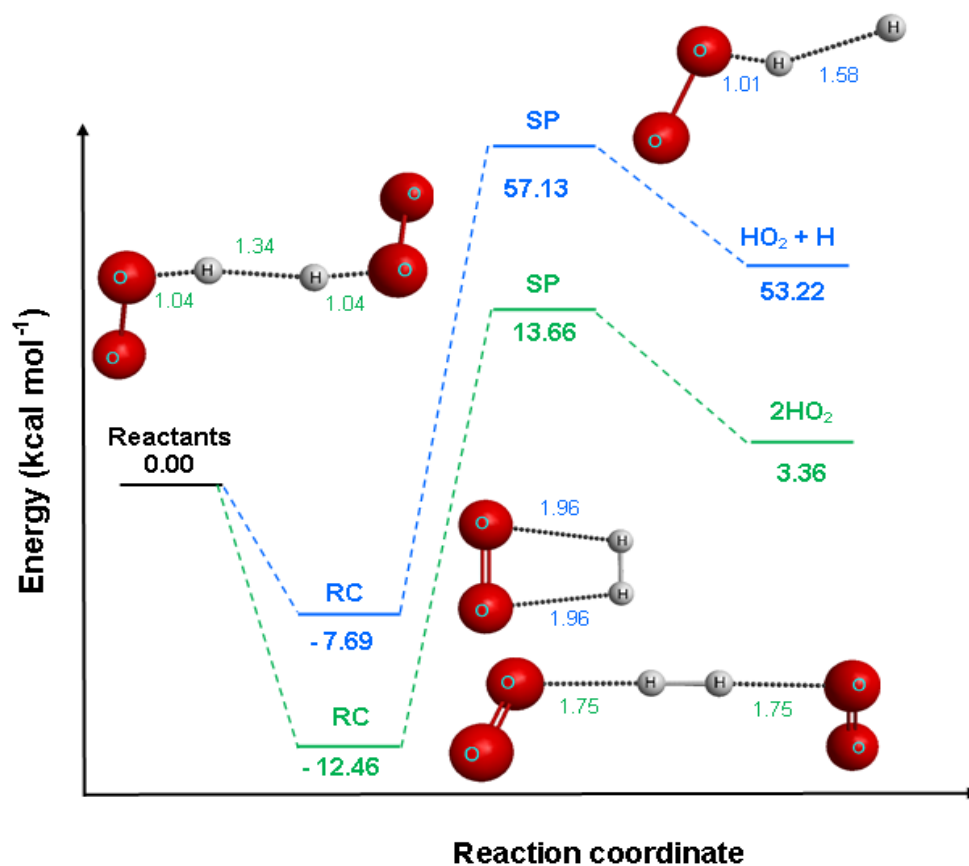


Figure 3.2: ReaxFF potential energy profile obtained *via* NEB method with the energy (kcal/mol), with respect to the reactants of the termolecular $2\text{O}_2 + \text{H}_2 \rightarrow 2\text{HO}_2$ (green lines) and bimolecular $\text{H}_2 + \text{O}_2 \rightarrow \text{H} + \text{HO}_2$ (blue lines) reactions. Optimized geometry of the stationary points including the reactant complexes (RC) and the saddle points (SP) predicted by ReaxFF are included, as well. (Distances in angstroms)

Table 3.1: The ReaxFF predictions for the geometrical parameters of the stationary points of the potential energy surface for the ter- and bi-molecular reactions obtained by the NEB method.^a

| | SP | RC |
|---------------------|---------|--------|
| Termolecular | | |
| r O'-H' | 1.04 | 1.75 |
| r O-H | 1.04 | 1.75 |
| r H-H' | 1.34 | 0.88 |
| α O-H-H'-O' | -170.49 | 156.46 |
| Bimolecular | | |
| r O-H | 1.01 | 1.96 |
| r H-H' | 1.58 | 0.81 |
| α O-H-H' | 146.59 | 95.60 |
| β O'-O-H-H' | -136.86 | 180.00 |

^a Distances in angstroms, and angles in degrees.

3.3.2 AB INITIO RESULTS

We began by exploring the triplet PES using *ab initio* electronic structure theory. The optimized geometries for the saddle points and complexes on the triplet PES of the termolecular reactions, including the eigenvector associated to the imaginary frequency are shown in Figure 3.3(a). The geometrical parameters, harmonic vibrational frequencies, and energies and enthalpies (relative to the reactants $2\text{O}_2(^3\Sigma_g^-) + \text{H}_2$) are given in Table 3.2. The results obtained for the bimolecular reaction $\text{H}_2 + \text{O}_2 \rightarrow \text{H} + \text{HO}_2$ are also included for comparison in Table 3.2 and Figure 3.3(b).

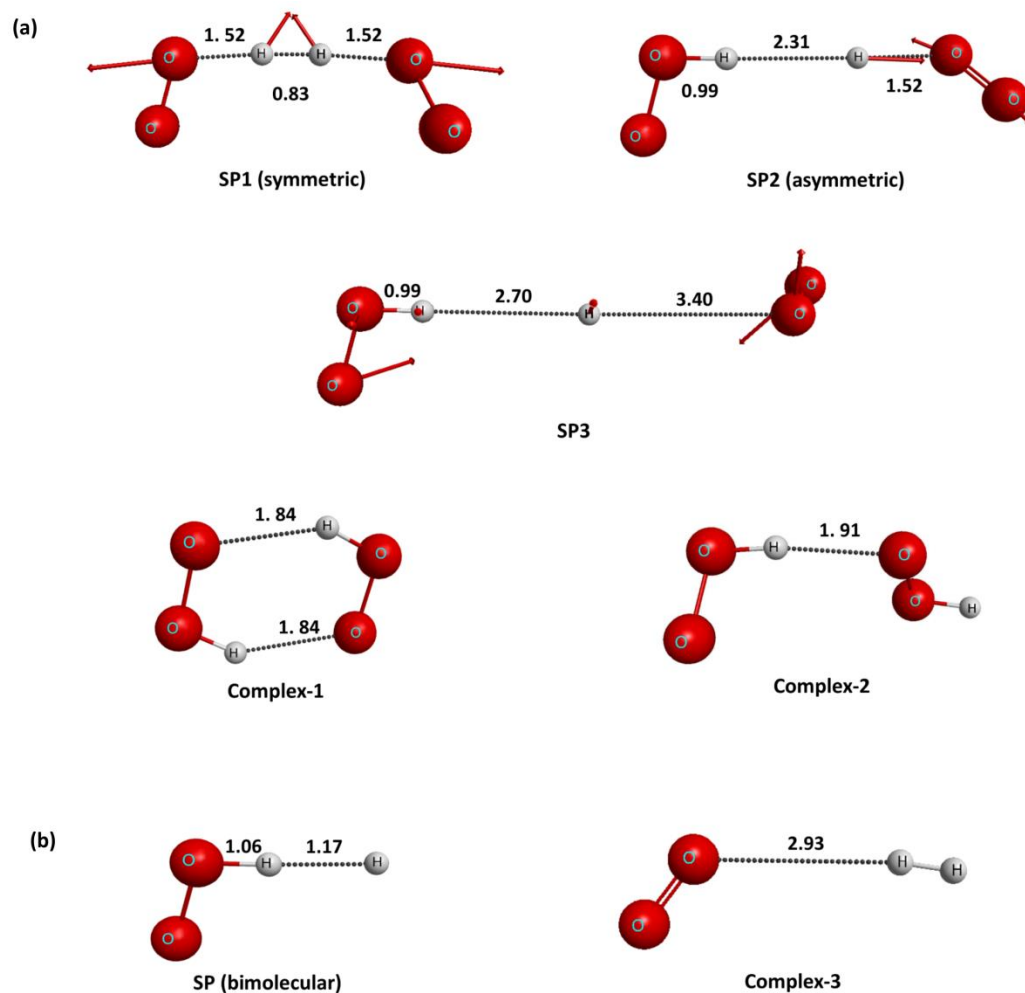


Figure 3.3: Optimized geometries (distances in angstroms) at the CCSD=FC/cc-pVTZ *ab initio* level of the saddle points and intermediate complexes on the triplet PES of the (a) termolecular and (b) bimolecular reactions, $2\text{O}_2 + \text{H}_2 \rightarrow 2\text{HO}_2$, $2\text{O}_2 + \text{H}_2 \rightarrow \text{H} + \text{HO}_2 + \text{O}_2$ and $\text{H}_2 + \text{O}_2 \rightarrow \text{H} + \text{HO}_2$ (SP2 and SP3 at the MP2/6-31G level). The eigenvectors associated to the imaginary frequencies of the saddle points of the termolecular reactions are also given

Using the CCSD(T)=FULL/aug-cc-pVTZ//CCSD=FC/cc-pVTZ *ab initio* level we found for $2\text{O}_2 + \text{H}_2 \rightarrow 2\text{HO}_2$ one saddle point, SP1, and two intermediate complexes

located in the product channel, Complex-1 and Complex-2 (see Table 2). Complex-1 is the same as the one reported by Zhou *et al.*,⁹⁵ and corresponds to the ring structure observed in the indirect pathway in the simulations using ReaxFF.

At the MP2/6-31G *ab initio* level we found two more saddle points, labeled SP2 and SP3 in Table 2. These saddle points might be saddle points for $2\text{O}_2 + \text{H}_2 \rightarrow 2\text{HO}_2$ and $2\text{O}_2 + \text{H}_2 \rightarrow \text{H} + \text{HO}_2 + \text{O}_2$, respectively. However, our attempts at optimization for these saddle points failed at the CCSD = FC/cc-pVTZ level, so they should be considered with caution as candidate but unverified saddle points of the studied termolecular reactions. The energies were refined using the CCSD(T) = FC/cc-pVTZ//MP2/6-31G single point *ab initio* level.

The symmetric saddle point SP1 is characterized by an imaginary frequency associated with an eigenvector located on the two new O–H bonds (see SP1 in Figure 3.3(a)). The asymmetric saddle point SP2 presents a larger difference between the O–H bond distances, with the eigenvector associated with the imaginary frequency located almost exclusively on the last-formed O–H bond (see SP2 in Figure 3.3(a)). The saddle point SP3, also on the triplet PES, has more asymmetric character than the saddle point SP2, with one O–H bond formed but with the other O₂ molecule largely separated from the remaining hydrogen atom (see SP3 in Figure 3.3(a)). It is characterized by a very low imaginary frequency, mainly associated with a torsional motion, and indicating that this saddle point may be closely linked to the $\text{H} + \text{HO}_2 + \text{O}_2$ product channel.

Table 3.2: *Ab initio* calculated geometries, vibrational frequencies, saddle point and complex energies relative to reactants, ΔV , enthalpy changes, ΔH (0 K), and absolute energies.^a

| | Geometry | Frequencies | ΔV | ΔH (0 K) | Absolute energy | |
|--|------------------------------|-------------|---|------------------|-----------------|-------------|
| SP1 (symmetric, C₁) | | | | | | |
| | r O–H | 1.52 | 2216, 1458, 1296, | 49.8 | 52.1 | -301.4314 |
| | r O–H | 1.52 | 1135, 1013, 967, | (44.9) | (47.6) | (-301.3245) |
| | r H–H' | 0.83 | 672, 377, 136, | | | |
| | α O–O–H–H' | -4.69 | 50, 16, 621i | | | |
| SP2 (asymmetric, C₁) | | | | | | |
| | r O–H | 0.99 | 3498, 1537, 1435, 1361, | (53.1) | (56.8) | (-301.3115) |
| | r O–H' | 1.52 | 771, 151, 99, 57, | | | |
| | r H–H' | 2.31 | 40, 20, 9, 2096i | | | |
| SP3 (C₁) | | | | | | |
| | r O–H | 0.99 | 3511, 1431, 1359, 942, | (48.1) | (49.7) | (-301.3195) |
| | r O–H' | 3.40 | 118, 75, 26, 20, | | | |
| | r H–H' | 2.70 | 16, 6, 4, 5i | | | |
| Complex-1 (C₁) | | | | | | |
| | r O \cdots H ^b | 1.84 | 3546, 3475, 1593, 1568, | -10.9 | -1.0 | -301.5283 |
| | r O \cdots H' ^b | 1.84 | 1210, 1203, 707, 561, | | | |
| | α O–O–H–O | 0.05 | 278, 255, 205, 106 | | | |
| Complex-2 (C₁) | | | | | | |
| | r O \cdots H ^b | 1.91 | 3716, 3649, 1542, 1475, 1190, 1186, 535, 265, 191, 96, 53, 23 | -5.2 | 3.6 | -301.5191 |
| SP (C₁) | | | | | | |
| | r O–H | 1.06 | 1650, 1413, 1224, | 58.9 | 57.9 | -151.2479 |
| | r H–H' | 1.17 | 723, 357, 2077i | (49.8) | (49.5) | (-151.2049) |
| | α O–H–H' | 178.6 | | | | |
| | β O–O–H–H' | 180.0 | | | | |
| Complex-3 (C₁) | | | | | | |
| | r(O \cdots H) ^b | 2.93 | 4410, 1666, 136, | -0.1 | 0.3 | -151.3420 |
| | α (O–H–H') | 171.5 | 133, 82, 2 | | | |
| | β (O–O–H–H') | 23.3 | | | | |

^a Distances in angstroms, frequencies in cm⁻¹, and relative energies and enthalpies in kcal/mol. The absolute energy is given in atomic units. All computed at the CCSD(T)=FULL/aug-cc-pVTZ//CCSD=FC/cc-pVTZ single point *ab initio* level except

for the SP2 and SP3 results (given in parentheses), which were calculated at the CCSD(T)=FC/cc-pVTZ//MP2/6-31G level. The basis set superposition error is considered.

^b $r(\text{O}\cdots\text{H})$ and $r(\text{O}\cdots\text{H}')$ are the hydrogen bond lengths.

We determined the saddle point SP1 at the CCSD(T)=FC/cc-pVTZ//MP2/6-31G level for comparison with SP2 and SP3, which we could not obtain at the CCSD=FC/cc-pVTZ level. The CCSD(T)=FC/cc-pVTZ//MP2/6-31G energy values are shown in parenthesis in Table 3.2. At this lower level, the classical energy barrier heights, ΔV , with respect to the reactants $2\text{O}_2(^3\Sigma_g^-) + \text{H}_2$, for the saddle points SP1, SP2, and SP3 are, respectively, 44.9 kcal/mol, 53.1 kcal/mol, and 48.1 kcal/mol. The reaction *via* SP3 is essentially a bimolecular reaction in which the second O_2 acts as a third body: $2\text{O}_2 + \text{H}_2 \rightarrow \text{H} + \text{HO}_2 + \text{O}_2$. The effect of the second (third-body) O_2 is to reduce the energy barrier to $\text{H}_2 + \text{O}_2 \rightarrow \text{H} + \text{HO}_2$ by 1.7 kcal/mol (see Table 3.2).

The intermediates Complex-1 and Complex-2 ($-10.9 \text{ kcal}\cdot\text{mol}^{-1}$ and $-5.2 \text{ kcal}\cdot\text{mol}^{-1}$ at the CCSD(T)=FULL/aug-cc-pVTZ//CCSD=FC/cc-pVTZ *ab initio* level, respectively, relative to the $2\text{O}_2(^3\Sigma_g^-) + \text{H}_2$ reactants) are formed by the two incipient HO_2 product radicals. Complex-1 is much more stable than Complex-2 because it forms two hydrogen bonds; Complex-2 is higher in energy than the reactants when the zero point energy is taken into account: $\Delta H(0 \text{ K}) = 3.6 \text{ kcal/mol}$. ReaxFF also describes this indirect pathway involving the complex $\text{HO}_2\cdots\text{HO}_2$. Our *ab initio* results and MD simulations predict that these complexes may be formed *via* $2\text{O}_2 + \text{H}_2 \rightarrow \text{SP1/SP2} \rightarrow \text{Complex-1/Complex-2} \rightarrow 2\text{HO}_2/\text{H}_2\text{O}_2 + \text{O}_2$. Although we did not observe indirect trajectories forming both

intermediate complexes, that is, Complex-1 converted into Complex-2 or *vice versa*, we cannot discard this kind of trajectory.

In the saddle points SP1, SP2 and SP3 the two $\text{O}_2(^3\Sigma_g^-)$ molecules stand at long intermolecular distances (larger than 4.0 Å); this leads us to think that the splitting due to the interaction of the $\text{O}_2(^3\Sigma_g^-)$ molecules may not be significant according to Hernández-Lamonedá *et al.*⁷⁶ In order to explore whether or not there are other feasible PESs for these termolecular reactions, a stability test of the triplet wavefunction was done with Gaussian09 on the termolecular saddle points SP1, SP2 and SP3, not finding any evidence of the singlet and quintet electronic states. In addition, the quintet state cannot be involved in the reaction $2\text{O}_2 + \text{H}_2 \rightarrow 2\text{HO}_2$ because that state cannot correlate with two doublet HO_2 radicals.

The saddle point along the $\text{H}_2 + \text{O}_2 \rightarrow \text{H} + \text{HO}_2$ reaction path, SP, on the bimolecular triplet PES is 58.9 kcal/mol with respect to $\text{H}_2 + \text{O}_2(^3\Sigma_g^-)$ at the CCSD(T)=FULL/aug-cc-pVTZ//CCSD=FC/cc-pVTZ level (see Table 3.2 and Figure 3.3(b)); 9.1 kcal/mol higher than the symmetric saddle point SP1 on the $2\text{O}_2 + \text{H}_2 \rightarrow 2\text{HO}_2$ triplet PES. To allow for a direct comparison the saddle point SP was also optimized and characterized at the CCSD(T)=FC/cc-pVTZ//MP2/6-31G level; see the values in parenthesis in Table 3.2. At this level the classical ground-state barrier heights are 44.9 kcal/mol, 48.1 kcal/mol, 49.8 kcal/mol, and 53.1 kcal/mol, respectively, for the symmetric termolecular SP1, termolecular SP3, bimolecular SP, and asymmetric termolecular SP2.

A very weakly bound complex, Complex-3 (see Table 3.2 and Figure 3.3(b)), is formed on the bimolecular triplet PES in the entrance channel: $\text{H}_2 + \text{O}_2 \rightarrow \text{Complex-3} \rightarrow \text{SP} \rightarrow \text{H} + \text{HO}_2$.

This is a weak van der Waals complex with very low vibrational frequencies corresponding to torsional modes (see Table 3.2). It is located at -0.1 kcal/mol relative to $\text{H}_2 + \text{O}_2(^3\Sigma_g^-)$. When the zero point energy is taken into account, the complex is not stable; $\Delta H(0 \text{ K}) = 0.3 \text{ kcal/mol}$.

Michael *et al.*⁵² reported values for the classical energy barrier height to $\text{H}_2 + \text{O}_2 \rightarrow \text{H} + \text{HO}_2$ using the CCSD(T)=FC *ab initio* method and the cc-pVDZ, cc-pVTZ and cc-pVQZ basis sets, obtaining values of 60.2 kcal/mol, 58.3 kcal/mol, and 57.8 kcal/mol, respectively. The result at the CCSD(T)=FC/cc-pVQZ *ab initio* level, 57.8 kcal/mol, is in good agreement with that obtained in this work at the less computationally expensive CCSD(T)=FULL/aug-cc-pVTZ//CCSD=FC/cc-pVTZ single point level, 58.9 kcal/mol (SP in Table 3.2), differing only by 1.1 kcal/mol. Michael *et al.*⁵² also calculated 55.4 kcal/mol for the enthalpy of reaction, $\Delta H_{\text{R}}(0 \text{ K})$, at the CCSD(T)=FC/cc-pVQZ level; that is, 0.6 kcal/mol higher than the value of 54.8 kcal/mol we obtained at the CCSD(T)=FULL/aug-cc-pVTZ//CCSD=FC/cc-pVTZ level. These values are in good agreement with the experimental value $55.7 \pm 0.8 \text{ kcal/mol}$ reported by Litorja *et al.*¹²¹

The connection between the localized stationary points was further investigated by performing IRC calculations using Gaussian09.¹⁰⁹ Using the optimized saddle points SP1, SP2, and SP3 as starting points, we followed these reaction paths in both directions: the reactants or forward direction, and the products or backward direction. As for the backward direction, SP1 and SP2 lead to structures involving two HO_2 radicals bonded by hydrogen bonds with $\text{O}\cdots\text{H}$ distances 2.8 Å and 2.3 Å, respectively. Although the IRCs did not directly converge to the complexes Complex-1 and Complex-2, the abovementioned structures seem to connect with Complex-1 and Complex-2 by rotating

the HO₂ fragments. In fact, we ran a further optimization of the structure reached along the backward IRC from SP2 and obtained Complex-1.

As for the forward direction, the IRC calculated for the saddle point SP1 leads to a structure formed by the 2O₂ and H₂ reactants with O···H distances about 2.5 Å. This structure seems to be consistent with a van der Waals complex; however, all the attempts to optimize it as a minimum failed, obtaining low imaginary frequencies. Thus, we could not confirm the existence of a van der Waals complex formed by the reactant molecules in the entry channel.

The forward IRC of the asymmetric saddle point SP2 toward the reactants 2O₂ + H₂ could not be calculated by following the direction of the eigenvector associated to its imaginary frequency. This eigenvector is located almost exclusively on the last-formed O–H bond (see SP2 in Figure 3.3(a)), and does not drive the IRC to the dissociation of the first-formed O–H bond. A similar situation was observed for the saddle point SP3, in which the eigenvector of its imaginary frequency mainly describes a torsional motion.

Failure of CCSD = FC/cc-pVTZ level of theory at optimization of SP2 and SP3 as well as failure of IRC calculations in connecting them with reactants 2O₂ + H₂ prevent us from relating SP2 and SP3 to the studied termolecular reactions with certainty. Thus, we propose SP2 and SP3 as candidate saddle points for the reactions 2O₂ + H₂ → 2HO₂ and 2O₂ + H₂ → H + HO₂ + O₂, respectively. With the information we obtained from the MD simulations and the electronic structure calculations no further insights can be inferred on the connection of these saddle points.

It is informative to look at the molecular orbitals, which are illustrated in Figure 3.4, to understand the relative energies of the various saddle points. The MOs in Figure 3.4 show why the symmetric termolecular saddle point SP1 is lower in energy than the others saddle points. These MOs in SP1 are formed by the Π_x and Π_x^* orbitals of the O_2 molecules, i.e. the orbitals orthogonal to those forming the double bond. While the MO shown in Figure 3.4(a) is formed by the doubly occupied Π_x orbitals of the O_2 molecules, with a small contribution of the σ bond of the H_2 molecule, the MO shown in Figure 3.4(b) is formed by the singly occupied Π_x^* orbitals, SOMOs orbital, also with a small contribution of the σ bond of the H_2 molecule. These two molecular orbitals are responsible for the interaction of the three molecules involved in the reaction through the $\Pi_x-\sigma-\Pi_x$ and $\Pi_x^*-\sigma-\Pi_x^*$ networks, being particularly stable and resulting in a highly symmetric saddle point not high in energy. This suggests that in the termolecular reaction $2O_2 + H_2 \rightarrow 2HO_2$ *via* the symmetric saddle point SP1, both O_2 molecules actively take part, and are involved to the same extent in the breaking and making of the bonds. We did not observe the formation of such MOs promoting the $\Pi_x-\sigma-\Pi_x$ and $\Pi_x^*-\sigma-\Pi_x^*$ interactions in the asymmetric saddle point SP2. The Π_x (see Figures 3.5(a) and 3.5(b)) and Π_x^* (see Figures 3.5(c) and 3.5(d)) MOs of both O_2 molecules and the σ MO of the H_2 molecule do not overlap, resulting in a non-symmetric and higher energy saddle point. This is also the case for SP3.

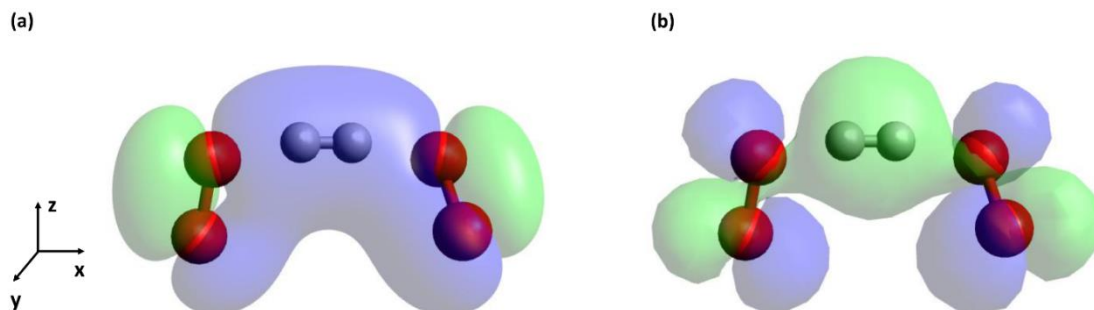


Figure 3.4: Molecular orbitals at SP1, the symmetric saddle point on the $2\text{O}_2 + \text{H}_2 \rightarrow 2\text{HO}_2$ triplet PES, formed by the (a) Π_x and (b) Π_x^* orbitals of the $\text{O}_2(^3\Sigma_g^-)$ molecules. The Π_x and Π_x^* orbitals are orthogonal to the double bond.

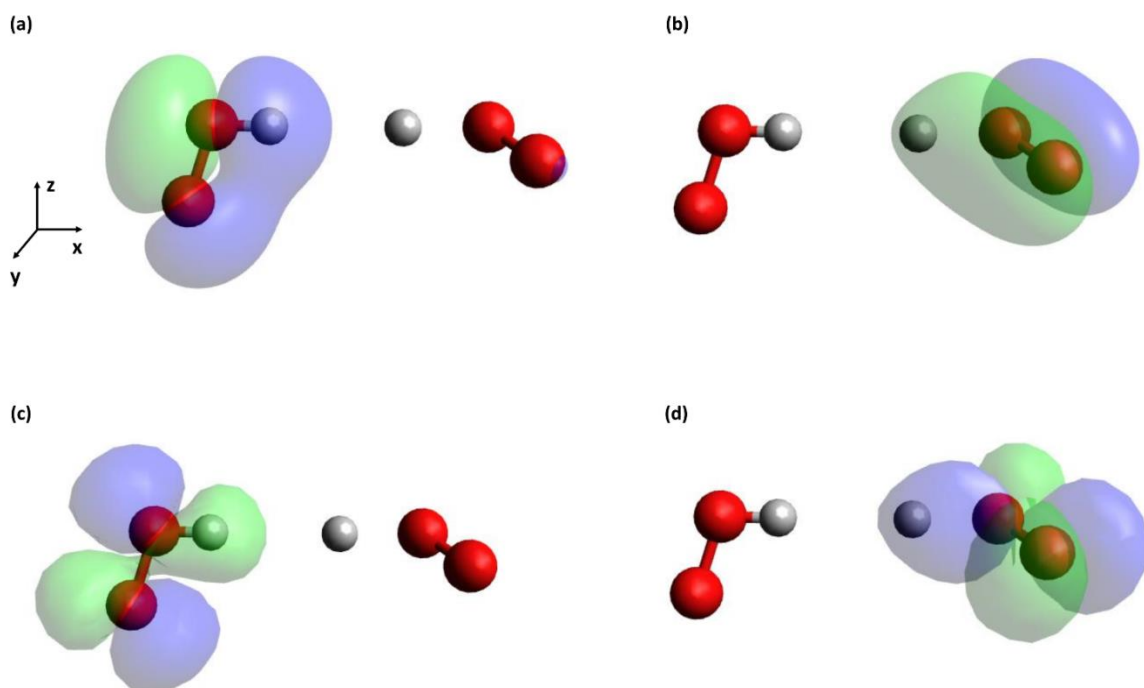


Figure 3.5: Molecular orbitals at SP2, the asymmetric saddle point on the $2\text{O}_2 + \text{H}_2 \rightarrow 2\text{HO}_2$ triplet PES, formed by the Π_x , (a) and (b), and Π_x^* , (c) and (d), orbitals of the $\text{O}_2(^3\Sigma_g^-)$ molecules. The Π_x and Π_x^* orbitals are orthogonal to the double bond.

The CCSD(T) method describes well the dynamic correlation and long-range dispersion energies, considered as a method giving accurate results. However, for chemical problems in which the multi-reference character is important, this method may fail. The multi-reference character of the stationary points found in this work was estimated using the $T1$ diagnostic by Lee and Taylor,¹¹⁷ which assesses the importance of the static correlation.

Values of $T1$ greater than 0.02 usually claim for multi-reference methods. However, it has been suggested that open-shell $T1$ values can be greater than those of closed-shell species, and values up to 0.04 are considered as acceptable for the former case.¹²²⁻¹²⁴ Some examples are the $\text{HO}_2(^2\text{A}')$ and CN radicals, which show $T1$ values larger than 0.03 and 0.04, respectively, at the CCSD/DZP and CCSD(T)/TZ2P levels,¹²³ but are very well described by coupled cluster theory.¹²⁵⁻¹²⁹ Other recent examples are the saddle points for the reactions between methanimine (CH_2NH) and the HO_2 radical, with values up to 0.04.¹²⁴

We believe this situation applies to the stationary points found for the reactions studied in this work; the saddle points show the largest $T1$ values: 0.02, 0.03 and 0.04 for the reactions $2\text{O}_2 + \text{H}_2 \rightarrow \text{H} + \text{HO}_2 + \text{O}_2$, $\text{H}_2 + \text{O}_2 \rightarrow \text{H} + \text{HO}_2$ and $2\text{O}_2 + \text{H}_2 \rightarrow 2\text{HO}_2$, respectively. In spite of the large $T1$ value, Michael *et al.*⁵² proved that the saddle point of the reaction $\text{H}_2 + \text{O}_2 \rightarrow \text{H} + \text{HO}_2$ is well characterized by the coupled cluster theory, reproducing the experimental rate constant, which is very sensitive to the barrier height.

The validity of the single-reference methods used in our calculations was further checked by performing CASSCF calculations with dynamic correlation, that is, CASSCF MP2.¹⁰⁹ The termolecular saddle points we report in this work turned out to be elusive

stationary points on the PESs: it was hard to find and optimize them and our attempts did not succeed with other methods and/or basis sets. We encountered the same troubles with the CASSCF MP2 calculations, and we were not able to optimize any of the saddle points with that method. Thus, we performed single point calculations at the CASSCF MP2/6-31G//MP2/6-31G level.

For the CASSCF MP2 calculations we only considered those molecular orbitals (MOs) with contributions of the orbitals 1s and/or 2p of the hydrogen and oxygen atoms, respectively; the energy of the reactants was obtained keeping the O₂ and H₂ reactants separated by 20 Å. The active space of the bimolecular saddle point SP consists of 8 electrons and 10 orbitals (CASSCF(8,10)), resulting in a barrier height of 51.7 kcal/mol, that is, only 1.9 kcal/mol larger than that at the CCSD(T)=FC/cc-pVTZ//MP2/6-31 level.

For the termolecular saddle points SP1, SP2, and SP3 we considered different active spaces. In the case of the symmetric saddle point SP1, the inclusion of the MOs formed by the Π and Π^* orbitals of the O₂ and the σ orbital of the H₂ (Figure 3.4) turned out to be important for an accurate estimation of the energy. Thus, the active spaces of the saddle points SP1, SP2, and SP3 are (12,12), (10,12) and (8,10), respectively, resulting in barrier heights of 48.6 kcal/mol, 51.1 kcal/mol and 54.5 kcal/mol, respectively. While the CASSCF MP2/6-31G//MP2/6-31G results for the saddle points SP1 and SP2 are in good agreement with those reported at the CCSD(T)=FC/cc-pVTZ//MP2/6-31G and CCSD(T)=FULL/aug-cc-pVTZ//CCSD=FC/cc-pVTZ levels (see Table 3.2), the saddle point SP3 shows larger discrepancies in the barrier height (6.1 kcal/mol, see Table 3.2).

To sum up, the CASSCF MP2/6-31G//MP2/6-31G level predicts the saddle point of the reaction $2\text{O}_2 + \text{H}_2 \rightarrow \text{H} + \text{HO}_2 + \text{O}_2$ (SP3) to be the most energetic, whereas the

CCSD(T)=FC/cc-pVTZ//MP2/6-31G and CCSD(T)=FULL/aug-cc-pVTZ//CCSD=FC/cc-pVTZ levels predict that saddle point to be SP2, that is, the saddle point of the asynchronous pathway of the reaction $2\text{O}_2 + \text{H}_2 \rightarrow 2\text{HO}_2$. However, the three *ab initio* levels predict the synchronous pathway of the termolecular reaction $2\text{O}_2 + \text{H}_2 \rightarrow 2\text{HO}_2$ to be the pathway with the lowest barrier height. The intermediate complexes found on the triplet PESs have lower *TI* values than the saddle points, thus a good performance of the CCSD(T)=FC/cc-pVTZ//MP2/6-31G and CCSD(T)=FULL/aug-cc-pVTZ//CCSD=FC/cc-pVTZ levels can be expected for them too.

A kinetic study is beyond the goals of the current section; however, given the large differences between the barrier heights to $\text{H}_2 + \text{O}_2 \rightarrow \text{H} + \text{HO}_2$ and the synchronous pathway of $2\text{O}_2 + \text{H}_2 \rightarrow 2\text{HO}_2$ (9.1 kcal/mol at the CCSD(T)=FULL/aug-cc-pVTZ//CCSD=FC/cc-pVTZ level), we can presume significantly larger rate constants for this termolecular pathway at sufficiently high pressures, when the termolecular collisions are frequent. These findings support what Karkach and Oshero⁷² postulated about the dominant role of the termolecular reaction $2\text{O}_2 + \text{H}_2 \rightarrow 2\text{HO}_2$ at high pressures in the early chemistry of hydrogen combustion.

ReaxFF was parameterized to account for the electronic ground-state of the H_2 and O_2 species;⁶⁴ however, it is our understanding (in fact, we verified this in Chapter 2, see Figure 2.1) that it was not parameterized to account for the manifold of PESs that arise when two ground-state $\text{O}_2(^3\Sigma_g^-)$ molecules interact. Therefore, a better performance of the force field can be expected for the $\text{O}_2(^3\Sigma_g^-)\text{--}\text{O}_2(^3\Sigma_g^-)$ interactions when the $\text{O}_2(^3\Sigma_g^-)$ molecules are widely separated and the splitting is negligible. Despite the fact that this splitting may not be accurately described by ReaxFF, it does appear to be qualitatively

right in that the barriers to the termolecular reactions are lower than that for $\text{H}_2 + \text{O}_2 \rightarrow \text{H} + \text{HO}_2$. However, while ReaxFF quantitatively predicts the barrier height for the bimolecular reaction $\text{H}_2 + \text{O}_2 \rightarrow \text{H} + \text{HO}_2$ nearly accurately (57.13 kcal/mol computed by the NEB method comparing to 58.9 kcal/mol calculated at CCSD(T)=FULL/aug-cc-pVTZ//CCSD=FC/cc-pVTZ single point *ab initio* level of theory), it fails spectacularly to predict the barrier height for the termolecular reaction $2\text{O}_2 + \text{H}_2 \rightarrow 2\text{HO}_2$ (13.66 kcal/mol computed by the NEB method comparing to 49.8 kcal/mol calculated at CCSD(T)=FULL/aug-cc-pVTZ//CCSD=FC/cc-pVTZ single point *ab initio* level of theory). This could be due to several reasons: **(1)** unlike reaction $\text{H}_2 + \text{O}_2 \rightarrow \text{H} + \text{HO}_2$, the termolecular reaction $2\text{O}_2 + \text{H}_2 \rightarrow 2\text{HO}_2$ was not used to obtain the QM training data set for developing the force field; **(2)** ReaxFF fails in accurately characterizing the interaction between two ground-state oxygen molecules as well as predicting the splitting of the potential energy surface for their interaction; see top frame of Figure 2.1; and **(3)** ReaxFF was developed under the assumption of the pairwise additive potential, therefore, it is expected to fail in accurately prediction of termolecular reactions like $2\text{O}_2 + \text{H}_2 \rightarrow 2\text{HO}_2$ where reactants are a cluster of three species.

The energetics of the two most prominent reactions identified in our simulations are summarized in Figure 3.6, which shows the classical potential energy diagram with the stationary points found at the CCSD(T)=FULL/aug-cc-pVTZ//CCSD=FC/cc-pVTZ *ab initio* level on the triplet PESs of $2\text{O}_2 + \text{H}_2 \rightarrow 2\text{HO}_2$ (the top frame) and (b) $\text{H}_2 + \text{O}_2 \rightarrow \text{H} + \text{HO}_2$ (the bottom frame) *via* the symmetric saddle point SP1 and the saddle point SP, respectively. These energies also include the basis set superposition error correction. The

termolecular reaction is also thermodynamically favored with reaction energy 0.26 kcal/mol, much lower than the value obtained for the bimolecular reaction, 54.4 kcal/mol.

The saddle point SP1 is located on the reaction path for the formation of the 2HO_2 products either *via* a direct mechanism or through the formation of different hydrogen-bonded intermediate complexes located on the post-transition state region (also on the triplet PES). These complexes may be converted into each other by internal rotations of the HO_2 fragments, and can be also stabilized by third body collisions, forming $\text{H}_2\text{O}_2 + \text{O}_2$ instead of 2HO_2 radicals.

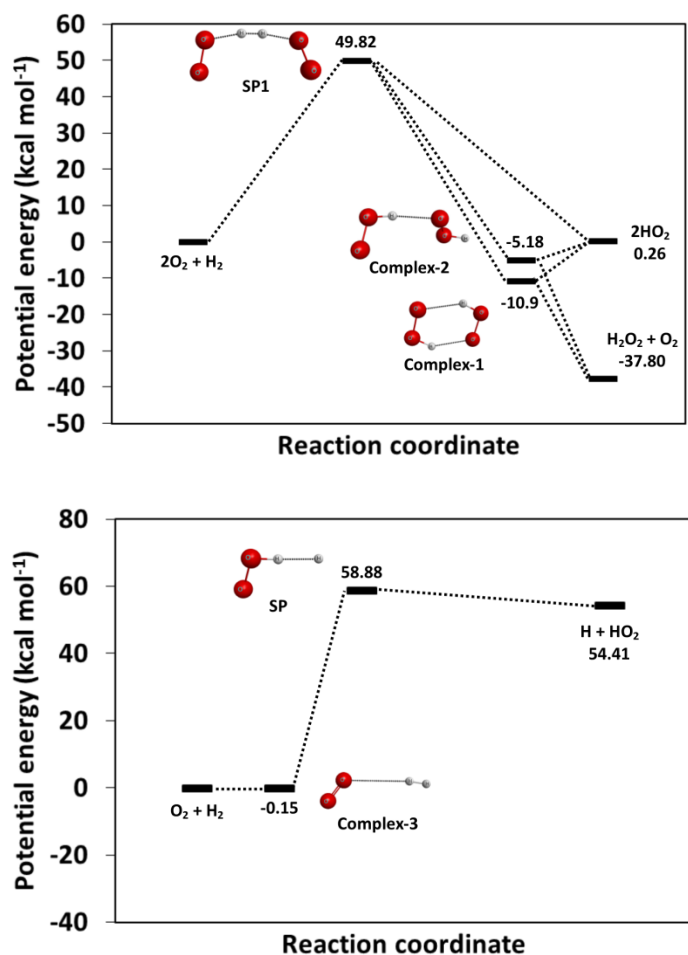


Figure 3.6: Classical potential energy profile with the energy (kcal/mol), with respect to the reactants, and optimized geometry, of the stationary points found on the triplet

potential energy surfaces of the termolecular $2\text{O}_2 + \text{H}_2 \rightarrow 2\text{HO}_2$ (the top panel) and bimolecular $\text{H}_2 + \text{O}_2 \rightarrow \text{H} + \text{HO}_2$ (the bottom panel) reactions at the CCSD(T)=FULL/aug-cc-pVTZ//CCSD=FC/cc-pVTZ *ab initio* level

3.4 EFFECTS OF TEMPERATURE ON THE EARLY CHEMISTRY OF HYDROGEN COMBUSTION

The effect of density on the early chemistry of hydrogen combustion was addressed in Chapter 2.4. We showed that at constant temperature, the probability of finding the termolecular reaction $2\text{O}_2 + \text{H}_2 \rightarrow 2\text{HO}_2$ as the initial reaction in hydrogen combustion increases with density. This increase was justified in term of the dependence of ter- and bi-molecular collision frequencies on density. We showed that while the bimolecular collision frequency is linearly dependent on density, the termolecular collision frequency manifests a nonlinear, more rapid growth with density which results in termolecular reaction becoming more likely at higher densities. However, as shown in panels of Figure 2.11, at a constant density the termolecular reaction $2\text{O}_2 + \text{H}_2 \rightarrow 2\text{HO}_2$ becomes less less probable relative to the bimolecular reaction $\text{H}_2 + \text{O}_2 \rightarrow \text{H} + \text{HO}_2$ as temperature increases from 3,000 K to 5,000 K. This is despite the fact that the ratio of termolecular collision frequency to bimolecular collision frequency increases by \sqrt{T} as given by Eq. (16) in Chapter 2. In other words, although the frequency of the termolecular collisions $\text{O}_2 \cdots \text{H}_2 \cdots \text{O}_2$ is more favored than that of bimolecular collisions $\text{H}_2 \cdots \text{O}_2$ by elevation of the temperature (see Figure 2.15), the occurrence probability of the termolecular reaction is decreasing.

The different effect of temperature on the occurrence probability of the bi- and ter-molecular reactions can be explained in term of the difference in the barrier heights to both reactions. Due to its higher barrier height, the reaction $O_2 + H_2 \rightarrow H + HO_2$, which is favored by the collision frequency (the termolecular collision frequency is smaller than that of the bimolecular by almost 30 factors), is more enhanced when temperature increases since the number of reactant molecules with enough energy to surmount the barrier height increases significantly. Therefore, the difference between the barrier heights to $2O_2 + H_2 \rightarrow 2HO_2$ and $O_2 + H_2 \rightarrow H + HO_2$ (about 9 kcal/mol at the CCSD(T)=FULL/aug-cc-pVTZ//CCSD=FC/cc-pVTZ *ab initio* level) becomes a less decisive factor in the competition between the reactions as temperature increases. The energy requirement to overcome the barrier height implies that sum of the internal energies and relative translational energy of the colliding molecules must exceed the barrier height, ΔV ; that is

$$\sum_{\text{reactants}} E_{\text{int}} + E_{\text{rel}} \geq \Delta V \quad (4)$$

where E_{int} and E_{rel} are the internal energies (rotational plus vibrational) and relative translational energy of reactant species which reacts. For a diatomic molecule in the classical limit the average E_{int} is equal to $2RT$ according to equipartition theorem. Therefore, for the energy requirement to be satisfied, the relative translational energy of the colliders must exceed a minimum value of $(E_{\text{rel}})^*$ which is equal to

$$(E_{\text{rel}})^* = \Delta V - 2NRT \quad (5)$$

where N is the molecularity of the collision; 2 for bi- and 3 for ter-molecular collisions. Note that we ignored the restriction might be imposed due to the conservation of the total angular momentum.

The probability of finding an N -molecular collision fulfilling Eq. (4) can be calculated by integrating the generalized Boltzmann factor for the relative translational energy for energy values greater than $(E_{\text{rel}})^*$; that is,

$$\text{Pr} = (2\pi\mu_N\kappa T)^{-\frac{3(N-1)}{2}} \int \cdots \int_{(E_{\text{rel}})^*}^{\infty} \exp\left(\frac{-E_{\text{rel}}}{\kappa T}\right) d^{3(N-1)} \mathbf{P} \quad (6)$$

where \mathbf{P} is the relative momentum vector and μ_N is the N -molecular reduced mass. Here we used the barrier heights predicted by electronic structure theory at CCSD(T) = FULL/aug-cc-pVTZ//CCSD = FC/cc-pVTZ single point *ab initio* level (49.8 kcal/mol and 58.9 kcal/mol for ter- and bi-molecular reactions, respectively) to calculate the minimum relative translational energy in Eq. (5). The probability for a ter- and bi-molecular collision satisfying the energy requirement of Eq. (4) was calculated using Eq. (6) and the results are given in Table 3.3. As it is inferred from Table 3.3, at 3,000 K, while about 58% of the termolecular collisions $\text{O}_2 \cdots \text{H}_2 \cdots \text{O}_2$ fulfill the energy requirement of Eq. (4), only less than 1% of bimolecular collisions $\text{H}_2 \cdots \text{O}_2$ meet the energy requirement. However, as temperature elevates, the probability of finding a bimolecular collision satisfying Eq. (4) increases more significantly (at 4,000 K, for instance, the increase is about 10 orders of magnitude for termolecular collisions while is only 2 orders of magnitude for bimolecular collisions) which by itself increases the probability of finding a bimolecular reaction initiating the early chemistry of hydrogen combustion.

Table 3.3: The probabilities of fulfillment of energy requirement of Eq. (4) for the ter- and bi-molecular reactions, respectively, at 3,000 K, 4,000 K, and 5,000 K.

| | 3,000 K | 4,000 K | 5,000 K |
|--|----------------|----------------|----------------|
| Termolecular | | | |
| $\sum_{\text{reactants}} \langle E_{\text{int}} \rangle$ | 35.76 | 47.68 | 59.61 |
| $(E_{\text{rel}})^*$ | 14.04 | 2.12 | 0.0 |
| Probability | 0.581 | 0.997 | 1 |
| Bimolecular | | | |
| $\sum_{\text{reactants}} \langle E_{\text{int}} \rangle$ | 23.84 | 31.79 | 39.74 |
| $(E_{\text{rel}})^*$ | 35.06 | 27.11 | 19.16 |
| Probability | 0.008 | 0.078 | 0.277 |

The average internal energy was calculated in accordance with the equipartition theorem: $2RT$ for a diatomic. $(E_{\text{rel}})^*$ and probabilities were computed using Eqs. (5) and (6), respectively. All energy values are in kcal/mol.

Therefore, based on the results of Table 3.3, we can conclude that at lower temperatures, the termolecular reaction $2\text{O}_2 + \text{H}_2 \rightarrow 2\text{HO}_2$ plays a more important role than the bimolecular reaction $\text{O}_2 + \text{H}_2 \rightarrow \text{H} + \text{HO}_2$ in the early chemistry of hydrogen combustion. Our findings support the assumption made by Karkach and Oshero⁷² who postulated that the reaction $2\text{O}_2 + \text{H}_2 \rightarrow 2\text{HO}_2$ may be important at elevated pressures and low temperatures. It should be noted that since the ReaxFF prediction of the barrier height to the termolecular reaction is lower than that of predicted by electronic structure calculations by about 35 kcal/mol, the occurrence probability of the termolecular reaction might be significantly overestimated.

3.5 STERIC EFFECTS

In the Section 3.4, we showed that at 3,000K, while 58% of the termolecular collisions $2\text{O}_2 + \text{H}_2$ have enough energy to surmount the energy barrier for the reaction $2\text{O}_2 + \text{H}_2 \rightarrow 2\text{HO}_2$, less than 1% of the bimolecular collisions $\text{O}_2 + \text{H}_2$ satisfy the energy requirement for the reaction $\text{O}_2 + \text{H}_2 \rightarrow \text{H} + \text{HO}_2$. However, at 3,000 K the occurrence probability of the termolecular reaction is still unexpectedly lower than that of the bimolecular reaction except at extremely high density; see Figure 2.11. In this section, we seek to address this matter by identifying the angular constraints, which is referred to as steric effects, for the termolecular and bimolecular reactions.

We closely studied 50 individual reaction clusters for each reaction at 3,000 K. During the interval between formation of each reaction cluster, that is when $r_{\text{O}_i\text{H}_j} \leq 1.8 \text{ \AA}$, and rupturing of the H-H bond, that is $r_{\text{H-H}} \geq 1.5 \text{ \AA}$, at every integration step we computed the bond angle(s) and the dihedral angle. Combining the results of 50 individual reaction clusters, we obtained the distributions of the bond and dihedral angles for the termolecular and bimolecular reaction clusters; see Figure 3.7.

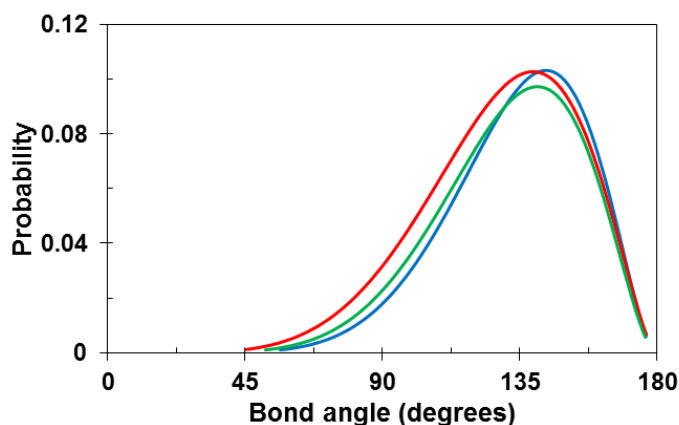


Figure 3.7: The probability distribution of the bond angle(s) α O–O–H for the bimolecular (green) and termolecular (red and blue) reaction clusters. The probability

distributions are fitted to the beta distribution function and were obtained for the bond angles of 50 individual reaction clusters calculated during the interval between formation of each reaction cluster and rupturing of the H-H bond.

As shown in Figure 3.7, for 90% of the reaction clusters, the bond angles α $\angle\text{O-O-H}$ fall in interval of (115, 155) with the maximum probability at 135 degrees. Although the bond angle distributions are same for both termolecular and bimolecular reaction clusters, the termolecular reaction clusters are constrained by two bond angle restrictions. In other words, for a termolecular collision to become reactive, two spatial requirements must be fulfilled which lowers the probability of reaction occurrence. As for the dihedral angle, we did not find any specific constraint for both reactions.

It must be noted that at elevated temperatures like those set for this study, $T > 3,000$ K, collision encounters had enough kinetic energy to escape the potential well, and thus reactant complex did not form. For the termolecular reaction, for instance, despite the potential well of -12.46 kcal/mol, as predicted by ReaxFF, the average total kinetic energy of collision clusters $2\text{O}_2 + \text{H}_2$ is $\frac{21}{2}RT$, 62.59 kcal/mol for $T = 3,000$ K, based on equipartitioning of the energy ($\frac{7}{2}RT$ for each diatomic). Therefore, the encounters almost never trap in the potential well and formation of reactant complex is very unlikely. In such elevated temperatures where encounters behave like hard spheres, the spatial constraints are satisfied randomly depending on the orientation of molecules as they enter a collision. In other words, since collisions do not lead to formation of reactant complexes, colliders do not have enough time for the intermolecular rearrangements to

satisfy the spatial constraints for the bond angles beyond purely statistical expectations. This is what we observed in the simulations where the center of mass distance of the colliders reduces with time, passes through a minimum (moment of collision), and then increases monotonically. The length of collision duration, as Tolman⁹⁸ suggested, is only an indication of largeness or smallness of the relative translational energy of the encounters. However, at low temperatures, termolecular encounters are more capable of getting trapped in the potential well to form a complex. Therefore, a termolecular collision at low temperatures more likely promotes a reaction since molecules have more time for the intermolecular rearrangements to meet the spatial requirements within a long-lived complex. This increases the occurrence probability of the termolecular reaction relative to that of bimolecular reaction.

4. GENERAL APPLICATION OF TOLMAN'S CONCEPT OF ACTIVATION ENERGY

The Arrhenius activation energy E_a is an empirical parameter given by the slope of a plot of $\ln k(T)$ versus $1/T$, where $k(T)$ is the reaction rate coefficient at temperature T .

When E_a is independent of T the Arrhenius equation is

$$E_a = -\kappa \, d \ln k(T) / d (1/T), \quad (1)$$

where κ is Boltzmann's constant. In 1920 Tolman¹³⁰ presented an interpretation of the activation energy of an elementary gas-phase bimolecular reaction under thermal conditions as the difference in the average internal plus relative translational energy of reacting pairs \bar{E}_{react} and the average total energy of colliding pairs of reactants $\bar{E}_{\text{colliding}}$ plus $\frac{1}{2}\kappa T$; that is,

$$E_a = \bar{E}_{\text{react}} - \bar{E}_{\text{colliding}} + \frac{1}{2}\kappa T. \quad (2)$$

The second term on the right-hand-side is the sum of the average relative translational energy of colliding pairs $(\bar{E}_{\text{rel}})_{\text{colliding}}$ and the average of the internal energies of the colliding pairs \bar{E}_{int} ; that is,

$$\bar{E}_{\text{colliding}} = (\bar{E}_{\text{rel}})_{\text{colliding}} + \bar{E}_{\text{int}}; \quad (3)$$

where $(\bar{E}_{\text{rel}})_{\text{colliding}}$ is given by

$$(\bar{E}_{\text{rel}})_{\text{colliding}} = \frac{\int_0^{\infty} \sigma(E_{\text{rel}}, T) E_{\text{rel}}^2 \exp\left(\frac{-E_{\text{rel}}}{\kappa T}\right) dE_{\text{rel}}}{\int_0^{\infty} \sigma(E_{\text{rel}}, T) E_{\text{rel}} \exp\left(\frac{-E_{\text{rel}}}{\kappa T}\right) dE_{\text{rel}}}, \quad (4)$$

and $\sigma(E_{\text{rel}}, T)$ is the collision cross-section.

Fowler and Guggenheim¹³¹ defined E_a as \bar{E}_{react} minus \bar{E}_{all} , the average internal plus relative translational energy of all pairs of reactants:

$$\bar{E}_{\text{all}} = (\bar{E}_{\text{rel}})_{\text{all}} + \bar{E}_{\text{int}}, \quad (5)$$

where $(\bar{E}_{\text{rel}})_{\text{all}}$ is the average relative translational energy of all pairs of reactants, $\frac{3}{2}\kappa T$. The difference between the average energy of colliding pairs and average energy of all pairs is $\frac{1}{2}\kappa T$, which appears explicitly in Eq. (2). This difference is due to the fact that colliding pairs more frequently involve reactants with larger E_{rel} . Therefore, the average E_{rel} for colliding pairs is greater than that of for all pairs. This can be verified for the hard-sphere model where the reaction cross section is independent of E_{rel} . For the hard-sphere model, $(\bar{E}_{\text{rel}})_{\text{colliding}}$ given by equation (4) results in $2\kappa T$ that exceeds $(\bar{E}_{\text{rel}})_{\text{all}}$ by $\frac{1}{2}\kappa T$. Thus, the Fowler and Guggenheim expression is equivalent to the one by Tolman.

A more general and rigorous derivation was given by Truhlar¹³² based on chemical dynamics. Truhlar's derivation rests on the assumption of local equilibrium,¹³³ that is, an equilibrium distribution of translational and internal energies of the reactants. The earlier versions were based on the assumption of global equilibrium. Truhlar's general equation for the activation energy of a bimolecular gas-phase reaction $A + B \rightarrow \text{products}$ is

$$E_a = (\bar{E}_{\text{rel}} + \bar{E}_{\text{int}})_{\text{react}} - [(\bar{E}_{\text{rel}})_{\text{all}} + (\bar{E}_{\text{int}})_A + (\bar{E}_{\text{int}})_B]; \quad (6)$$

that is, the activation energy is the difference in the “average energy of the reacting pairs” (relative translational plus internal) and the “average energy of all pairs of reactants”. In Eq. (6) $(\bar{E}_{\text{int}})_A$ and $(\bar{E}_{\text{int}})_B$ are the average internal energies of reactants A and B, respectively.

The Tolman activation energy depends on the average relative translational energy of all pairs of reactants, $(\bar{E}_{\text{rel}})_{\text{all}}$, and the average internal energies of reactants, thus it has been applied to describe the temperature dependences of activation energies $E_a(T)$ of reactions; that is, predicts the curvature of Arrhenius plots.¹³⁴⁻¹³⁶ Allison *et al.*¹³⁵ used it to explain the curved Arrhenius plot they computed for the $\text{Cl} + \text{H}_2 \rightarrow \text{HCl} + \text{H}$ system. They explained the doubling in the activation energy over the experimental temperature range 200 K to 2500 K.¹³⁷⁻¹⁴⁰ Another example was reported by Haddadi *et al.*¹³⁶ They observed an Arrhenius convex curve for Ti⁺ ion intramolecular exchange reaction between the two crown sides of the Calix[4]crown-6 ligand, which they attributed to the first term on the left-hand-side of Eq. (6). They showed that the average of energy of the reacting systems increases less rapidly than does the Boltzmann average energy. Inagaki

and Yamamoto¹³⁴ showed that the activation energy of a deep hydrogen tunneling process is describable by Tolman's interpretation. They explained that for a reaction dominated by tunneling the average energy of the reacting molecules is equivalent to the average tunneling energy; that is, the activation energy is the average tunneling energy minus the average energy of molecules.

Tolman's concept has typically been applied to bimolecular reactions; however, it can be applied to reactions of any molecularity.^{141,142} Truhlar and Kohen,¹⁴¹ for instance, used it to explain the positive convexity of the Arrhenius plots of enzyme catalyzed reactions,¹⁴³⁻¹⁴⁵ specifically a thermal unimolecular dissociation. Their analysis shows that the convex Arrhenius plot is due to either the decreasing or less rapidly increasing of the average energy of dissociating molecules than the average energy of all molecules as the temperature increases.¹⁴¹ Gilbert and Ross¹⁴² proved that the activation energy of unimolecular reactions has the form of Tolman's equation in the high-pressure limit. However, they showed that Tolman's expression cannot accurately predict the activation energy of a unimolecular reaction in the low-pressure limit unless it is corrected to account for the depletion of the Boltzmann distribution by reactions. They also showed that the expression for the activation energy of a unimolecular reaction in the low-pressure limit needs another correction factor to account for energy dependence of collisional vibrational excitation and de-excitation of the reactant molecules.¹⁴²

Defining relative translation motion for three or more particles (ignoring internal degrees of freedom) is not straightforward. Smith^{146,147} generalized collision parameters such as relative translation motion to termolecular clusters by transformation to the center-of-mass coordinate system. The transformation reduces the configuration space of

three particles to three-dimensions. The classical canonical partition function for this reduced space is

$$L(T) = \frac{1}{h^6} \int_{-\infty}^{\infty} d^6 \mathbf{r} \int_{-\infty}^{\infty} \exp\left(-\frac{E_{\text{rel}}}{\kappa T}\right) d^6 \mathbf{P} \quad (7)$$

$$= \frac{(2\pi\mu\kappa T)^3}{h^6} V^2, \quad (8)$$

where E_{rel} is the relative translational energy of three particles, \mathbf{P} is the generalized vector of relative linear momentum, \mathbf{r} is the generalized vector of relative position, and μ is the reduced mass. Therefore, the Maxwell's law for the relative motion of three particles is

$$V^{-2} \int_{-\infty}^{\infty} d^6 \mathbf{r} (2\pi\mu\kappa T)^{-3} \int_{-\infty}^{\infty} \exp\left(-\frac{E_{\text{rel}}}{\kappa T}\right) d^6 \mathbf{P} = 1. \quad (9)$$

To obtain the average relative translational energy of three particles we need to evaluate the momentum integral; that is,

$$\bar{E}_{\text{rel}} = (2\pi\mu\kappa T)^{-3} \int_{-\infty}^{\infty} \exp\left(-\frac{E_{\text{rel}}}{\kappa T}\right) d^6 \mathbf{P} \quad (10)$$

$$= \pi^3 (2\pi\mu\kappa T)^{-3} \int_{-\infty}^{\infty} E_{\text{rel}} \exp\left(-\frac{E_{\text{rel}}}{\kappa T}\right) p^5 dp, \quad (11)$$

where p is the magnitude of relative linear momentum and is equal to $p = \sqrt{2\mu E_{\text{rel}}}$.

Therefore, Eq. (11) becomes

$$\begin{aligned}\bar{E}_{\text{rel}} &= \pi^3 (2\pi\mu\kappa T)^{-3} 4\mu^3 \int_0^{\infty} E_{\text{rel}}^2 \exp\left(-\frac{E_{\text{rel}}}{\kappa T}\right) dE_{\text{rel}} \\ &= 3\kappa T.\end{aligned}\tag{12}$$

In this Chapter, we present a generalization of Tolman's concept of activation energy applicable to analysis of thermal and non-thermal reactions in molecular dynamics simulations of reactions in bulk gases. To illustrate the applicability of the method calculations were carried out to determine the activation energies of bimolecular reaction $\text{O}_2 + \text{H}_2 \rightarrow \text{H} + \text{HO}_2$ and termolecular reaction $2\text{O}_2 + \text{H}_2 \rightarrow 2\text{HO}_2$ from canonical MD simulation results for $[\text{H}_2]/[\text{O}_2] = 1$ at 3,000 K using the reactive force field ReaxFF. Later, in this Chapter, we apply the method to get the activation energies for the critical elementary reactions occurring in NVE simulations of thermal dissociation of 10 hydrogen peroxide molecules equilibrated at initial temperature of 2,100 K and density of $275.6 \text{ kg}\cdot\text{m}^{-3}$.

4.1 GENERALIZED TOLMAN ACTIVATION ENERGY

The activation energy as given in Eq. (6) is an ensemble average over the activation energies of individual bimolecular gas-phase reactions. Since each reaction is local in the Boyd sense,¹³³ a more general definition of E_a than Eq. (6) that includes reactions of any

molecularity is the difference between the average local energy of reactants that react $(\bar{E}_{\text{local}})_{\text{react}}^0$ and the average energy of all clusters of reactants; that is,

$$E_a = (\bar{E}_{\text{local}})_{\text{react}}^0 - [(\bar{E}_{\text{rel}})_{\text{all}} + (\bar{E}_{\text{int}})_A + (\bar{E}_{\text{int}})_B]. \quad (13)$$

Here we apply this approach to thermal reactions to demonstrate its applicability for determining the reaction requirements of reaction in simulations of bulk gases. Note that the quantities in the square brackets can be computed during the course of any simulation of bulk gases, including the reactions the non-thermal products of earlier reactions. This will be addressed later in this Chapter.

It is necessary to identify those atoms in a bulk simulation that are involved in a given reaction, and to compute the Tolman (internal plus relative translational) energy of that cluster of atoms; which we refer to as the *reaction cluster local energy* (RCLE). The Tolman energy of a cluster of atoms depends on the chemical bonding. The Tolman energy is a part of the total energy (internal plus total translational) of a cluster of atoms that can influence an individual reaction. In other words, because we treat reaction clusters as conservative systems the difference between the total energy and the Tolman energy, which is the translational energy of the center-of-mass of the cluster, $E_{\text{trans,CoM}}$, does not contribute to the reaction.

The change with time of the RCLE for an individual reaction can be defined in a Lagrangian reference frame (denoted by subscript L) as the sum of appropriate terms for the energy source or sink $p(E)$ and for energy flow $q(E)$; that is,

$$\frac{dE_{\text{local}}}{dt} = \left(\frac{\partial E_{\text{local}}}{\partial t} \right)_{\text{L}} = p[E] + q[E], \quad (14)$$

where $p(E)$ is the rate of heat given off or used by a reaction due to formation or breaking of bonds and $q(E)$ is rate of flow of energy into or out of the RCLE of the reaction to an external energy bath. Integrating the left-hand-side of Eq. (14) over the reaction duration τ results in

$$\int_0^{t < \tau} dE_{\text{local}} = E_{\text{local}}(t) - E_{\text{local}}(t = 0) = t \times (p[E] + q[E]), \quad (15)$$

where $t = 0$ is a time before the reactants begin to interact and $t = \tau$ is the time at the end of the reaction. The local energy of an individual reaction is a dynamic quantity that evolves according to Eq. (14). The RCLE at the end of a reaction is

$$(E_{\text{local}})^\tau = (E_{\text{rel}} + E_{\text{int}})_{\text{react}}^0 + P[E] + Q[E], \quad (16)$$

where $P(E)$ is the heat change due to chemistry in the cluster; that is, the change in the potential energy upon conversion of reactants to products at constant volume; and $Q(E)$ is the change due to third-body effects, which are included in our definition of the cluster. Since the RCLE includes the potential energy of each species relative to separated atoms, $P(E)$ is also accounted for. Thus, the local energy is conserved in each reaction cluster; that is,

$$(E_{\text{local}}) = (E_{\text{rel}} + E_{\text{int}})_{\text{react}}^0 = (E_{\text{local}})^{\tau}. \quad (17)$$

Tolman's concept applies to non-thermal reactants as long as Boyd's local equilibrium assumption holds; that is, when the rate of relaxation of the translational energy is much faster than that of the internal modes, which is typically the case. For example, Dunbar¹⁴⁸ showed, based on a local equilibrium assumption, that the activation energy of a low-pressure, laser-driven dissociation reaction has the form of Eq. (6) plus two correction terms to account for the dependence of the overall rate of dissociation on the rate of laser pumping. Dunbar assumed that the thermal distributions for the translational and internal energies do not change during the time that the dissociation reaction occurs as a first-order process; that is, when the concentration of reactants are considerably larger than the concentration of products.

We illustrate the generalized Tolman activation energy (GTE_a) method for determining the activation energies of reactions in molecular dynamic simulations of the NVT ensemble of mixtures of H₂ and O₂ and NVE ensemble of 10 H₂O₂ molecules.

4.2 CANONICAL ENSEMBLE

4.2.1 COMPUTATIONAL METHODS

The 2014 version of the LAMMPS^{80,81} code was used to perform MD simulations in the NVT ensemble with the ReaxFF⁶⁴ force field. One hundred molecules with the equivalent ratio [H₂]/[O₂]=1 were simulated in a periodic box of dimensions 21×21×21 Å³. The temperature of the system was maintained at 3,000 K using the Nose-Hoover^{82,83} thermostat with damping constant 0.5 ps. The initial configurations were generated by

using the PACKMOL⁸⁹ code. The molecular internuclear distances, 0.75 Å and 1.18 Å for H₂ and O₂, respectively, were uniformly positioned in the simulation cell. The Polak-Ribiere⁹⁰ version of the conjugate-gradient algorithm was used to minimize the potential energy of the system; then atomic velocities were randomly selected from the Gaussian distribution for temperature T . The trajectories were propagated using the velocity Verlet^{12,13} integrator with time step 0.1 fs. The system was thermally equilibrated, which was confirmed by calculating the kinetic vibrational and rotational temperatures and comparing them to the target temperature. The equilibration was considered complete when the kinetic rotational and vibrational temperatures were equal to the target temperature. Complete equilibration required 15-25 ps. The bond distances were monitored during the equilibration to determine whether a reaction occurred. When a reaction did occur, the simulation was abandoned. The configurations of the system at the end of the equilibration simulations were used as the initial states for the production simulations, which were run for 2 ns.

Application of the GTE_a concept requires that the reaction molecularity be determined which was delivered using the reaction identification algorithm prescribed in Chapter 2. Beginning 125 fs before the time at which the bond rupture was detected, center-of-mass velocity of each molecule in the cluster was obtained from the LAMMPS output file to calculate the relative translational energy of the reactants E_{rel} ; that is,

$$E_{\text{rel}} = \sum_{i=1}^N E_{\text{trans},i} - E_{\text{trans,CoM}}, \quad (18)$$

where $E_{\text{trans},i}$ is the translational energy of the i^{th} species in the cluster, and $E_{\text{trans,CoM}}$ is the

translational energy of the center-of-mass of the cluster, and N is the molecularity of the reaction cluster. The relative translational energy E_{rel} was added to the sum of the vibrational and rotational energies of the species in the reaction cluster at every integration time step to give $(E_{\text{rel}} + E_{\text{int}})_{\text{react}}^0$, which was averaged over the 125 fs interval to give the local energy for the NVT ensemble:

$$(E_{\text{local}})_{\text{MD}}^{\text{NVT}} = \langle (E_{\text{rel}} + E_{\text{int}})_{\text{react}}^0 \rangle. \quad (19)$$

Averages of the internal energies of the all the H₂ and O₂ molecules were computed at every integration step from the beginning of the simulation. Time averages of these quantities were used in Eq. (19) to compute the activation energies of reactions in the MD simulations; that is,

$$(E_a)_{\text{MD}} = (\bar{E}_{\text{local}})_{\text{MD}}^{\text{NVT}} - \langle (\bar{E}_{\text{rel}})_{\text{all}} + (\bar{E}_{\text{int}})_{\text{A}} + (\bar{E}_{\text{int}})_{\text{B}} \rangle, \quad (20)$$

where $(\bar{E}_{\text{local}})_{\text{MD}}^{\text{NVT}}$ is the average of Eq. (19) over an ensemble (as indicated by the overbar) of individual reactions.

We computed the local energies and the thermal energies for reactant and product arrangements of a reaction cluster beginning 125 fs before the time at which reaction was detected. We defined the *local energy* (LE) curve for an individual reaction as the curve of minimum value of the local energies of reactants and products as the reaction progresses. The LE is the curve that connects the local energy of reaction at $t = 0$ to $t = \tau$,

that is it is the evolution of the RCLE, $E_{\text{local}}(t)$; see Eq. (15). We used the LE to verify the conservation of the RCLE, and thus validate Eq. (17) for the main initial reactions occurring in the NVT ensemble at $T = 3,000$ K and $\rho = 304.85 \text{ kg}\cdot\text{m}^{-3}$ for $[\text{H}_2]/[\text{O}_2] = 1$. Similarly, we defined the *thermal energy* (TE) curve for an individual reaction as the minimum value of the thermal energies of reactants and products as the reaction proceeds. The TE of each (reactants and products) was computed relative to the bottom of the potential energy well of the reactants or products; that is, we subtracted energy of the bottom of the potential well (measured relative to separated atoms) from the LE to obtain the TE.

There is a unique point on the LE curve for an individual reaction that separates reactants and products, which we call the *transition configuration* (TC). It is the point at which the local energy of the reactants is equal to that of the products. The TC is located at the maximum of the LE curve, and is a true measure of the energy requirement for the passage of reactants to products. Note that for a cluster of atoms the local kinetic energy, that is, sum of the relative translational energy and total kinetic internal energy, is independent of the arrangement of the atoms, and thus is the same for reactants and products, thus the TC is the point where the sum of the bonding potential energy of reactants is equal to that of products; that is,

$$\sum_{j=1}^m P.E.{}_j = \sum_{j'=1}^{m'} P.E.{}_{j'}. \quad (21)$$

The TC characterized by Eq. (21) echoes the nonadiabatic transition determined by Landau¹⁴⁹-Zener¹⁵⁰ curve crossing formulation. Borgis and Hynes¹⁵¹ showed that for proton transfer reactions and in absence of quantum effects the location of crossing point

is where the effective potentials in the solvent coordinate for the reactant and product states become equal. The same idea applies to electron transfer in Marcus theory where the transition state can be determined as where the energy of the valance-bond state of reactant equals to that of the product.

4.2.2 RESULTS AND DISCUSSION

We have calculated the Tolman activation energy, Eq. (20), using averages of 30 individual TCs for $\text{O}_2 + \text{H}_2 \rightarrow \text{H} + \text{HO}_2$ and for $2\text{O}_2 + \text{H}_2 \rightarrow 2\text{HO}_2$ calculated from the results of MD simulations of the NVT ensemble. We calculated the local (LE) and thermal energies (TE) for individual reactions to verify energy conservation of the RCLE. The LE and TE curves are used to determine the transition configurations (TC) for the reactions. Since we have used an approximate force field, ReaxFF, it is important that we assess its accuracy to the extent that we can; thus, we compare the potential energy profiles predicted by ReaxFF to the TCs.

We first focused on calculation of the average relative translational plus internal energy over all clusters; that is, $\langle (\bar{E}_{\text{rel}})_{\text{all}} + (\bar{E}_{\text{int}})_{\text{A}} + (\bar{E}_{\text{int}})_{\text{B}} \rangle$ in Eq. (20). The evolution of ensemble averages of vibrational and rotational energies for H_2 and O_2 molecules in a typical simulation at $T = 3,000$ K and $\rho = 304.85$ $\text{kg}\cdot\text{m}^{-3}$ for a mixture of 50 H_2 and 50 O_2 molecules was computed over the first 100 ps of the simulation. The time averages of these quantities are approximately equal to RT per mole (5.96 kcal/mol), as predicted by the equipartition theorem. We used Eq. (18) to find the relative translational energy of each H_2 - O_2 pair every time step until a reaction was detected and averaged over all H_2 - O_2 pairs (2,500 pairs exist in a simulation cell); the time average of this quantity gives

$\langle (\bar{E}_{\text{rel}})_{\text{all}} \rangle$; see Eq. (20). This corresponds to the analytical approach introduced by Truhlar¹³² and leads to the same result for $(\bar{E}_{\text{rel}})_{\text{all}}$. The simulation predicts 8.81 kcal/mol for the average relative translational energy of H₂-O₂ pairs, which is about $3/2RT$ per mole (8.94 kcal/mol). Using Eq. (18), the relative translational energy of each 2O₂+H₂ cluster was computed every time step until a reaction was detected and averaged over all 2O₂+H₂ clusters (61,250 clusters exist in a simulation cell); the evolution of the average relative translational energy of termolecular clusters, 2O₂+H₂, is plotted for a typical simulation is shown in Figure 4.1. The calculated $\langle (\bar{E}_{\text{rel}})_{\text{all}} \rangle$ for the termolecular cluster of 2O₂+H₂ is equal to 17.92 kcal/mol, which is about $3RT$ per mole (17.88 kcal/mol) of termolecular clusters of 2O₂+H₂ under thermal conditions. Note that Eq. (18) predicts the same results as Eq. (12) does, which confirms the reliability of the computational approach prescribed by Eq. (18). The average relative translational plus internal energy of all clusters, $\langle (\bar{E}_{\text{rel}})_{\text{all}} + (\bar{E}_{\text{int}})_{\text{A}} + (\bar{E}_{\text{int}})_{\text{B}} \rangle$, Eq. (20), is determined by temperature.

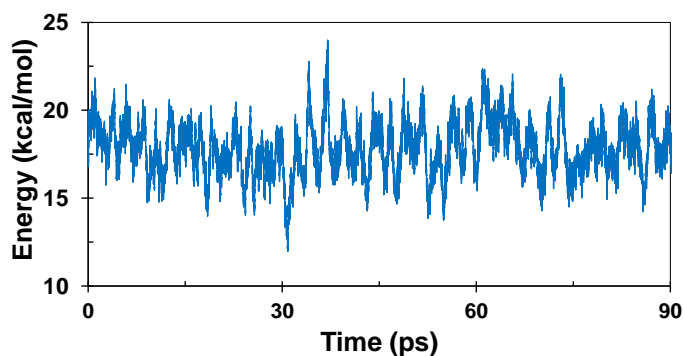


Figure 4.1: Average relative translational energy for all H₂ + 2O₂ groups as a function of time for a typical simulation. The time average of the quantity is 17.92 kcal/mol that is about $3RT$.

The RCLE for each individual reaction was calculated using Eq. (19), and the ensemble average of 30 individual reactions was used in Eq. (20) for $(\bar{E}_{\text{local}})_{\text{MD}}^{\text{NVT}}$. This gives values of Tolman's activation energy 52.9 kcal/mol and 18.9 kcal/mol for $\text{O}_2 + \text{H}_2 \rightarrow \text{H} + \text{HO}_2$ and $2\text{O}_2 + \text{H}_2 \rightarrow 2\text{HO}_2$, respectively. The predicted activation energy of $\text{O}_2 + \text{H}_2 \rightarrow \text{H} + \text{HO}_2$ can be compared to the Michael *et al.*⁵² results; they reported

$$k = 1.228 \times 10^{-18} T^{2.4328} \exp(-26926 \text{ K}/T) \text{ cm}^3 \cdot \text{molecule}^{-1} \cdot \text{s}^{-1} \quad (22)$$

for the temperature range 400 K to 2,300 K. Assuming extrapolation of Eq. (22) to 3,000 K is valid gives $E_a = 68.01$ kcal/mol, which differs with the Tolman activation energy by about 22%. The predicted Tolman activation energy value for $2\text{O}_2 + \text{H}_2 \rightarrow 2\text{HO}_2$ at 3,000 K is significantly larger than the reaction barrier height by 5.3 kcal/mol obtained by using NEB. To the best of our knowledge there is no reported value for the activation energy for $2\text{O}_2 + \text{H}_2 \rightarrow 2\text{HO}_2$.

The local energy curves of the reactants and products were calculated starting 125 fs before the time at which reaction was identified using

$$E_{\text{local}}(t) = (E_{\text{rel}} + E_{\text{int}})_t. \quad (23)$$

Panels (a) and (c) of Figure 4.2 show the local energy curves for a typical bi- and tri-molecular reaction, respectively. Each local energy curve has three regions: pre-transition, transition, and post-transition. Pre-transition is the region where time averages of local energy curves are usually constant values with local energy of the reactants being

lower than that of products. Immediately after formation of the reaction cluster the local energy curves are almost vertical; which is the transition region that includes the TC. Beyond the transition region the reactions proceed products, which we call the post-transition region. As in the pre-transition region the local energy oscillates about constant values with the local energy of the products being lower than that of the reactants. It must be noted that in the pre-transition region and prior to formation of the reaction cluster, if any reactant species collided with other species present in the box, we observed an abrupt change in local energy curves due to energy transfer. However, once the reaction cluster formed, the local energy curves remained constant; see Figure 4.3. In addition to the abrupt change caused by collisions between components of a reaction cluster with other species prior to formation of the reaction cluster, the thermostat can also perturb the local energy due to rescaling the velocities.

The local energy shown in panels (b) and (d) of Figure 4.2 (in green) for typical bi- and ter-molecular reactions, respectively, was determined by the minimum between the local energy of the reactants (blue dashed curves) and that of the products (red dashed curves) every time step beginning 125 fs prior to detection of the reaction. As panels (b) and (d) of Figure 4.2 show the RCLE is conserved during a reaction. This is in agreement with Eq. (17) that for the NVT ensemble the RCLE at the beginning of a reaction and at the end of the reaction are equal. On the other hand, the thermal energy shown in panels (b) and (d) of Figure 4.2 (in purple) predicts that the thermal energy decreases for both of the typical individual reactions. According to the individual reactions of Figure 4.2, the reaction cluster loses 41.2 kcal/mol and 2.2 kcal/mol thermal energy for the bi- and ter-molecular reactions, respectively. This means that the reaction clusters become

energetically cold after the reactions. Note that for the bimolecular reaction, LE starts deviating from its mean value at 44.4 ps (panel (b)). This rapid deviation is due to the hydrogen-atom product is highly unstable and leaves the reaction cluster immediately as it is produced, thus starts interacting with other species. We obtained the LE and TE pathways for each reaction by averaging over 30 individual LEs and TEs, respectively; see Figure 4.4.

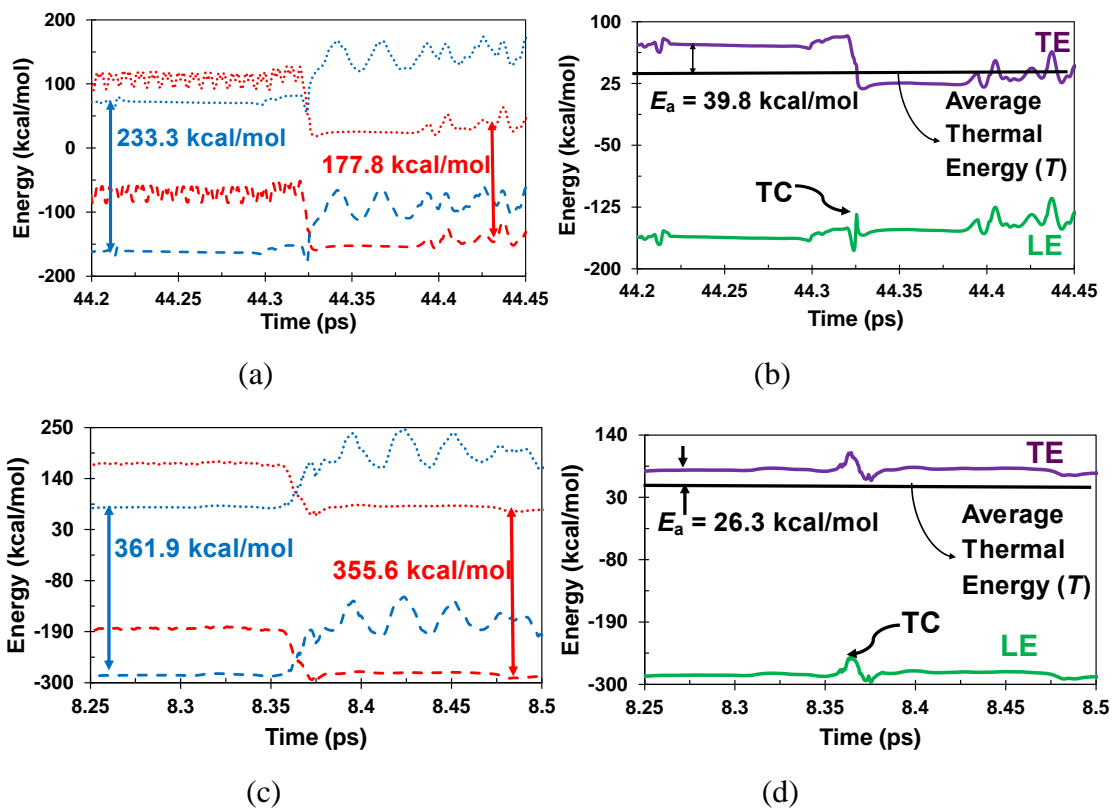


Figure 4.2: The local energy (LE) of the reactants (dashed blue curves) and products (dashed red curves), both calculated using Eq. (22) for (a) a typical $\text{H}_2 + \text{O}_2 \rightarrow \text{H} + \text{HO}_2$ reaction and (c) a typical $\text{H}_2 + 2\text{O}_2 \rightarrow 2\text{HO}_2$ reaction. The LE is the minimum of these local energy curves and plotted in green for (b) the bimolecular reaction and (d) the termolecular reaction. The transition configuration for each reaction is shown by an arrow. For each individual reaction, the thermal energy curves are shown by blue and red

dotted curves for the reactant and product arrangement of the reaction cluster, respectively. The thermal energy (TE) curves are shown in purple. The Tolman activation energy for these individual reactions is 39.8 kcal/mol and 26.3 kcal/mol for the bi- and ter-molecular reaction, respectively.

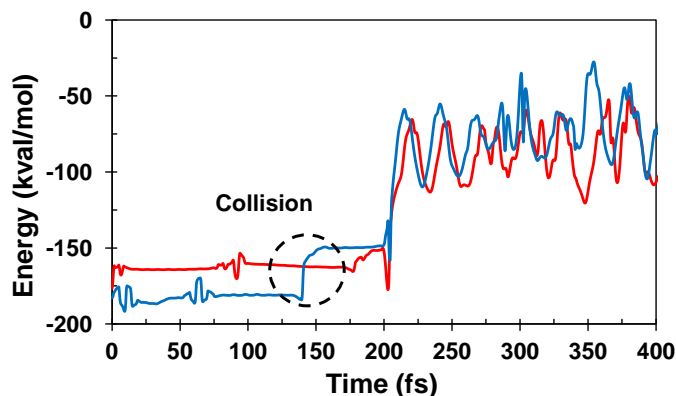


Figure 4.3: The local energy curves for the reactant arrangement of two typical bimolecular reaction cluster $\text{H}_2 + \text{O}_2 \rightarrow \text{H} + \text{HO}_2$. The time origin sets at 215 fs prior to detection of the reaction that is rupturing of the H_2 molecule. For the reaction cluster shown in red, the local energy is constant in the interval prior to the time at which reaction was detected. However, the local energy shown by the blue curve abruptly increases about 75 fs prior to breaking of the H-H bond. This abrupt change is due to a H_2 molecule colliding with a collision complex previously formed by a H_2 and an O_2 molecule. This collision occurs about 55 fs before the formation of the reaction cluster.

Each LE has a maximum located at the intersection of the local energy curves which lies in the transition region. The configuration of reaction cluster at the peak of the LE was taken as the TC for the reaction, as illustrated in Figure 4.5 for the typical reactions

of Figure 4.2. We computed TC for 30 individual reactions of each kind (30 termolecular and 30 bimolecular). Then we averaged the geometrical parameters over the individual TCs to obtain the average TC for the bi- and ter-molecular reactions. The geometrical parameters for the average TCs are listed in Table 4.1. It is important to note that while before TC the LE is determined by local energy of reactants, once a reaction passes TC the backward reaction has to be considered to get the LE. This is due to the fact that reaction proceeds along the product channel beyond TC. Thus, TC is a unique point on the LE which determines the time after which products becomes thermally more stable than reactants.

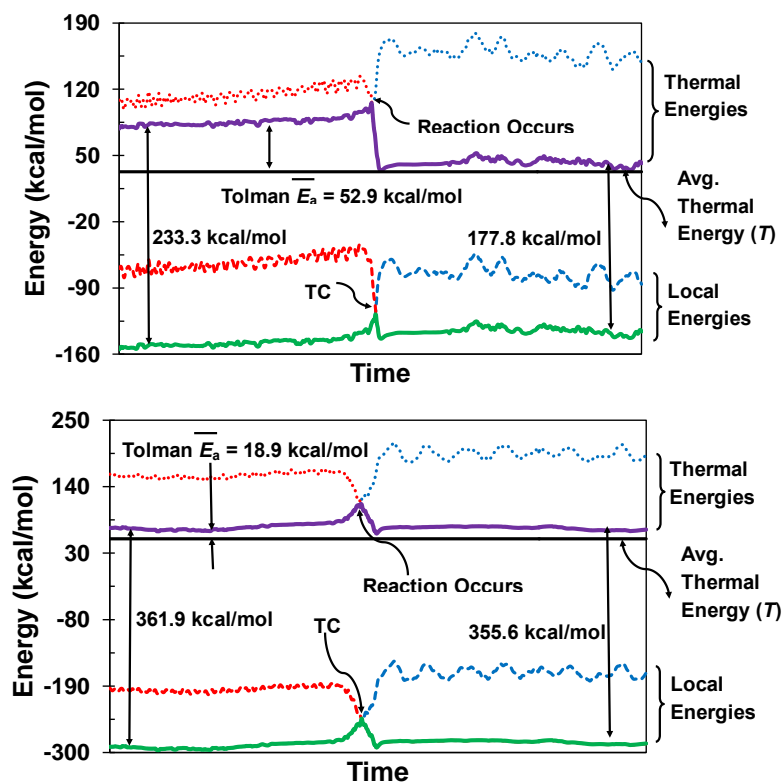


Figure 4.4: The local energy (LE) path (green curves) and the thermal energy (TE) path (purple curves) were obtained by averaging over 30 individual reaction LEs and TEs, respectively, and shown for the bimolecular (top panel) and termolecular (bottom panel) reactions. The average local energy curves are plotted for reactants (blue) and products

(red). While near the time of the reaction, the average RCLE is conserved, the bimolecular and termolecular reaction clusters lose 42.1 kcal/mol and 4.0 kcal/mol thermal energy on average, respectively. The Tolman activation energy was computed as the average of 30 individual activation energies.

The ReaxFF saddle point (geometries are given in Table 4.1 and the potential energy profile was illustrated in Figure 3.2) for the bimolecular reaction shows that for the bimolecular reaction the saddle point resembles to the products. It is also true for the TC of the bimolecular reaction. As demonstrated in Figure 4.2(a), the crossing point of two curves is at the bottom of the transition region for the reverse reaction (red curve). Unlike the bimolecular reaction which saddle point is completely on the product side, the saddle point for the termolecular reaction has an intermediate structure that is slightly leaning to the products (dashed green line in Figure 3.2). It can also be inferred by looking at Figure 4.2(c) where the TC is in the middle of the transition region for the reverse reaction (blue curve).

Table 4.1: Predicted transition configuration (TC) geometries determined by using Tolman’s approach and saddle point (SP) structures obtained using NEB method for bi- and ter-molecular reactions. The reported values are the average over an ensemble of 30 individual TC.

| | NEB | TC |
|---------------------|---------|-------------|
| Termolecular | | |
| r O'-H' | 1.04 | 1.34 ± 0.15 |
| r O-H | 1.04 | 1.43 ± 0.15 |
| r H-H' | 1.34 | 1.16 ± 0.06 |
| β_1 O-H-H' | 170.66 | |
| β_2 O-H-H' | 170.66 | |
| α O-H-H'-O' | -170.48 | |

| Bimolecular | | |
|---------------------|---------|-----------------|
| r O-H | 1.01 | 1.26 ± 0.11 |
| r H-H' | 1.58 | 1.25 ± 0.10 |
| β' O-H-H' | 144.70 | |
| α' O'-O-H-H' | -161.33 | |

^aDistances in angstroms. β_1 and β_2 are the bond angles and α is the dihedral angle for the termolecular saddle point. β' and α' are the bond and dihedral angles, respectively, for the bimolecular reaction.

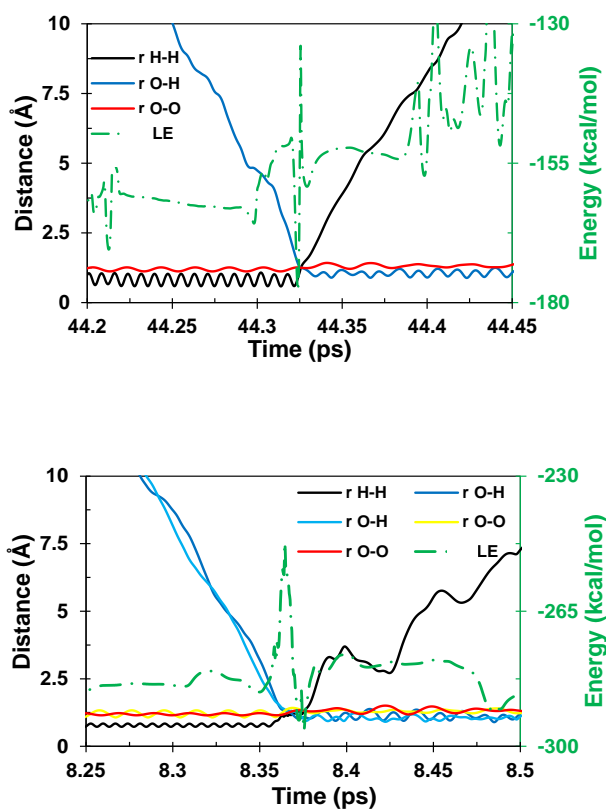


Figure 4.5: The reaction identification algorithm monitors the evolution of internuclear distances within the reaction cluster; the dashed green curve shows the local energy (LE) which maximum is associated to the energy of the presumptive TC. (a) A typical bimolecular reaction with the transition configuration (TC) geometry of r H-H = 1.22 Å, r O-H = 1.26 Å and r O-O = 1.26 Å, and (b) a typical termolecular reaction with the

TC geometry of $r_{\text{H-H}} = 1.15 \text{ \AA}$, $r_{\text{O-H}} = 1.34 \text{ \AA}$, $r_{\text{O-H}} = 1.34 \text{ \AA}$, $r_{\text{O-O}} = 1.29 \text{ \AA}$ and $r_{\text{O-O}} = 1.23 \text{ \AA}$.

4.3 MICROCANONICAL ENSEMBLE

4.3.1 COMPUTATIONAL METHODS

Using ReaxFF reactive force field, 50 simulations were performed with microcanonical ensembles, that is, fixed number of atoms (N), fixed volume (V), and fixed total energy (E)—referred to as NVE. We simulated 10 H_2O_2 molecules at the density of $\rho = 275.6 \text{ kg}\cdot\text{m}^{-3}$ in a cubic cell with periodic boundary conditions. The total energy of the simulations was set to the total energy of the equilibrated system at 2,100 K.

We first began with running an equilibration simulation. Initial configuration of reactants for each simulation was generated using PACKMOL⁸⁹ code that distributes all molecules in a box with periodic boundaries such that all non-bonding interatomic distances were at least 2.2 \AA . These initial configurations were adjusted by using the Polak-Ribiere version of the conjugate gradient algorithm for energy minimization, until either the energy, 1×10^{-4} , or the force criterion, $1 \times 10^{-6} \text{ kcal}\cdot\text{mol}^{-1} \text{ \AA}^{-1}$, was satisfied. This resulted in the H_2O_2 molecules being at the bottom of the potential well with O-H and O-O bonds equal to their equilibrium bond length; 0.970 \AA and 1.461 \AA , respectively. Atomic velocities were selected from Gaussian distributions corresponding to the input temperatures of 2,100 K. The trajectories were propagated using the velocity Verlet algorithm with time step of 0.01 fs.

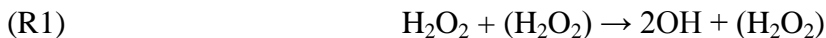
The equilibration simulations were carried out using NVT ensemble for the input temperature of 2,100 K. The equilibration in the system was checked by calculation of the average kinetic translational and kinetic internal (rotational plus vibrational) temperatures of the molecules. If a reaction was occurred during the equilibration, the simulation was abandoned. State of the equilibrated system was used as input for production of NVE simulations which were run for 2 ns.

4.3.2 ATOMIC REACTION SEQUENCE AND REACTION STREAM

We used the reaction identification algorithm previously described in Chapter 2 to detect all chemical molecular events in transition of the system from thermally equilibrated reactants to thermally equilibrated products in thermal dissociation of H₂O₂. Note that in the present study the most thermodynamically (from point of view of free energies) stable product is a mixture of 10 H₂O and 5 O₂; that is the overall reaction is



The simulations predict two initiation reaction mechanisms for thermal dissociation of H₂O₂ as



with contribution of 62% and 38% to the initial radicals production, respectively. A complete list of all elementary reactions observed in the simulations is reported in Appendix I.

We define an *atomic species sequence* (ASS) for an atom as a sequence of species that connects thermally equilibrated reactants to thermally equilibrated products. For each simulation, we divided the time interval between time of occurrence of the initial reaction and the time at which the final products became thermally equilibrated into 10 regular sub-intervals. At the end of each sub-interval composition of the system was determined. The first composition determination was made immediately after the initial reaction was completed and its products were identifiable. The last determination was made when the final products became thermally equilibrated. We obtained the ASS for each H atom and each O atom individually. A complete set of ASSs for all H and O atoms are illustrated in panels (a) and (b) of Figure 4.6, respectively. Removing the less frequent ASSs with occurrence probability < 1%, we obtained the dominant ASSs that are shown in Figure 4.7. The simulations predict that the less frequent ASSs contribute by 20% to transition of the system from thermally equilibrated reactants to thermally equilibrated products in thermal dissociation of H₂O₂. This significant contribution indicates that rare ASSs which result from less probable elementary reactions can be treated as fluctuations and are deserved to be understood profoundly using methods like *kinetic Monte Carlo*.¹⁵²

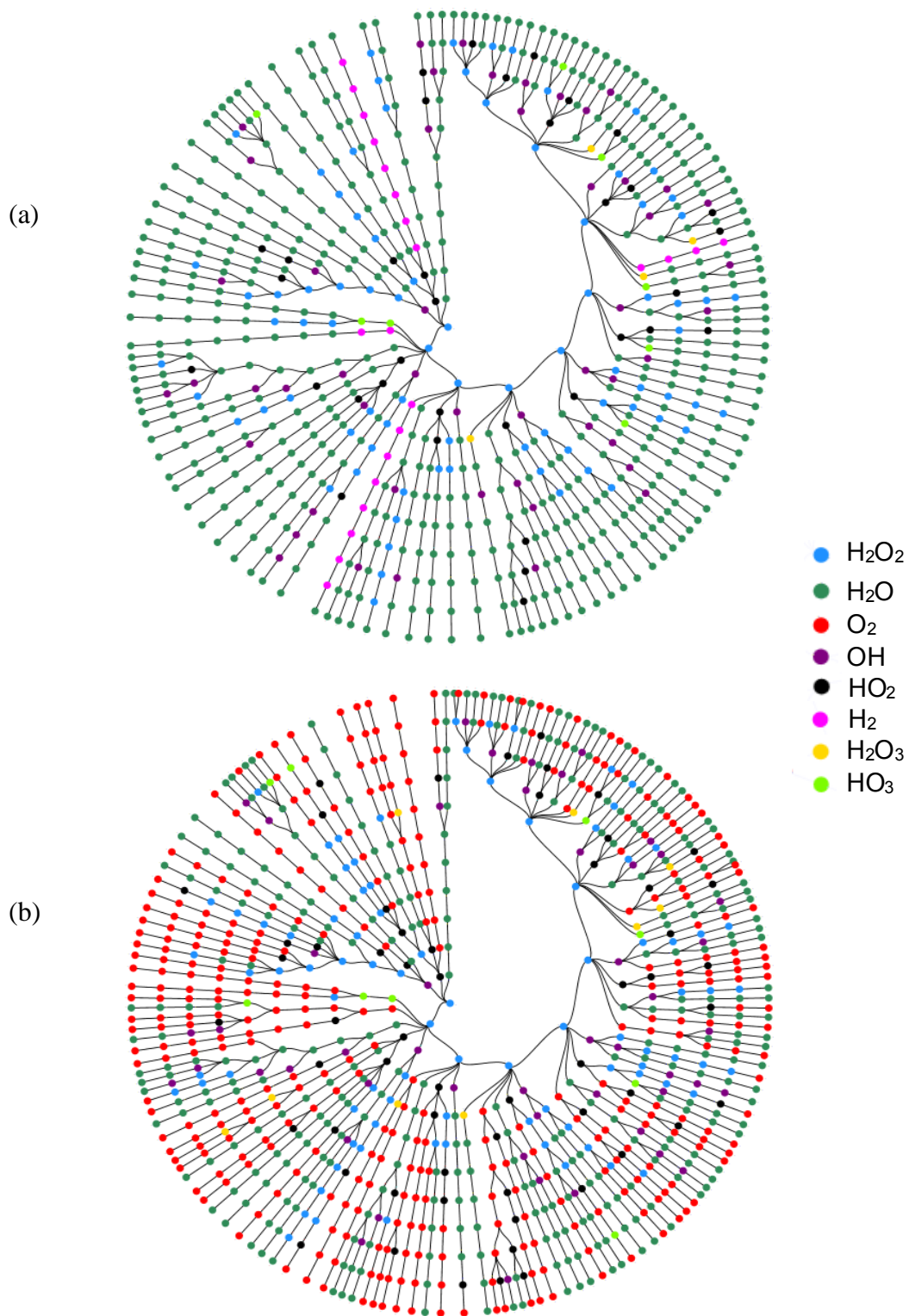


Figure 4.6: (a) All atomic species sequences (ASSs) found for (a) H atoms and (b) O atoms from analysis of 50 NVE simulations of 10 H_2O_2 molecules equilibrated at 2,100 K and $275.6 \text{ kg}\cdot\text{m}^{-3}$

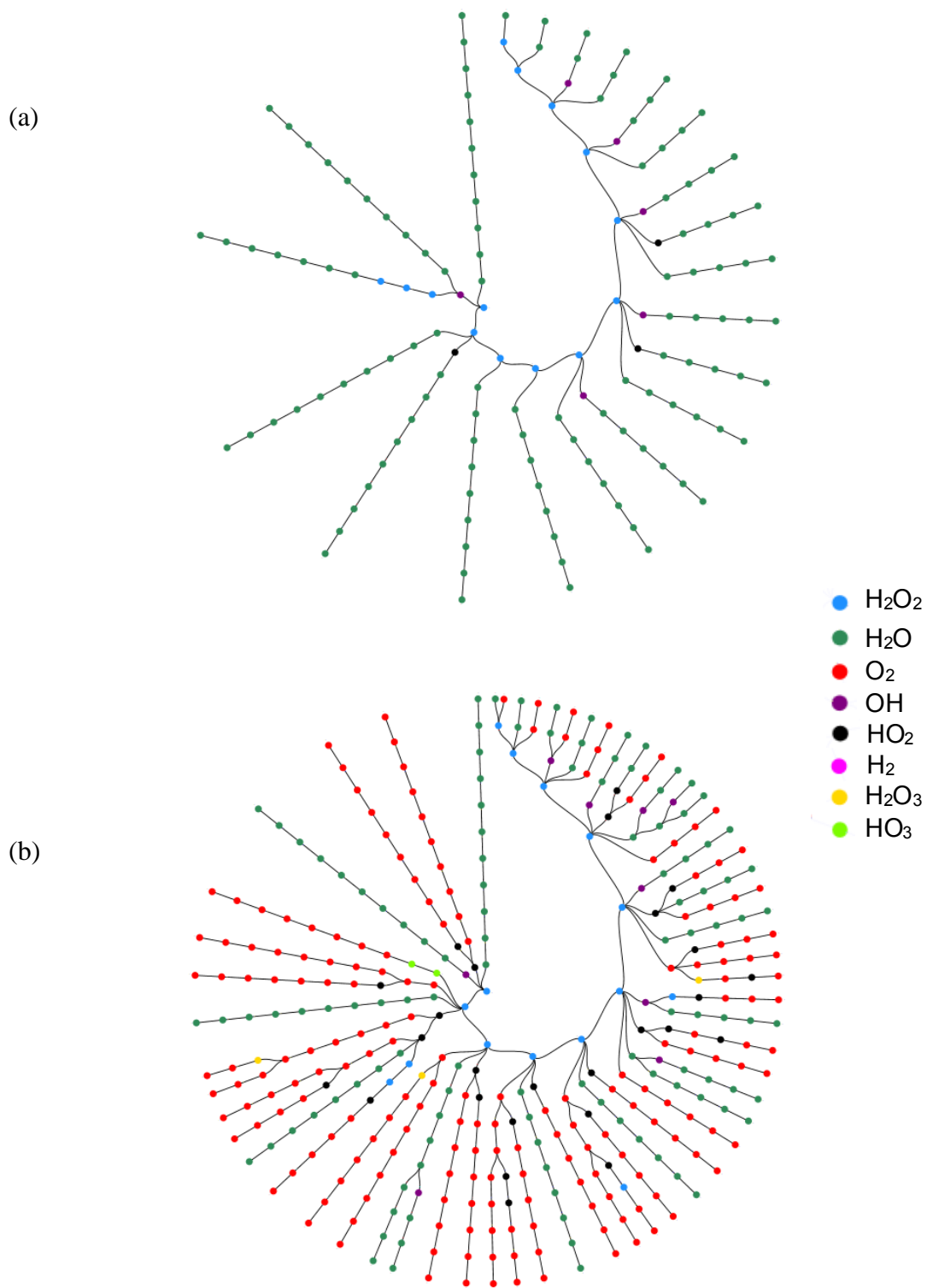


Figure 4.7: The dominant atomic species sequences (ASSs) obtained by removing less frequent ASSs with occurrence probability $< 1\%$ from Figure 4.6 for (a) H atoms and (b) O atoms.

We define the *atomic reaction stream* (ARS) for all atoms of same kind (that is, all H atoms or all O atoms) as a complete set of sequences of elementary reactions which connect two different chemical species among those appeared in the overall reaction equation (R), that is H_2O , H_2O_2 , and O_2 . For hydrogen atoms, for instance, ARS is the set of four groups of reaction sequences connect H_2O_2 to H_2O , H_2O_2 to H_2O_2 , H_2O to H_2O_2 , and H_2O to H_2O . Note that we also considered the situation where initial and final species in the sequences were not thermally equilibrated. For each group in an ARS set, less frequent sequences with occurrence probability $< 1\%$ were removed to obtain the dominant subset of the ARS. The dominant subset of the ARS for H atoms is listed in Table 4.2 and illustrated in Figure 4.8. The simulations predict that 85% of H atoms are involved in reaction sequences listed Table 4.2 in transition of the system from thermally equilibrated reactants to thermally equilibrated products.

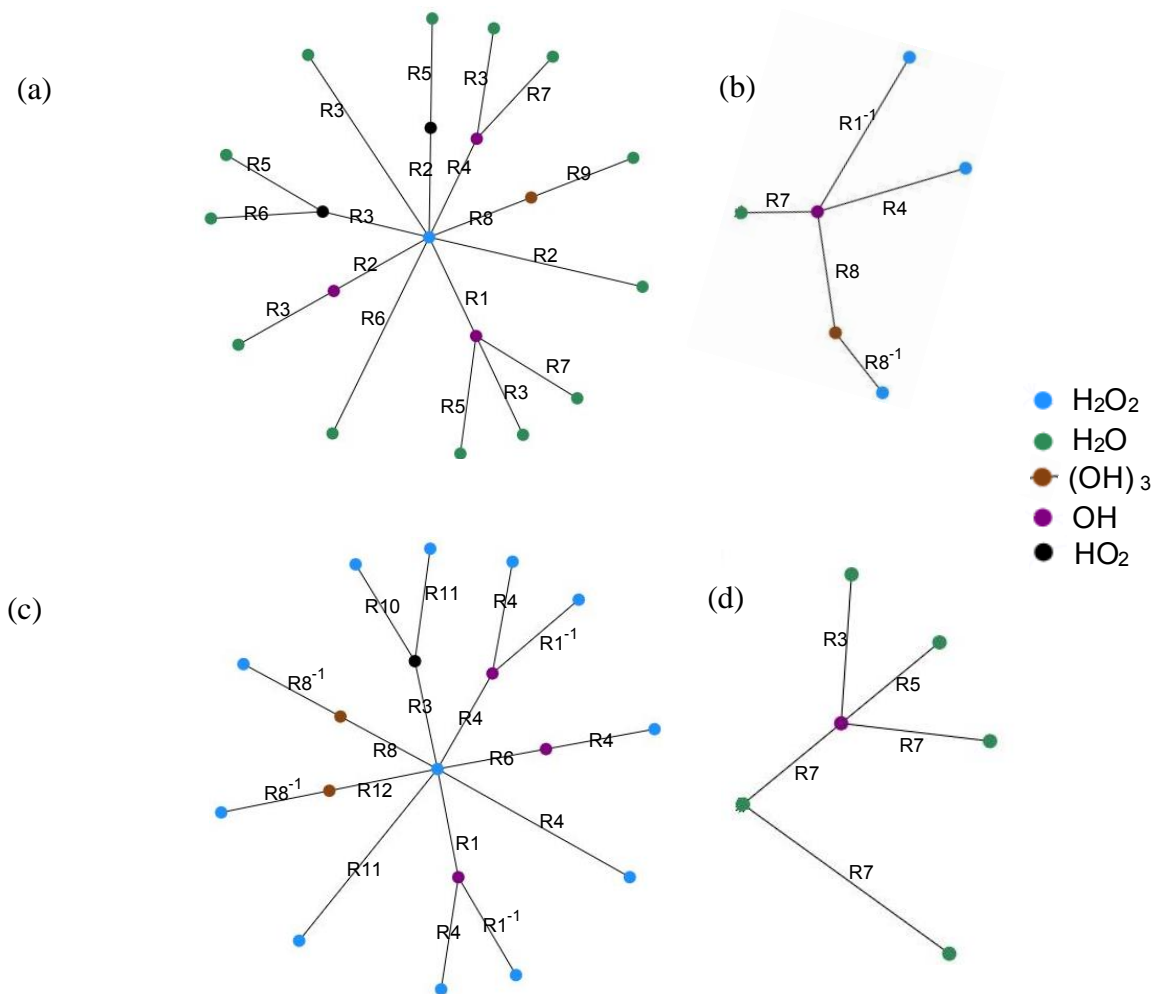


Figure 4.8: The dominant subset of atomic reaction stream (ARS) for H atoms obtained from analysis of 50 NVE simulations of 10 H₂O₂ molecules equilibrated at 2,100 K and 275.6 kg·m⁻³. Dominant reaction sequences which connect (a) a H₂O₂ molecule to a H₂O molecule, (b) a H₂O molecule to a H₂O₂ molecule, (c) a H₂O₂ molecule to a H₂O₂ molecule, and (d) a H₂O molecule to a H₂O molecule.

Table 4.2: The dominant subset of ARS for H atoms.¹

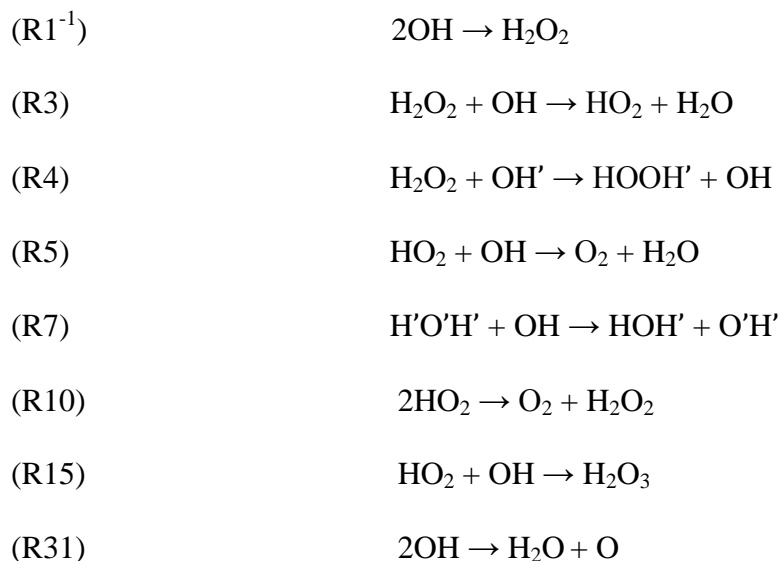
| | Reaction Sequence | Probability |
|---|------------------------|-------------|
| H₂O₂ to H₂O | | |
| | R3 | 27% |
| | R1-R7 | 13% |
| | R1-R3 | 11% |
| | R6 | 6% |
| | R3-R5 | 5% |
| | R2 | 4% |
| | R4-R3 | 3% |
| | R3-R6 | 3% |
| | R1-R5 | 2% |
| | R4-R14 | 2% |
| | R8-R9 | 2% |
| | R2-R3 | 1% |
| | R2-R5 | 1% |
| H₂O to H₂O₂ | | |
| | R7-R1 ⁻¹ | 52% |
| | R7-R4 | 26% |
| | R7-R8-R8 ⁻¹ | 12% |

| <i>Continued</i> | Reaction Sequence | Probability |
|---|--------------------------|--------------------|
| H₂O₂ to H₂O₂ | | |
| | R4 | 33% |
| | R3-R10 | 13% |
| | R1-R4 | 9% |
| | R8-R8 ⁻¹ | 7% |
| | R11 | 6% |
| | R6-R4 | 5% |
| | R4-R4 | 4% |
| | R12-R8 ⁻¹ | 3% |
| | R3-R11 | 2% |
| | R1-R1 ⁻¹ | 2% |
| | R4-R1 ⁻¹ | 2% |
| H₂O to H₂O | | |
| | R7 | 54% |
| | R7-R7 | 27% |
| | R7-R5 | 8% |
| | R7-R3 | 5% |

¹A complete list of identified reactions is available in Appendix I.

4.3.3 NEB CALCULATIONS

In the previous section, we have determined the dominant subset of the ARS for hydrogen atoms in the thermal dissociation of H₂O₂. As inferred from Table 4.2, the most frequent reaction sequences include reactions involving highly unstable radicals such as OH and HO₂. These reactions are



Since these reactions significantly contribute in the dominant subset of the ARS, it is important to know how accurate ReaxFF force field predicts the potential energy profile for them. Therefore, we performed nudged elastic band (NEB) calculations as implemented in LAMMPS 2014 to characterize the potential energy profile for these reactions as predicted by ReaxFF. A minimum number of 56 replicas distributed equidistantly along the reaction pathway were selected from actual simulations to perform the NEB studies. We changed the force constants within $1.0 \times 10^{-5} E_h \cdot a_0^{-2}$ to $1.0 \times 10^{-1} E_h \cdot a_0^{-2}$ interval until the force criteria of $1.0 \times 10^{-5} E_h \cdot a_0$ was met for the saddle points. The potential energy profiles for these reactions are shown in Figure 4.9 which reveals that all of these reactions proceed *via* formation of a reactant complex in the entry channel.

Ginovska *et al.*¹⁵³ performed *ab initio* calculations using DFT MPW1K/6-31+G** level of theory to characterize the potential energy profile for reaction (R3). Their calculations reveal that a reactant complex exists in the entry channel of the reaction

which is 6.1 kcal/mol lower in energy than the separated reactants. They predicted two saddle points for reaction (R3) which are 0.9 kcal/mol and 1.5 kcal/mol above the separated reactants. Comparing with Ginovska *et al.* results, we conclude that while ReaxFF predicts the energy of the reactant complex nearly accurately (ReaxFF prediction is only 0.57 kcal/mol lower than that of predicted by Ginovska *et al.*¹⁵³ using DFT MPW1K/6-31+G** level of theory), it tremendously fails to predict the energy of the saddle points for reaction (R3); ReaxFF prediction for the saddle point of reaction (R3) is 6.97 kcal/mol below the lowest energy saddle point predicted by Ginovska *et al.*

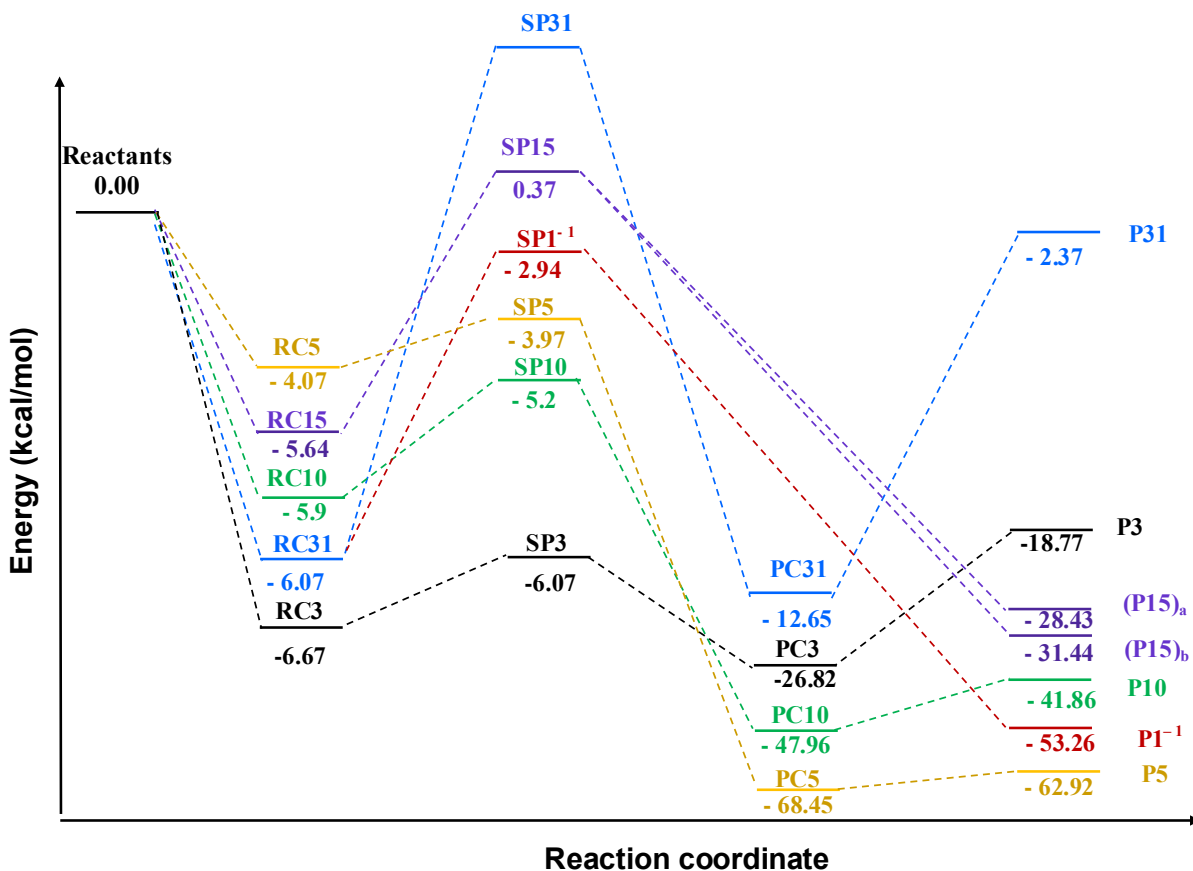


Figure 4.9: ReaxFF prediction for the potential energy profile of the dominant reactions in atomic reaction stream (ARS) of thermal dissociation of H₂O₂. Reactant complex

(RC), saddle point (SP), and product complex (PC) are energetically characterized for each reaction. Attempts to characterize the potential energy profile for reactions (R4) and (R7) failed.

Gonzalez *et al.*^{154,155} carried out *ab initio* calculations to characterize the potential energy profile for reaction (R5) on the triplet¹⁵⁵ and singlet¹⁵⁴ potential energy surfaces. Using MP4/6-31G** level of theory, they reported the barrier heights of 48.05 kcal/mol and 7.59 kcal/mol on the singlet and triplet surfaces, respectively, relative to the reactant complex formed in the entry channel. Their electronic structure calculations reveal that reaction (R5) predominantly proceeds on the triplet potential energy surface except at temperatures higher than 2,500 K where the reaction path on the singlet surface becomes competitive. Comparing with the results reported by Gonzalez *et al.*, it is revealed that ReaxFF does not accurately predict the potential energy profile which might be due to the fact that ReaxFF surface is a spinless surface.

It must be noted that in the present study, we used ReaxFF merely as a tool to develop methods to glean details of the chemistry from CMD simulations; the accuracy is not a key to our purpose.

4.3.4 APPLICATION OF GENERALIZED TOLMAN ACTIVATION ENERGY TO NON-THERMAL REACTIONS

Earlier in this Chapter, we presented the generalized interpretation of the Tolman activation energy and applied it to the molecular dynamics (MD) simulations of reactions in bulk gases under thermal conditions. Here, we use the interpretation to treat non-

thermal reactions; for example, in reactions occurring in bulk MD simulations of the NVE ensemble.

We defined the activation energy for an individual reaction $A + B \rightarrow \text{Products}$ occurring in MD simulations, as the average local energy (internal plus relative translational) of the reactant pair that react $\langle E_{\text{local}} \rangle_{\text{react}}$ minus the average energy of all clusters of reactants; that is

$$(E_a)_{\text{individual}} = \langle E_{\text{local}} \rangle_{\text{react}} - \bar{E}_{\text{all}}, \quad (24)$$

where the $\langle E_{\text{local}} \rangle_{\text{react}}$ was computed by time averaging sum of the internal and relative translational energies of reactants that reacts. The time average was computed over a limited time interval prior to detection of the reaction during which the composition of the system remained unchanged. This time interval varied from one reaction to another. For the \bar{E}_{all} , we assumed thermal conditions, that is, the average relative translational energy and the average internal energies were set by T according to equipartitioning of the energy.

However, application of Eq. (24) to non-thermal reactions requires properly treatment of \bar{E}_{all} . Since for microcanonical ensemble temperature is not a fundamental variable, one cannot assume equipartitioning of the energy in its conventional form, which states the contribution of each degree of freedom to the total kinetic energy is $\frac{1}{2} RT$ per mol. Recently, Uline *et al.*¹⁵⁶ generalized the equipartition theorem to microcanonical ensemble showing that for NVE ensembles with small number of atoms, energy of

various degrees of freedom is proportional to a more fundamental bulk property than the temperature which is the time average total kinetic energy of the system; $\langle KE_{\text{tot}} \rangle$.

It is trivial that the $\langle KE_{\text{tot}} \rangle$ for a number of N particles is equal to the sum of the average kinetic energy of each particle, that is

$$\langle KE_{\text{tot}} \rangle = \sum_{i=1}^N \frac{\langle \mathbf{p}_i^2 \rangle}{2m_i}, \quad (25)$$

where \mathbf{p}_i is the momentum vector of the i^{th} particle. Uline *et al.*¹⁵⁶ showed that the average total kinetic energy acts as an energy bath for each particle and the average energy of each particle is expressed as

$$\frac{\langle \mathbf{p}_i^2 \rangle}{2m_i} = \frac{M_{\text{tot}} - m_i}{M_{\text{tot}}(N-1)} \langle KE_{\text{tot}} \rangle. \quad (26)$$

Although Uline *et al.* only considered translational degrees of freedom to generalize the equipartition theorem, their approach can be extended to internal degrees of freedom as we do it in the current study. Here, we made use of the GTEa jointly with a more generalized version of the equipartition theorem than that of introduced by Uline *et al.* to compute the activation energy for the secondary reactions of (R3) predominantly observed in ARS of thermal dissociation of H_2O_2 .

4.3.5 THEORETICAL METHODS AND RESULTS

There are $N = 40$ atoms in simulation cells which form N_t number of molecules (number of molecules varies in course of the overall reaction). It is important to note that the generality of Eq. (25) is not violated by assuming particles as molecules with the internal degrees of freedom. Subtracting sum of the average molecular center-of-mass translational energy from both sides of Eq. (25), we have for the time average total internal (rotational plus kinetic vibrational) kinetic energy

$$\langle KE_{\text{tot,int}} \rangle = \sum_{i=1}^{N=40} \frac{\langle \mathbf{p}_{i,\text{red}}^2 \rangle}{2m_i} \quad \text{with } i = \text{H or O} \quad (27)$$

where $\mathbf{p}_{i,\text{red}}$ is the internal (rotational plus kinetic vibrational) momentum of the i^{th} atom.

Rewriting Eq. (26) for the average total internal kinetic energy, we have

$$\frac{\langle \mathbf{p}_{i,\text{red}}^2 \rangle}{2m_i} = \frac{M_{\text{tot}} - m_i}{M_{\text{tot}}(N-1)} \langle KE_{\text{tot,int}} \rangle \quad \text{with } i = \text{H or O, and } N = 40 \quad (28)$$

for the average internal kinetic energy of each atom in the system. Equation (28) shows that while all similar atoms (all H atoms or all O atoms) contributes an identical amount to the total internal kinetic energy, different atoms do not contribute equally to the total internal kinetic energy due to the difference in masses. We can also write down a similar equation to Eq. (25) for the average total translational energy as

$$\langle KE_{\text{tot,trans}} \rangle = \sum_{i=1}^{N_t} \frac{\langle \mathbf{p}_{i,\text{CoM}}^2 \rangle}{2m_i}, \quad (29)$$

where the sum is over the total number of molecules, N_t , and $\mathbf{p}_{i,\text{CoM}}$ is the momentum of the center-of-mass of the i^{th} molecule. Therefore, the average translational energy of the i^{th} molecule is

$$\frac{\langle \mathbf{p}_{i,\text{CoM}}^2 \rangle}{2m_i} = \frac{M_{\text{tot}} - m_i}{M_{\text{tot}}(N_t - 1)} \langle KE_{\text{tot,trans}} \rangle . \quad (30)$$

Equation (30) implies that the contribution of each molecule to the total translational energy is not the same for all molecules but depends on a factor related to the mass of the molecule. More specifically, the heavier molecules contribute less than the lighter molecules.

We identified a number of 40 distinct occurrences of (R3) in seven NVE simulations. To get the activation energy for each individual reaction, we needed to compute the local energy of OH \cdots H₂O₂ reaction clusters. For each reaction cluster, we separately obtained the center-of-mass velocity of the OH and H₂O₂ involved in the reaction cluster from the LAMMPS output file beginning 125 fs prior to detection of a reaction. This gives the molecular translational energy for each species in the reaction cluster. Then, we subtracted the obtained molecular translational energies from the total kinetic energy of the reaction cluster which gives the total internal kinetic energy of the cluster. Then, we computed the relative translational energy for the cluster as sum of the molecular translational energies minus the translational energy of the center-of-mass of the OH \cdots H₂O₂ cluster. Then, the bonding potential energy for the involved OH and H₂O₂

was obtained directly from ReaxFF by running independent simulations with only one species in the box at each time (to avoid any intermolecular interaction). We read the potential energy predicted by ReaxFF for the geometry of reacting OH and H₂O₂. The geometries to run these independent simulations were taken from the LAMMPS output file beginning 125 fs prior to detection of the reaction. Finally, the average local energy for an OH···H₂O₂ reaction cluster, that is, $\langle E_{\text{local}} \rangle_{\text{react}}$ in Eq. (24) was computed as the time average (125 fs time interval prior to detection of the reaction) of sum of the relative translational energy, internal kinetic energy, and bonding potential energy of the cluster.

We used Eqs. (28) and (30) for the time interval between two sequential chemical events happening in the cell (with the second one being reaction (R3)) to compute the \bar{E}_{all} at the time of each individual reaction. The total kinetic energy of the system was computed using Eq. (25) from the LAMMPS output file. Then, we computed the center-of-mass velocity every 0.5 fs for each molecule to get the molecular translational energy. The total translational energy was computed by adding all molecular translational energies and averaged over the time interval between two sequential reactions to get the average total translational energy. The average relative translational energy of a typical OH···H₂O₂ cluster under the energy condition of the an individual reaction was computed as the average translational energy of a typical OH radical plus the average translational energy of a typical H₂O₂ molecule minus the average translational energy of the center-of-mass of the OH···H₂O₂ cluster; all three quantities were calculated using Eq. (30); that is

$$\begin{aligned}
\langle E_{\text{rel}} \rangle &= \left\{ \frac{M_{\text{tot}} - m_{\text{OH}}}{M_{\text{tot}}(N_{\text{t}} - 1)} + \frac{M_{\text{tot}} - m_{\text{H}_2\text{O}_2}}{M_{\text{tot}}(N_{\text{t}} - 1)} - \frac{M_{\text{tot}} - m_{\text{OH}\cdots\text{H}_2\text{O}_2}}{M_{\text{tot}}(N_{\text{t}} - 1)} \right\} \langle KE_{\text{tot,trans}} \rangle \\
&= \frac{1}{(N_{\text{t}} - 1)} \langle KE_{\text{tot,trans}} \rangle.
\end{aligned} \tag{31}$$

Note that since composition of the system was unchanged between two sequential reactions, N_{t} was fixed in Eq. (31) for each individual reaction. Equation (31) shows that the average relative translational energy for a typical bimolecular cluster is proportional to the average total translational energy regardless of the cluster mass. A similar approach can be applied to clusters with higher molecularity.

According to Eq. (28), the average contributions of hydrogen and oxygen atoms to the total internal kinetic energy are

$$\langle E_{\text{int,H}} \rangle = \frac{M_{\text{tot}} - m_{\text{H}}}{39M_{\text{tot}}} \langle KE_{\text{tot,int}} \rangle, \tag{32}$$

$$\langle E_{\text{int,O}} \rangle = \frac{M_{\text{tot}} - m_{\text{O}}}{39M_{\text{tot}}} \langle KE_{\text{tot,int}} \rangle. \tag{33}$$

Therefore, the average internal kinetic energy of a cluster of $\text{OH}\cdots\text{H}_2\text{O}_2$ for the time interval between two sequential chemical events is

$$\langle E_{\text{int,H}_2\text{O}_2} \rangle = 3 \left\{ \frac{M_{\text{tot}} - m_{\text{H}}}{39M_{\text{tot}}} + \frac{M_{\text{tot}} - m_{\text{O}}}{39M_{\text{tot}}} \right\} \langle KE_{\text{tot,int}} \rangle \tag{34}$$

where the factor of 3 accounts for the fact that there are three O and three H atoms in each OH \cdots H₂O₂ cluster. The average total internal kinetic energy appeared in Eqs. (32)–(34) was computed by subtracting the average total translational energy from the average total kinetic energy (computed using Eq. (25)).

Finally, the total bonding potential energy, at each time step, was computed by adding up the ReaxFF predictions for the potential energy of each species. We placed each species in an isolated simulation box and read its potential energy predicted by ReaxFF. The total bonding potential energy was averaged over the time interval between two sequential chemical events to get the average value at the moment of an individual reaction (R3). The total number of vibrational degrees of freedom was set by the composition of the system which is known in the time between two reactions. We assumed that the average total bonding potential energy is equally partitioned among all vibrational degrees of freedom, that is, all vibrational degrees of freedom on average contributes equally in amount of $\langle PE_{\text{vib}} \rangle$. Therefore, the average bonding potential energy of a typical OH \cdots H₂O₂ pair with four vibrational degrees of freedom is $4\langle PE_{\text{vib}} \rangle$.

Therefore, the \bar{E}_{all} for all OH \cdots H₂O₂ pairs at the time of each individual reaction was computed as the time average (over the time interval between two reactions) of sum of the average relative translational energy as computed by Eq. (31), average internal kinetic energy as computed by Eq. (34), and average potential vibrational energy of a typical OH \cdots H₂O₂ cluster; that is $\langle E_{\text{OH}\cdots\text{H}_2\text{O}_2} \rangle$. Essentially, we made the ergodic assumption that the time average is equal to the ensemble average; thus, Eq. (24) can be rewritten as

$$(E_a)_{\text{individual}} = \langle E_{\text{local}} \rangle_{\text{react}} - \langle E_{\text{OH} \cdots \text{H}_2\text{O}_2} \rangle \quad (35)$$

We computed the activation energy for 40 individual reactions of (R3), $\text{H}_2\text{O}_2 + \text{OH} \rightarrow \text{HO}_2 + \text{H}_2\text{O}$, occurring in the non-equilibrium region of the NVE simulations using Eq. (35). Figure 4.10 shows the activation energy of each individual reaction in course of the simulation. Note that the zero of time was taken to be the time of the initial reaction. We observed negative activation energy for some of the individual reactions which is interpreted in Tolman's sense as reactions between non-thermal (cold) species with the energy lower than the average. These reactions involve highly unstable radicals (OH in this case). However, the average over 40 individual activation energies reveals that the activation energy for reaction (R3) is on average $\bar{E}_a = 0.62$ kcal/mol which indicates that ReaxFF predicts that reaction (R3) in general is barrierless under the thermodynamic conditions of this study. However, each individual reaction can have either negative or positive activation energy depending on the energetics of the reaction cluster.

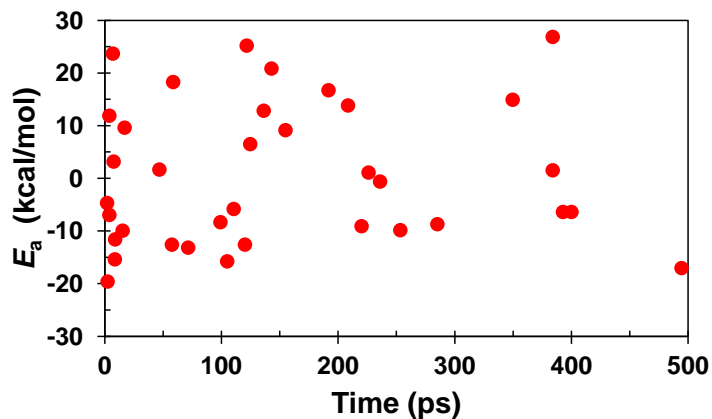


Figure 4.10: The Tolman activation energy for 40 individual secondary reactions of $\text{H}_2\text{O}_2 + \text{OH} \rightarrow \text{HO}_2 + \text{H}_2\text{O}$ in the simulation of the thermal dissociation of H_2O_2 .

5. CONCLUSIONS

In this research, we used ReaxFF force field as a tool to perform classical molecular dynamics (CMD) simulations to gain insight into hydrogen combustion. We developed a reaction identification algorithm which can be used along CMD simulations to detect every elementary molecular event such as reactions, complex formations, and complex dissociations. The simulations showed that even the early chemistry of hydrogen combustion that is a relatively simple process has not been understood well. The CMD simulations showed that the termolecular reaction $2\text{O}_2 + \text{H}_2 \rightarrow 2\text{HO}_2$ plays an important role in production of initial radicals at elevated density and low temperature. This is in contradiction with the mainstream thought in the combustion community that the bimolecular reaction $\text{O}_2 + \text{H}_2 \rightarrow \text{H} + \text{HO}_2$ is the initial reaction in hydrogen combustion.

As electronic structure calculations predicted, barrier height to the termolecular reaction $2\text{O}_2 + \text{H}_2 \rightarrow 2\text{HO}_2$ is lower (~ 9 kcal/mol) than that of the bimolecular reaction. This finding indicates that many of the currently existing reduced mechanisms and kinetic models which are widely used to describe the chemistry of hydrogen combustion are indeed inaccurate. We believe one cannot accurately describe the complexity of hydrogen combustion, unless by developing models based on atomic level simulations. As quantum dynamics is computationally very expensive, CMD simulation is the only practical approach that can be used to explore dynamics of hydrogen combustion.

One area that should be taken seriously by the combustion community is development of more accurate force fields. The only present force field, ReaxFF, is not reliable and indeed cannot be used to accurately describe and/or predict the chemistry—as we showed ReaxFF tremendously failed at predicting the barrier height for the termolecular reaction.

We need better reactive force fields which can handle the spin-spin interactions as well as the complexity of changing electronic structures during the course of combustion.

In this context, the community still lacks methods to glean details of the chemistry such as activation energies and transition structures from CMD simulations. As a starting point, we developed a computational method based on the Tolman interpretation of activation energy to extract activation energies and transition structures for various reactions in course of simulations. This is just the start point which yet needs to be studied.

6. APPENDIX I

List of the reactions observed in 50 NVE simulations of thermal dissociation of 10 H₂O₂ molecules at 2,100 K and $\rho = 275.6 \text{ kg}\cdot\text{m}^{-3}$. The red color is used for those reactions which backwards were also observed in simulations.

| | |
|-----|--|
| R1 | $\text{H}_2\text{O}_2 \rightarrow 2\text{OH}$ |
| R2 | $2\text{H}_2\text{O}_2 \rightarrow \text{H}_2\text{O} + \text{HO}_2 + \text{OH}$ |
| R3 | $\text{H}_2\text{O}_2 + \text{OH} \rightarrow \text{H}_2\text{O} + \text{HO}_2$ |
| R4 | $\text{H}_2\text{O}_2 + \text{OH} \rightarrow \text{H}_2\text{O}_2 + \text{OH}$ |
| R5 | $\text{HO}_2 + \text{OH} \rightarrow \text{H}_2\text{O} + \text{O}_2$ |
| R6 | $\text{H}_2\text{O}_2 + \text{HO}_2 \rightarrow \text{H}_2\text{O} + \text{O}_2 + \text{OH}$ |
| R7 | $\text{H}_2\text{O} + \text{OH} \rightarrow \text{H}_2\text{O} + \text{OH}$ |
| R8 | $\text{OH} + \text{H}_2\text{O}_2 \rightarrow (\text{OH})_3$ |
| R9 | $(\text{OH})_3 \rightarrow \text{H}_2\text{O} + \text{HO}_2$ |
| R10 | $2\text{HO}_2 \rightarrow \text{H}_2\text{O}_2 + \text{O}_2$ |
| R11 | $\text{HO}_2 + \text{H}_2\text{O}_2 \rightarrow \text{H}_2\text{O}_2 + \text{HO}_2$ |
| R12 | $2\text{H}_2\text{O}_2 \rightarrow (\text{OH})_3 + \text{OH}$ |
| R13 | $\text{HO}_2 + \text{O}_2 \rightarrow \text{HO}_2 + \text{O}_2$ |
| R14 | $\text{HO}_2 \rightarrow \text{H} + \text{O}_2$ |
| R15 | $\text{HO}_2 + \text{OH} \rightarrow \text{H}_2\text{O}_3$ |
| R16 | $\text{OH} + \text{O}_2 \rightarrow \text{HO}_3$ |
| R17 | $\text{H}_2\text{O}_2 + \text{HO}_2 \rightarrow \text{H}_2\text{O}_3 + \text{OH}$ |
| R18 | $\text{H}_2\text{O}_3 + \text{OH} \rightarrow \text{HO}_2 + \text{H}_2\text{O}_2$ |
| R19 | $\text{HO}_2 + \text{OH} \rightarrow \text{HO}_2 + \text{OH}$ |
| R20 | $\text{O}_2 + \text{H}_2\text{O}_2 \rightarrow \text{HO}_3 + \text{OH}$ |
| R21 | $\text{H}_2\text{O}_3 + \text{HO}_2 \rightarrow \text{H}_2\text{O}_3 + \text{HO}_2$ |
| R22 | $\text{H}_2\text{O}_3 + \text{OH} \rightarrow \text{H}_2\text{O} + \text{HO}_3$ |
| R23 | $\text{HO}_3 + \text{OH} \rightarrow \text{HO}_3 + \text{OH}$ |
| R24 | $\text{HO}_3 + \text{H}_2 \rightarrow (\text{OH})_3$ |
| R25 | $(\text{OH})_3 + \text{OH} \rightarrow \text{H}_2\text{O}_3 + \text{H}_2\text{O}$ |
| R26 | $\text{H} + 2\text{H}_2\text{O}_2 \rightarrow \text{H}_2\text{O} + (\text{OH})_3$ |
| R27 | $\text{H}_2 + \text{OH} \rightarrow \text{H}_2\text{O} + \text{H}$ |
| R28 | $\text{H}_2\text{O} + \text{HO}_2 \rightarrow \text{H} + \text{O}_2 + \text{H}_2\text{O}$ |
| R29 | $\text{H} + \text{H}_2\text{O} \rightarrow \text{H} + \text{H}_2\text{O}$ |
| R30 | $\text{H} + \text{HO}_2 \rightarrow 2\text{OH}$ |
| R31 | $2\text{OH} \rightarrow \text{H}_2\text{O} + \text{O}$ |
| R32 | $\text{H}_2\text{O}_2 + \text{HO}_2 \rightarrow \text{H}_2 + \text{O}_2 + \text{HO}_2$ |
| R33 | $\text{H}_2\text{O}_2 + \text{HO}_2 \rightarrow \text{H}_3\text{O}_4$ |
| R34 | $\text{HO}_3 + \text{HO}_2 \rightarrow \text{H}_2\text{O} + 2\text{O}_2$ |
| R35 | $2\text{HO}_2 \rightarrow 2\text{OH} + \text{O}_2$ |

| | |
|-----|--|
| R36 | $\text{H} + \text{HO}_3 \rightarrow \text{H}_2\text{O}_3$ |
| R37 | $\text{H} + \text{OH} + \text{H}_2\text{O} \rightarrow 2 \text{H}_2\text{O}$ |
| R38 | $(\text{OH})_3 + \text{H}_2\text{O}_2 \rightarrow \text{H}_2\text{O} + \text{HO}_2 + \text{H}_2\text{O}_2$ |
| R39 | $\text{H}_2 + \text{OH} \rightarrow \text{H}_3\text{O}$ |
| R40 | $\text{H} + \text{H}_2\text{O} \rightarrow \text{H}_3\text{O}$ |
| R41 | $\text{H} + \text{H}_2\text{O}_2 \rightarrow \text{H}_2\text{O} + \text{OH}$ |
| R42 | $2\text{H}_2\text{O}_2 \rightarrow \text{H}_3\text{O}_2 + \text{HO}_2$ |
| R43 | $\text{H}_3\text{O}_2 \rightarrow \text{H}_2\text{O} + \text{OH}$ |
| R44 | $\text{O}_3 \rightarrow \text{O}_2 + \text{O}$ |
| R45 | $\text{H}_2\text{O} + \text{O} \rightarrow (\text{OH})_2$ |
| R46 | $(\text{OH})_2 + \text{O}_2 \rightarrow \text{O}_3 + \text{H}_2\text{O}$ |
| R47 | $\text{O} + \text{H}_2\text{O}_2 \rightarrow \text{O}_2 + \text{H}_2\text{O}$ |

BIBLIOGRAPHY

- [1] J. H. Merkin, D. J. Needham, and S. K. Scott, Oscillatory Chemical Reactions in Closed Vessels, *Proc. R. Soc. A* **406**, 299 (1986).
- [2] P. Gray and S. K. Scott, A New Model for Oscillatory Behavior in Closed Systems: The Autocatalator, *Ber. Bunsenges. Phys. Chem.* **90**, 985 (1986).
- [3] S. K. Scott, *Chemical Chaos*, Oxford University Press: Oxford, 1993.
- [4] M. Bodenstein, Eine Theorie der photochemischen Reaktionsgeschwindigkeiten, *Zeit. physik. Chemie.* **85**, 329 (1913).
- [5] S. Vajda, P. Valko, and T. Turanyi, Principal Kinetic Analysis of Kinetic Models, *Int. J. Chem. Kinet.* **17**, 55 (1985).
- [6] G. Esposito and H. K. Chelliah, Skeletal Reaction Models Based on Principal Component Analysis, *Combustion and Flame* **158**, 477 (2011).
- [7] I. G. Zsely, T. Turanyi, The Influence of Thermal Coupling and Diffusion on the Importance of Reactions: The Case Study of Hydrogen-Air Combustion. *Phys. Chem. Chem. Phys.* **5**, 3622 (2003).
- [8] N.J. Brown, G. Li, and M.L. Koszykowski, Mechanism reduction via principal component analysis, *Int. J. Chem. Kinet.* **29**, 393 (1997).
- [9] A. E. Lutz, R. J. Kee, and J. A. Miller, SENKIN: A Fortran Program for Predicting Homogenous Gas Phase Chemical Kinetics with Sensitivity Analysis, SAND87-8248; Sandia National Laboratories: Albuquerque, NM, 1988.
- [10] V. Szalay, Iterative and Direct Methods Employing Distributed Approximating Functionals for the Reconstruction of a Potential Energy Surface from Its Sampled Values, *J. Chem. Phys.* **111**, 8804 (1999).

- [11] T. Hollebeek, T.-S. Ho, and H. Rabitz, Efficient Potential Energy Surfaces from Partially Filled Ab Initio Data over Arbitrarily Shaped Regions, *J. Chem. Phys.* **114**, 3940 (2001).
- [12] L. Verlet, Computer “Experiments” on Classical Fluids. I. Thermodynamical Properties of Lennard-Jones Molecules, *Phys. Rev.* **159**, 98 (1967).
- [13] W. C. Swope, H. C. Andersen, P. H. Berens, and K. R. Wilson, A Computer Simulation Method for the Calculation of Equilibrium Constants for the Formation of Physical Clusters of Molecules: Application to Small Water Clusters, *J. Chem. Phys.* **76**, 637 (1982).
- [14] Y. Guo, T. D. Sewell, and D. L. Thompson, Analysis of the Zero-Point Energy Problem in Classical Trajectories, *J. Chem. Phys.* **104**, 576 (1996).
- [15] L. M. Raff and D. L. Thompson, The Classical Trajectory Approach to Reactive Scattering, *Theory of Chemical Reaction Dynamics*, Vol. III, Ed. M. Baer (CRC Press, Boca Raton, Fl).
- [16] R. N. Porter, Classical Trajectory Methods in Molecular Collisions, *Ann. Rev. Phys. Chem.* **25**, 317 (1974).
- [17] D. L. Bunker, Classical Trajectory Methods, *Method. Comput. Phys.* **10**, 287 (1971).
- [18] N. N. Semenov, *Some Problems in Chemical Kinetics and Reactivity*, Vols. I and II (translation), Princeton University Press, Princeton, NJ, 1959.
- [19] G. Dixon-Lewis and D. J. Williams, The Oxidation of Hydrogen and Carbon Monoxide, *Comprehensive Chemical Kinetics*, Vol. 17, Elsevier, Amsterdam, 1977.
- [20] B. Lewis and G. von Elbe, *Combustion, Flames and Explosions of Gases*, 3rd Ed., Academic, New York, 1987.

- [21] I. Glassman and R. A. Yetter, *Combustion*, 4th Ed., Elsevier, New York, 2008.
- [22] C. N. Hinshelwood and E. A. Moelwyn-Hughes, The Lower Pressure Limit in the Chain Reaction between Hydrogen and Oxygen, *Proc. R. Soc. Lond. Ser. A* **138**, 311 (1932)
- [23] A. A. Frost and N. H. Alyea, Kinetics of the Hydrogen—Oxygen Low Pressure Explosion, *J. Am. Chem. Soc.* **55**, 3227 (1933).
- [24] X. M. Wang and C. K. Law, An analysis of the explosion limits of hydrogen-oxygen mixtures, *J. Chem. Phys.* **138**, 134305 (2013).
- [25] R. R. Baldwin, M. E. Fuiler, J. S. Hillman, D. Jackson, and R. W. Walker, Second limit of hydrogen + oxygen mixtures: the reaction $H + HO_2$, *J. Chem. Soc. Faraday Trans. I* **70**, 635 (1974).
- [26] U. Mass and J. Warnatz, Ignition Processes in Hydrogen-Oxygen Mixtures, *Combust. Flame* **74**, 53, (1988).
- [27] D. L. Baulch, J. F. Griffiths, A. J. Pappin, and A. F. Sykes, Third-Body Interactions in the Oscillatory Oxidation of Hydrogen in a Well Stirred Flow Reactor, *J. Chem. Soc. Faraday Trans. I* **84**, 1575 (1988).
- [28] W. Kordylewski and S. K. Scott, The Influence of Self-Heating on the Second and Third Explosion Limits in the $O_2 + H_2$ Reaction, *Combust. Flame* **57**, 127 (1984).
- [29] E. P. Dougherty and H. Rabitz, Computational Kinetics and Sensitivity Analysis of Hydrogen-Oxygen Combustion, *J. Chem. Phys.* **72**, 6571 (1980).
- [30] G. Dixon-Lewis, Computer Modeling of Combustion Reactions in Flowing Systems with Transport, *Combustion Chemistry*, Springer, New York, 1984.

- [31] K. K. Foo and C. H. Yang, On the Surface and Thermal Effects of Hydrogen Oxidation, *Combust. Flame* **17**, 223 (1971).
- [32] N. M. Marinov, C. K. Westbrook, and W. J. Pitz in Transport Phenomena in Combustion, vol. 1, Taylor and Francis, Washington DC, 1996.
- [33] M.A. Mueller, T.J. Kim, R.A. Yetter, and F.L. Dryer, Flow Reactor Studies and Kinetic Modeling of the H₂/O₂ Reaction, *Int. J. Chem. Kinet.* **31**, 113 (1999).
- [34] J. Li, Z. Zhao, A. Kazakov, and F.L. Dryer, An Updated Comprehensive Kinetic Model of Hydrogen Combustion, *Int. J. Chem. Kinet.* **36**, 566 (2004).
- [35] M. O'Conaire, H. J. Curran, J. M. Simmie, W. J. Pitz, and C. K. Westbrook, A Comprehensive Modeling Study of Hydrogen Oxidation, *Int. J. Chem. Kinet.* **36**, 603 (2004).
- [36] O. P. Shatalov, L. B. Ibraguimova, V. A. Pavlov, G. D. Smekhov, and Y. V. Tunik, Presented in part at Proceedings of the European Combustion Meeting, Analysis of the Kinetic Data Described Oxygen-Hydrogen Mixtures Combustion, Moscow, Russia, 2009.
- [37] M. P. Burke, M. Chaos, Y. Ju, F. L. Dryer, and S. J. Klippenstein, Comprehensive H₂/O₂ Kinetic Model for High-Pressure Combustion, *Int. J. Chem. Kinet.* **44**, 444 (2011).
- [38] D. L. Baulch, C. J. Cobos, R. A. Cox, C. Esser, P. Frank, Th. Just, J. A. Kerr, M. J. Pilling, J. Troe, R. W. Walker, and J. Warnatz, Evaluated Kinetic Data for Combustion Modelling, *J. Phys. Chem. Ref. Data* **21**, 411 (1992).
- [39] D. L. Baulch, C. J. Cobos, R. A. Cox, P. Frank, G. Hayman, Th. Just, J. A. Kerr, T. Murrells, M. J. Pilling, J. Troe, R. W. Walker, and J. Warnatz, Evaluated Kinetic Data for Combustion Modelling: Supplement I, *J. Phys. Chem. Ref. Data* **23**, 847 (1994).

- [40] D. L. Baulch, C. T. Bowman, C. J. Cobos, R. A. Cox, Th. Just, J. A. Kerr, M. J. Pilling, D. Stocker, J. Troe, W. Tsang, R. W. Walker, and J. Warnatz, Evaluated Kinetic Data for Combustion Modeling: Supplement II, *J. Phys. Chem. Ref. Data* **34**, 757 (2005).
- [41] Z. Hong, D. F. Davidson, and R. K. Hanson, An Improved H₂/O₂ Mechanism Based on Recent Shock Tube/Laser Absorption Measurements, *Combust. Flame* **158**, 633 (2011).
- [42] A. H. Willbourn and C. N. Hinshelwood, The Mechanism of the Hydrogen-Oxygen Reaction. III. The Influence of Salts, *Proc. R. Soc. Lond. Ser. A* **185**, 376 (1946).
- [43] F. E. Belles, Detonability and Chemical Kinetics: Predictions of Limits of Detonability of Hydrogen. In *Seventh Symposium (International) on Combustion*, 745 (1959).
- [44] J. E. Dove and T. D. Tribbeck, Computational Study of the Kinetics of the Hydrogen-Oxygen Reaction behind Steady State Shock Waves. Application to the Composition Limits and Transverse Stability of Gaseous Detonations. *Astronautica Acta* **15**, 387 (1970).
- [45] R. A. Yetter, F. L. Dryer, and D. M. Golden, in *Major Topics in Combustion*, Springer-Verlag, New York, 1992.
- [46] J. W. Dold and A. K. Kapila, Comparison between Shock Initiations of Detonation Using Thermally Sensitive and Chain-Branching Chemical Models, *Combustion and Flame* **85**, 185 (1991).
- [47] M. Short and J. J. Quirk, On the Nonlinear Stability and Detonability Limit of a Detonation Wave for a Model Three-Step Chain Branching Reaction. *J. of Fluid Mech.* **339**, 89 (1997).

- [48] T. Varga, T. Nagy, C. Olm, I. Gy. Zse'ly, R. Pa'lvlygi, E'. Valko', G. Vincze, M. Cserha'ti, H. J. Curran, and T. Tura'nyi, Optimization of a Hydrogen Combustion Mechanism Using both Direct and Indirect Measurements, *Proc. Combust. Inst.* **35**, 589 (2015).
- [49] A. Kéromnès, W. K. Metcalfe, K. A. Heufer, N. Donohoe, A. K. Das, C. J. Sung, J. Herzler, C. Naumann, P. Griebel, O. Mathieu, M. C. Krejci, E. L. Petersen, W. J. Pitz, and H. J. Curran, An Experimental and Detailed Chemical Kinetic Modelling Study of Hydrogen and Syngas Mixtures at Elevated Pressures, *Combust. Flame* **160**, 995 (2013).
- [50] J. Strohle and T. Myhrvold, An Evaluation of Detailed Reaction Mechanisms for Hydrogen Combustion under Gas Turbine conditions, *International Journal of Hydrogen Energy* **32**, 125 (2007).
- [51] N. Popov, The Effect of Nonequilibrium Excitation on the Ignition of Hydrogen-Oxygen Mixtures, *High Temp.* **45**, 261 (2007).
- [52] J. V. Michael, J. W. Sutherland, L. B. Harding, and A. F. Wagner, Initiation in H₂/O₂: Rate Constants for H₂ + O₂ → H + HO₂ at High Temperature, *Proc. Combust. Inst.* **28**, 1471 (2000).
- [53] A.A. Konnov, On the Role of Excited Species in Hydrogen Combustion, *Combust. Flame* **162**, 3753 (2015).
- [54] V. E. Kozlov, A. M. Starik, and N. S. Titova, Enhancement of Combustion of a HydrogenAir Mixture by Excitation of O₂ Molecules to the O₂(a¹Δ_g) State, *Combustion, Explosion, and Shock Waves* **44**, 371 (2008).

- [55] V. V. Smirnov, O. M. Stelmakh, V. I. Fabelinsky, D. N. Kozlov, A. N. Starik, and N. S. Titova, On the Influence of Electronically Excited Oxygen Molecules on Combustion of Hydrogen-Oxygen Mixture, *J. Phys. D: Appl. Phys.* **41**, 192001 (2008).
- [56] A. M. Starik, V. E. Kozlov, and N. S. Titova, On Mechanisms of a Flame Velocity Increase upon Activation of O₂ Molecules in Electrical Discharge, *J. Phys. D: Appl. Phys.* **41**, 125206 (2008).
- [57] T. Ombrello, S.H. Won, Y. Ju, and S. Williams, Flame Propagation Enhancement by Plasma Excitation of Oxygen. Part II: Effects of O₂(a¹Δ_g), *Combust. Flame* **157**, 1916 (2010)
- [58] K. Chenoweth, A. C. T. van Duin and W. A. Goddard, ReaxFF Reactive Force Field for Molecular Dynamics Simulations of Hydrocarbon Oxidation, *J. Phys. Chem. A* **112**, 1040 (2008).
- [59] K. Chenoweth, A. C. T. van Duin, S. Dasgupta and W. A. Goddard, Initiation Mechanisms and Kinetics of Pyrolysis and Combustion of JP-10 Hydrocarbon Jet Fuel, *J. Phys. Chem. A* **113**, 1740 (2009).
- [60] J. E. Mueller, A. C. T. van Duin, and W. A. Goddard, Development and Validation of ReaxFF Reactive Force for Hydrocarbon Chemistry Catalyzed by Nickel, *J. Phys. Chem. C* **114**, 4939 (2010).
- [61] J. E. Mueller, A. C. T. van Duin, and W. A. Goddard, Application of the ReaxFF Reactive Force Field to Reactive Dynamics of Hydrocarbon Chemisorption and Decomposition, *J. Phys. Chem. C* **114**, 5675 (2010).

- [62] M. F. Jr. Russo and A. C. T. van Duin, Atomistic-scale simulations of chemical reactions: Bridging from quantum chemistry to engineering. *Nucl. Instrum. Methods Phys. Res. B* **269**, 1549 (2011).
- [63] T. P. Senftle, S. Hong, M. M. Islam, S. B. Kylasa, Y. Zheng, Y. K. Shin, C. Junkermeier, R. Engel-Herbert, M. J. Janik, H. M. Aktulga, T. Versraelen, A. Grama, and A. C. T. van Duin, The ReaxFF Reactive Force-Field: Development, Applications and Future Directions. *Npj Comput. Mater.* **2**, 15011 (2016).
- [64] S. Agrawalla and A. C. T. van Duin, Development and Application of a ReaxFF Reactive Force Field for Hydrogen Combustion, *J. Phys. Chem. A* **115**, 960 (2011).
- [65] A. D. Becke, Density functional thermochemistry. III. The role of exact exchange, *J. Chem. Phys.* **98**, 5648 (1993).
- [66] C. T. Lee, W. T. Yang, and R. G. Parr, Development of the Colle-Salvetti correlation-energy formula into a functional of the electron density, *Phys. Rev. B* **37**, 785 (1988).
- [67] R. Krishnan, J. S. Binkley, R. Seeger, and J. A. Pople, Self-consistent molecular orbital methods. XX. A basis set for correlated wave functions, *J. Chem. Phys.* **72**, 650 (1980).
- [68] R. B. Woodward and R. Hoffman, *The Conservation of Orbital Symmetry*, Verlag Chemie, Weinheim and Academic Press, New York, 1970.
- [69] J. Michl, Physical basis of qualitative MO arguments in organic photochemistry, *Topics Curr. Chem.* **46**, 1 (1974).
- [70] R. G. Pearson, *Symmetry rules for chemical reactions*, Wiley, New York, 1976.

- [71] C. K. Westbrook, Hydrogen Oxidation Kinetics in Gaseous Detonations, *Combust. Sci. Technol.* **29**, 67 (1982).
- [72] S. P. Karkach and V. I. Osherov, *Ab Initio* Analysis of the Transition States on the Lowest Triplet H₂O₂ Potential Surface, *J. Chem. Phys.* **110**, 11918 (1999).
- [73] W. G. Mallard, F. Westley, J. T. Herron and R. F. Hampson, *NIST Chemical Kinetics Database Ver. 6.0*, NIST Standard Reference Data, Gaithersburg, MD, 1994.
- [74] M. Bartolomei, M. I. Hernández, J. Campos-Martinez, E. Carmona-Novillo and R. Hernández-Lamoneda. The Intermolecular Potentials of the O₂-O₂ Dimer: a Detailed *Ab Initio* Study of the Energy Splittings for the Three Lowest Multiplet States, *Phys. Chem. Chem. Phys.* **10**, 5374 (2008).
- [75] P. E. S. Wormer and A. van der Avoird, (Heisenberg) Exchange and Electrostatic Interactions between O₂ molecules: an *Ab Initio* Study, *J. Chem. Phys.*, **81**, 1929 (1984).
- [76] R. Hernández-Lamoneda, M. Bartolomei, M. I. Hernández, J. Campos-Martinez, and F. Dayou, Intermolecular Potential of the O₂-O₂ Dimer. An *Ab Initio* Study and Comparison with Experiment, *J. Phys. Chem. A* **109**, 11587 (2005).
- [77] M. Bartolomei, E. Carmona-Novillo, M. I. Hernández, J. Campos-Martinez, and R. Hernández-Lamoneda, Global *Ab Initio* Potential Energy Surface for the O₂($3\Sigma_g^-$) + O₂($3\Sigma_g^-$) Interaction, *J. Chem. Phys.* **133**, 124311 (2010).
- [78] M. C. van Hemert, P. E. S. Wormer, A. van der Avoird, *Ab Initio* Calculation of the Heisenberg Exchange Interaction between O₂ Molecules, *Phys. Rev. Lett.* **51**, 1167 (1983).
- [79] B. Bussery, P. E. S. Wormer, A van der Waals intermolecular potential for (O₂)₂, *J. Chem. Phys.* **99**, 1230 (1993).

- [80] H. M. Aktulga, J. C. Fogarty, S. A. Pandit and A. Y. Grama, Parallel Reactive Molecular Dynamics: Numerical Methods and Algorithmic Techniques, *Parallel Computing* **38**, 245 (2012).
- [81] S. Plimpton, Fast Parallel Algorithms for Short-Range Molecular Dynamics, *J. Comp. Phys.* **117**, 1 (1995).
- [82] W. R. Hoover, Canonical Dynamics: Equilibrium Phase-Space Distributions, *Phys. Rev. A* **31**, 1695 (1985).
- [83] S. Nosé, Unified Formulation of the Constant Temperature Molecular Dynamics Methods, *J. Chem. Phys.* **81**, 511 (1984).
- [84] A. P. Thompson, S. J. Plimpton, and W. Mattson, General formulation of pressure and stress tensor for arbitrary many-body interaction potentials under periodic boundary conditions, *J. Chem. Phys.* **131**, 154107 (2009).
- [85] E. W. Lemmon, M. L. Huber, J. W. Leachman, Revised Standardized Equation for Hydrogen Gas Densities for Fuel Consumption Applications. *J. Res. Nat. Inst. Stand. Technol.* **113**, 341 (2008).
- [86] E. W. Lemmon, M. L. Huber, M. O. McLinden, NIST Standard Reference Database 23: Reference Fluid Thermodynamic and Transport Properties-REFPROP, Version 8.0, National Institute of Standards and Technology, Standard Reference Data Program, Gaithersburg, 2007.
- [87] N. M. Kuznetsov, A. V. Dubrovsky, S. M. Frolov, Analytical Approximation of the Thermal and Caloric Equations of State for Real Gases over a Wide Density and Temperature Range. *Russian J. Phys. Chem. B* **5**, 1084 (2011).

- [88] V. V. Sychev, A. A. Vasserman, A. D. Kozlov, G. A. Spiridonov, and V. A. Tsymarnyi, Thermodynamic Properties of Oxygen. *Nat. Stand. Ref. Data Service of the USSR*, **5**, 1987.
- [89] L. Martinez, R. Andrade, E. G. Birgin, and J. M. Martinez, PACKMOL: A Package for Building Initial Configurations for Molecular Dynamics Simulations, *J. Comp. Chem.* **30**, 2157 (2009).
- [90] E. Polak and G. Ribiere, *Rev. Fran. Informat. Rech. Oper.* **3**, 35 (1969).
- [91] H. C. Andersen, Cluster Methods in Equilibrium Statistical Mechanics of Fluids. In *Statistical Mechanics, Part A: Equilibrium Techniques*; Berne, B. J., Ed.; Plenum: New York, 1977.
- [92] T. L. Hill, *An Introduction to Statistical Thermodynamics*, Dover Publications, Inc., New York, 1986.
- [93] T. Cheng, A. Jaramillo-Botero, W. A. Goddard, and H. Sun, Adaptive Accelerated ReaxFF Reactive Dynamics with Validation from Simulating Hydrogen Combustion, *J. Am. Chem. Soc.* **136**, 9434 (2014).
- [94] W. R. Stockwell, On the HO₂ + HO₂ Reaction: Its Misapplication in Atmospheric Chemistry Models, *J. Geophys. Res.* **100**, 11695 (1995).
- [95] D. D. Y. Zhou, K. Han, P. Zhang, L. B. Harding, M. J. Davis, and R. T. Skodje, Theoretical Determination of the Rate Coefficient for the HO₂ + HO₂ → H₂O₂ + O₂ Reaction. Adiabatic Treatment of Anharmonic Torsional Effects, *J. Phys. Chem. A* **116**, 2089 (2012).
- [96] C. C. Kircher and S. P. Sander, Kinetics and Mechanism of HO₂ and DO₂ Disproportionations, *J. Phys. Chem.* **88**, 2082 (1984).

- [97] Bodenstein, M., *Z. Physik. Chem. (Leipzig)* **100**, 68 (1922).
- [98] R. C. Tolman, *Statistical mechanics with applications to physics and chemistry*, Chem. Cat. Co., New York, 1927.
- [99] L. S. Kassel, *The kinetics of homogeneous gas reactions*, Chem. Cat. Co., New York, 1932.
- [100] F. T. Smith, Triple Collisions and Termolecular Reaction Rates, *Kinetic processes in gases and plasmas*, Academic Press, New York and London, 1969.
- [101] H. Jónsson, G. Mills, and K. W. Jacobsen, *Classical and Quantum Dynamics in Condensed Phase Simulations*, edited by B. J. Berne, G. Ciccoti, and D. F. Coker, World Scientific, Singapore (1998).
- [102] G. Henkelman, B. P. Uberuaga and H. Jónsson, A Climbing Image Nudged Elastic Band Method for Finding Saddle Points and Minimum Energy Paths, *J. Chem. Phys.* **113**, 9901 (2000).
- [103] G. Henkelman and H. Jónsson, Improved Tangent Estimate in the Nudged Elastic Band Method for Finding Minimum Energy Paths and Saddle Points, *J. Chem. Phys.* **113**, 9978 (2000).
- [104] L. R. Pratt, A statistical method for identifying transition states in high dimensional problems *J. Chem. Phys.* **85**, 5045 (1986).
- [105] R. Elber and M. Karplus, A method for determining reaction paths in large molecules: Application to myoglobin, *Chem. Phys. Lett.* **139**, 375 (1987).
- [106] E. M. Sevick, A. T. Bell, and D. N. Theodorou, A chain of states method for investigating infrequent event processes occurring in multistate, multidimensional systems, *J. Chem. Phys.* **98**, 3196 (1993).

- [107] R. E. Gillilan and K. R. Wilson, Shadowing, rare events, and rubber bands. A variational Verlet algorithm for molecular dynamics, *J. Chem. Phys.* **97**, 1757 (1992).
- [108] A. Nakano, A Space–Time-Ensemble Parallel Nudged Elastic Band Algorithm for Molecular Kinetics Simulation, *Comp. Phys. Comm.* **178**, 280 (2008).
- [109] M. J. Frisch, G. W. Trucks, H. B. Schlegel, G. E. Scuseria, M. A. Robb, J. R. Cheeseman, G. Scalmani, V. Barone, B. Mennucci, G. A. Petersson, H. Nakatsuji, M. Caricato, X. Li, H. P. Hratchian, A. F. Izmaylov, J. Bloino, G. Zheng, J. L. Sonnenberg, M. Hada, M. Ehara, K. Toyota, R. Fukuda, J. Hasegawa, M. Ishida, T. Nakajima, Y. Honda, O. Kitao, H. Nakai, T. Vreven, J. A. Jr. Montgomery, J. E. Peralta, F. Ogliaro, M. Bearpark, J. J. Heyd, E. Brothers, K. N. Kudin, V. N. Staroverov, R. Kobayashi, J. Normand, K. Raghavachari, A. Rendell, J. C. Burant, S. S. Iyengar, J. Tomasi, M. Cossi, N. Rega, J. M. Millam, M. Klene, J. E. Knox, J. B. Cross, V. Bakken, C. Adamo, J. Jaramillo, R. Gomperts, R. E. Stratmann, O. Yazyev, A. J. Austin, R. Cammi, C. Pomelli, J. W. Ochterski, R. L. Martin, K. Morokuma, V. G. Zakrzewski, G. A. Voth, P. Salvador, J. J. Dannenberg, S. Dapprich, A. D. Daniels, Ö. Farkas, J. B. Foresman, J. V. Ortiz, J. Cioslowski, and D. J. Fox, GAUSSIAN 09 (Revision D.01), Gaussian Inc., Wallingford, CT, 2009.
- [110] J. Čížek, *Advances in Chemical Physics*, Wiley Interscience, New York (1969).
- [111] R. J. Bartlett, Coupled-Cluster Approach to Molecular Structure and Spectra: a Step Toward Predictive Quantum Chemistry, *J. Phys. Chem.* **93**, 1697 (1989).
- [112] T. H. Jr. Dunning, Gaussian Basis Sets for Use in Correlated Molecular Calculations. I. The Atoms Boron through Neon and Hydrogen, *J. Chem. Phys.* **90**, 1007 (1989).

- [113] R. A. Kendall, T. H. Jr. Dunning, and R. J. Harrison, Electron Affinities of the First-Row Atoms Revisited. Systematic Basis Sets and Wave, *J. Chem. Phys.* **96**, 6796 (1992).
- [114] C. Moller and M. S. Plesset, Note on an Approximation Treatment for Many-Electron Systems, *Phys. Rev.* **46**, 618 (1934).
- [115] W. J. Hehre, R. Ditchfield, and J. A. Pople, Self-Consistent Molecular Orbital Methods. XII. Further Extensions of Gaussian-Type Basis Sets for Use in Molecular Orbital Studies of Organic Molecules, *J. Chem. Phys.* **56**, 2257 (1972).
- [116] S. F. Boys and F. Bernardi, Calculation of Small Molecular Interactions by Differences of Separate Total Energies – Some Procedures with Reduced Errors, *Mol. Phys.* **19**, 553 (1970).
- [117] T. J. Lee and P. R. Taylor, A Diagnostic for Determining the Quality of Single-Reference Electron Correlation Methods, *Int. J. Quantum Chem., Quantum Chem. Symp.* **S23**, 1999 (1989).
- [118] S. Wilson, P. J. Grout, J. Maruani, G. Delgado-Barrio and P. Piecuch, *Frontiers in Quantum Systems in Chemistry and Physics*, Springer, 2008, pp. 397-401.
- [119] I. W. Bulik, T. M. Henderson, and G. E. Scuseria, Can Single-Reference Coupled Cluster Theory Describe Static Correlation?, *J. Chem. Theory Comput.* **11**, 3171 (2015).
- [120] O. B. Gadzhiev, S. K. Ignatov, M. Y. Kulikov, A. M. Feigin, A. G. Razuvaev, P. G. Sennikov and O. Schrems, Structure, Energy, and Vibrational Frequencies of Oxygen Allotropes On ($n \leq 6$) in the Covalently Bound and van der Waals Forms: Ab Initio Study at the CCSD(T) Level, *J. Chem. Theory Comput.* **9**, 247 (2012).

- [121] M. Litorja, and B. A. Ruscic, Photoionization Study of Hydroperoxyl Radical, HO₂, and Hydrogen Peroxide, H₂O₂, *J. Electron Spectrosc.*, **97**, 131 (1998).
- [122] D. Jayatilaka, and T. J. Lee, Open-shell Coupled-cluster Theory, *J. Chem. Phys.* **98**, 9734 (1993).
- [123] J. C. Rienstra-Kiracofe, W. D. Alleu, and H. F. Schaefer III, The C₂H₅ + O₂ Reaction Mechanism: High-Level *Ab Initio* Characterizations, *J. Phys. Chem. A* **104**, 9823 (2000).
- [124] M. Akbar-Ali, J. A. Sonk, and J. R. Barker, Predicted Chemical Activation Rate Constants for HO₂ + CH₂NH: The Dominant Role of a Hydrogen-Bonded Pre-reactive Complex, *J. Phys. Chem. A* **120**, 7060 (2016).
- [125] J. D. Watts, J. Gauss, and R. J. Bartlett, Open-Shell Analytical Energy Gradients for Triple Excitation Many-Body, Coupled-Cluster Methods: MBPT(4), CCSD+T(CCSD), CCSD(T) and QCISD(T), *Chem. Phys. Lett.* **200**, 1 (1992).
- [126] W. J. Lauderdale, V. G. Cheng, and S. G. Wierschke, Calculated Infrared Frequencies and Intensities of the HO₂ Radicals, *J. Phys. Chem. A* **98**, 4502 (1994).
- [127] W. J. Lauderdale, J. F. Stanton, J. Gauss, J. D. Watts, and R. J. Bartlett, Many-Body Perturbation Theory with a Restricted Open-Shell Hartree-Fock Reference, *Chem. Phys. Lett.* **187**, 21 (1991).
- [128] W. J. Lauderdale, J. F. Stanton, J. Gauss, J. D. Watts, and R. J. Bartlett, Restricted Open-Shell Hartree-Fock-Based Many-Body Perturbation Theory: Theory and Applications of Energy Gradient Calculations, *J. Chem. Phys.* **97**, 6606 (1992).

- [129] M. Urban, J. D. Watts, and R. J. Bartlett, On the Accuracy of Molecular Properties by Coupled-Cluster Methods for Some Difficult Examples: Oxygen Atom, Iron Atom, and Cyano Radical, *Int. J. Quantum Chem.* **52**, 211 (1994).
- [130] R. C. Tolman, Statistical Mechanics Applied to Chemical Kinetics, *J. Amer. Chem. Soc.* **42**, 2506 (1920).
- [131] R. H. Fowler, and E. A. Guggenheim, *Statistical Thermodynamics: A Version of Statistical Mechanics for Students of Physics and Chemistry*. (The Syndics of The Cambridge University Press, 1956).
- [132] D. G. Truhlar, Interpretation of the Activation Energy, *J. Chem. Educ.* **55**, 309 (1978).
- [133] R. K. Boyd, Macroscopic and Microscopic Restrictions on Chemical Kinetics, *Chem. Rev.* **77**, 93 (1977).
- [134] T. Inagaki, and T. Yamamoto, Critical Role of Deep Hydrogen Tunneling to Accelerate the Antioxidant Reaction of Ubiquinol and Vitamin E, *J. Phys. Chem. B* **118**, 937 (2014).
- [135] T. C. Allison, G. C. Lynch, M. S. Gordon, and D. G. Truhlar, An Improved Potential Energy Surface for the H₂Cl System and Its Use for Calculations of Rate Coefficients and Kinetic Isotope Effects, *J. Phys. Chem.* **100**, 13575 (1996).
- [136] H. Haddadi, N. Alizadeh, M. Shamsipur, and Z. Asfari, Dynamic NMR Study of the Kinetics of Complexation of Tl⁺ Ion with Calix[4]crown-6, *J. Phys. Chem. A* **114**, 7462 (2010).
- [137] S. S. Kumaran, K. P. Lim, and J. V. Michael, Thermal rate constants for the Cl+H₂ and Cl+D₂ reactions between 296 and 3,000 K, *J. Chem. Phys.* **101**, 9487 (1994).

- [138] J. H. Lee, J. V. Michael, W. A. Payne, L. J. Stief, and D. A. Whytock, Absolute Rate of the Reaction of Cl(2P) with Molecular Hydrogen from 200–500 K, *J. Chem. Soc. Faraday Trans. I* **73**, 1530 (1977).
- [139] J. C. Miller, and R. J. Gordon, Kinetics of the Cl–H₂ System. I. Detailed Balance in the Cl+H₂ Reaction, *J. Chem. Phys.* **75**, 5305 (1981).
- [140] A. A. Westenberg, and N. de Haas, Atom–Molecule Kinetics using ESR Detection. IV. Results for Cl + H₂ ⇌ HCl + H in Both Directions, *J. Chem. Phys.* **48**, 4405 (1968).
- [141] D. G. Truhlar, and A. Kohen, Convex Arrhenius Plots and Their Interpretation , *Proc. Natl. Acad. Sci. U S A.* **98** (3), 848 (2001).
- [142] R. G. Gilbert, and I. G. Ross, Concept of Activation Energy in Unimolecular Reactions, *J. Chem. Phys.* **57**, 2299 (1972).
- [143] A. Wrba, A. Schweiger, V. Schultes, R. Jaenicke, and P. Zavodszky, Extremely Thermostable D-glyceraldehyde-3-phosphate Dehydrogenase from the Eubacterium *Thermotoga Maritima*, *Biochemistry* **29**, 7584 (1990).
- [144] S. Lakatos, G. Halasz, and P. Zavodszky, Conformational Stability of Lactate Dehydrogenase from *Bacillus Thermus-aquaticus* [proceedings], *Biochem. Soc. Trans.* **6**, 1195 (1978).
- [145] A. Kohen, R. Cannio, S. Bartolucci, and J. P. Klinman, Enzyme Dynamics and Hydrogen Tunnelling in a Thermophilic Alcohol Dehydrogenase, *Nature (London)* **399**, 496 (1999).
- [146] F. T. Smith, Generalized Angular Momentum in Many-Body Collisions, *Phys. Rev.* **120**, 1058 (1960).

- [147] F. T. Smith, Scattering Matrix and Chemical Reaction Rates, *J. Chem. Phys.* **36**, 248 (1962).
- [148] R. C. Dunbar, Kinetics of Low-intensity Infrared Laser Photodissociation. The Thermal Model and Application of the Tolman Theorem, *J. Chem. Phys.* **95**, 2537 (1991).
- [149] C. Zener, Non-Adiabatic Crossing of Energy Levels, *Proc. R. Soc. London A* **137**, 696 (1932).
- [150] L. D. Landau, On the theory of transfer of energy at collisions II, *Phys. Z.* **2**, 46 (1932).
- [151] D. Borgis and J. T. Hynes, Curve crossing formulation for proton transfer reactions in solution, *J. Phys. Chem.* **100**, 1118 (1996).
- [152] Voter, A. F. Introduction to the Kinetic Monte Carlo Method. In *Radiation Effects in Solids*; Sickafus, K. E., Kotomin, E. A., Eds.; Springer. NATO Publishing Unit: Dordrecht, The Netherlands, 2005.
- [153] B. Ginovska, D. M. Camaioni, and M. Dupuis, Reaction pathways and excited states in $\text{H}_2\text{O}_2 + \text{OH} \rightarrow \text{HO}_2 + \text{H}_2\text{O}$: A new ab initio investigation, *J. Chem. Phys.* **127**, 84309 (2007)
- [154] C. Gonzalez, J. Theisen, L. Zhu, H. B. Schlegel, and W. L. Hase, Kinetics of the Reaction between OH and HO₂ on the Singlet Potential Energy Surface, *J. Phys. Chem.* **95**, 6784 (1991).
- [155] C. Gonzalez, J. Theisen, H. B. Schlegel, and W. L. Hase, Kinetics of the Reaction between OH and HO₂ on the Triplet Potential Energy Surface, *J. Phys. Chem.* **96**, 1767 (1992).

[156] M. J. Uline, D. W. Siderius, and D. S. Corti, On the generalized equipartition theorem in molecular dynamics ensembles and the microcanonical thermodynamics of small systems, *J. Chem. Phys.* **128**, 124301 (2008).

VITA

Homayoon Rafatijo was born in Tehran, Iran on April 16, 1990. He got his diploma in math and physics from National Organization for Development of Exceptional Talents (NODET) in 2008. Soon after he finished the high school, Homayoon got admitted to Sharif University of Technology known as the most competitive university of Iran to study Aerospace Engineering. In 2011, Homayoon started theoretical physical chemistry as a minor subject to pursue his main interest to understand the fundamental nature of chemical and physical processes. In 2013, Homayoon received his degree from Sharif University of Technology and immediately got admitted to the chemistry program at University of Missouri-Columbia to study for the doctoral degree under supervision of Professor Donald L. Thompson.